
Doctoral Dissertations

Student Theses and Dissertations

Fall 2012

Compressive sensing for 3D microwave imaging systems

Hamed Kajbaf

Follow this and additional works at: https://scholarsmine.mst.edu/doctoral_dissertations



Part of the [Electrical and Computer Engineering Commons](#)

Department: **Electrical and Computer Engineering**

Recommended Citation

Kajbaf, Hamed, "Compressive sensing for 3D microwave imaging systems" (2012). *Doctoral Dissertations*. 2145.

https://scholarsmine.mst.edu/doctoral_dissertations/2145

This thesis is brought to you by Scholars' Mine, a service of the Missouri S&T Library and Learning Resources. This work is protected by U. S. Copyright Law. Unauthorized use including reproduction for redistribution requires the permission of the copyright holder. For more information, please contact scholarsmine@mst.edu.

COMPRESSIVE SENSING FOR 3D MICROWAVE IMAGING SYSTEMS

by

HAMED KAJBAF

A DISSERTATION

Presented to the Faculty of the Graduate School of the

MISSOURI UNIVERSITY OF SCIENCE AND TECHNOLOGY

in Partial Fulfillment of the Requirements for the Degree

DOCTOR OF PHILOSOPHY

in

ELECTRICAL ENGINEERING

2012

Approved by:

Dr. Yahong Rosa Zheng, Advisor

Dr. Reza Zoughi

Dr. Randy H. Moss

Dr. David J. Pommerenke

Dr. Von L. Richards

PUBLICATION DISSERTATION OPTION

This dissertation consists of the following five papers, formatted in the style used by the Missouri University of Science and Technology, listed as follows:

Paper 1, H. Kajbaf, Y.R. Zheng, and R. Zoughi, “Improving efficiency of microwave imaging systems using compressive sensing technology,” is accepted for publication in Materials Evaluation, 2012.

Paper 2, H. Kajbaf, J.T. Case, Z. Yang, and Y.R. Zheng, “Compressed sensing for SAR-Based wideband 3D microwave imaging system using nonuniform FFT,” has been submitted to IET Radar, Sonar, and Navigation, 2012.

Paper 3, H. Kajbaf and Y.R. Zheng, “Adaptive basis selection compressed sensing,” to be submitted to IEEE Trans. Instrum. Meas., 2012.

Paper 4, H. Kajbaf, J.T. Case, Y.R. Zheng, S. Kharkovsky, and R. Zoughi, “Quantitative and qualitative comparison of SAR images from incomplete measurements using compressed sensing and nonuniform FFT,” has been published in Proc. 2011 IEEE Radar Conf. (RADAR), Kansas City, MO, May 2011, pp. 592–596.

Paper 5, H. Kajbaf, J.T. Case, and Y.R. Zheng, “3D image reconstruction from sparse measurement of wideband millimeter wave SAR experiments,” has been published in Proc. of the 18th IEEE Int. Conf. on Image Process. (IEEE ICIP 2011), Brussels, Belgium, Sep. 2011, pp. 2701–2704.

ABSTRACT

Compressed sensing (CS) image reconstruction techniques are developed and experimentally implemented for wideband microwave synthetic aperture radar (SAR) imaging systems with applications to nondestructive testing and evaluation. These techniques significantly reduce the number of spatial measurement points and, consequently, the acquisition time by sampling at a level lower than the Nyquist-Shannon rate. Benefiting from a reduced number of samples, this work successfully implemented two scanning procedures: the nonuniform raster and the optimum path.

Three CS reconstruction approaches are also proposed for the wideband microwave SAR-based imaging systems. The first approach reconstructs a full-set of raw data from undersampled measurements via L1-norm optimization and consequently applies 3D forward SAR on the reconstructed raw data. The second proposed approach employs forward SAR and reverse SAR (R-SAR) transforms in each L1-norm optimization iteration reconstructing images directly. This dissertation proposes a simple, elegant truncation repair method to combat the truncation error which is a critical obstacle to the convergence of the CS iterative algorithm. The third proposed CS reconstruction algorithm is the adaptive basis selection (ABS) compressed sensing. Rather than a fixed sparsifying basis, the proposed ABS method adaptively selects the best basis from a set of bases in each iteration of the L1-norm optimization according to a proposed decision metric that is derived from the sparsity of the image and the coherence between the measurement and sparsifying matrices. The results of several experiments indicate that the proposed algorithms recover 2D and 3D SAR images with only 20% of the spatial points and reduce the acquisition time by up to 66% of that of conventional methods while maintaining or improving the quality of the SAR images.

ACKNOWLEDGMENT

First and foremost, I would like to thank my family for their endless love and support in my whole life. It would have been impossible for me to finish this work without their encouragement, understanding, reassurance, and kindness. I owe my loving thanks to my best friend, Farideh Fazayeli, for all the emotional support, camaraderie, enthusiasm, care, and help she provided to get me through difficult times.

I would like to express my sincere gratitude to both Dr. Yahong Rosa Zheng and Dr. Reza Zoughi for their continuous support of my PhD study and research. Their guidance, encouragement, and immense knowledge helped me throughout my research and writing of this dissertation. I also would like to thank the members of my PhD advisory committee, Dr. Randy H. Moss, Dr. David J. Pommerenke, and Dr. Von L. Richards, for their valuable advice and guidance during my study.

It is my pleasure to thank all of my friends in both the CRASP Research Group and the *amntl* of Missouri S&T for their company and assistance during my PhD years and all the colleagues at Missouri S&T for their assistance in my research work. My special thanks goes to Mr. Joseph T. Case, Mr. Mojtaba Fallahpour, Dr. Sergey Kharkovsky, Mr. Amirhossein Rafati, Dr. Mohammad T. Ghasr, and Mr. Zengli Yang for their valuable help during my research.

I would like to thank the American Society for Nondestructive Testing (ASNT), the Intelligent Systems Center (ISC), and University of Missouri Research Board for financially supporting this research.

TABLE OF CONTENTS

	Page
PUBLICATION DISSERTATION OPTION	iii
ABSTRACT	iv
ACKNOWLEDGMENT	v
LIST OF ILLUSTRATIONS	ix
LIST OF TABLES	xii
 SECTION	
1. INTRODUCTION	1
1.1. BACKGROUND.....	1
1.2. PROBLEM STATEMENT	4
1.3. SUMMARY OF CONTRIBUTIONS	7
 PAPER	
I. IMPROVING EFFICIENCY OF MICROWAVE WIDEBAND IMAGING USING COMPRESSED SENSING TECHNIQUES	10
ABSTRACT.....	10
1. INTRODUCTION	11
2. EXPERIMENTAL PROCEDURE	12
3. 2D AND 3D SAR IMAGING	14
4. COMPRESSED SENSING FOR SAR IMAGING	17
5. EXPERIMENTAL RESULTS AND DISCUSSIONS.....	20
5.1. 2D EXPERIMENTS	20
5.2. 3D EXPERIMENTS	21
5.3. FIGURES OF MERIT.....	21
5.4. CORROSION UNDER PAINT EXPERIMENT	28
6. CONCLUSION.....	30
7. ACKNOWLEDGMENT.....	30

II. COMPRESSED SENSING FOR SAR-BASED WIDEBAND 3D MICROWAVE IMAGING SYSTEM USING NONUNIFORM FFT	31
ABSTRACT.....	31
1. INTRODUCTION	31
2. CS ALGORITHMS FOR 3D SAR	34
3. ACCURATE SAR AND R-SAR TRANSFORMS.....	40
4. EXPERIMENTS AND RESULTS.....	50
4.1. RUBBER PADS IN FOAM - SPECIMEN 1	50
4.1.1. Experiment	50
4.1.2. Results	51
4.2. RUBBER PADS IN SAND - SPECIMEN 2	54
4.2.1. Experiment	54
4.2.2. Results	54
4.3. REBAR IN CEMENT-BASED MATERIALS - SPECIMEN 3	56
4.3.1. Experiment	56
4.3.2. Results	56
5. CONCLUSION.....	57
6. APPENDIX (MATRIX REPRESENTATION OF SAR TRANSFORM) ...	58
7. ACKNOWLEDGMENT.....	60
III. ADAPTIVE BASIS SELECTION COMPRESSED SENSING	61
ABSTRACT.....	61
1. INTRODUCTION	61
1.1. APPLICATIONS	64
2. FIXED BASIS AND BEST BASIS CS FOR IMAGE PROCESSING	65
2.1. FIXED BASIS	65
2.2. BEST BASIS AND DICTIONARY LEARNING	66
3. ADAPTIVE BASIS SELECTION (ABS) COMPRESSED SENSING.....	68
3.1. STRATEGY	68
3.2. PROPOSED ABS ALGORITHM.....	70
3.3. COMPUTATIONAL COMPLEXITY	73
3.4. SPARSITY METRIC	74
3.5. COHERENCE	76
4. APPLICATION TO WIDEBAND 2D SAR IMAGING	76
4.1. SYNTHETIC APERTURE RADAR IMAGING.....	77

4.2. RESULTS	80
5. APPLICATION TO <i>K</i> -SPACE IMAGING	82
5.1. <i>K</i> -SPACE IMAGING	82
5.2. RESULTS	84
6. CONCLUSION.....	86
7. ACKNOWLEDGMENT.....	88
IV. QUANTITATIVE AND QUALITATIVE COMPARISON OF SAR IMAGES FROM INCOMPLETE MEASUREMENTS USING COMPRESSED SENSING AND NONUNIFORM FFT	89
ABSTRACT.....	89
1. INTRODUCTION	89
2. NUFFT SAR.....	90
3. DATA RECOVERY USING CS	92
4. EXPERIMENTAL TESTS AND RESULTS.....	93
5. CONCLUSION.....	101
V. 3D IMAGE RECONSTRUCTION FROM SPARSE MEASUREMENT OF WIDEBAND MILLIMETER WAVE SAR EXPERIMENTS	102
ABSTRACT.....	102
1. INTRODUCTION	102
2. WIDEBAND MONOSTATIC SAR IMAGING.....	103
3. APPLICATION OF CS TO WIDEBAND SAR.....	105
4. EXPERIMENTAL TESTS AND RESULTS.....	106
5. CONCLUSION.....	111
6. ACKNOWLEDGMENT.....	111
SECTION	
2. CONCLUSIONS	112
3. PUBLICATIONS	114
BIBLIOGRAPHY	115
VITA	120

LIST OF ILLUSTRATIONS

Figure	Page
SECTION	
1.1 The schematic of a SAR-based microwave imaging system.....	2
PAPER I	
1 Schematic of synthetic aperture radar system imaging a flaw inside a composite using uniform raster scanning.	12
2 Scan path for 5% of the spatial points (red dots are measurement points and blue lines are traveled path by the probe).	15
3 Photo and schematic of sample 1.....	16
4 2D SAR images of sample 1 from full-set data, 30%, and 20%random points reconstructed by BP and OMP (CFDR).....	22
5 3D SAR images of sample 1	23
6 Slices of 3D SAR images of sample 1 from full-set data, 30%, and 20% random points reconstructed by BP and OMP (CFAR).....	24
7 Figures of merit for SAR images of sample 1.....	26
8 CS processor and scanner performance for sample 1.....	27
9 Corrosion under paint experiment (sample 2).	29
PAPER II	
1 The schematic of a SAR-based microwave imaging system.....	35
2 Optimal path vs. raster scanning path for 5% random undersampling.	37
3 The block diagram of SAR and R-SAR using NUFFT for the proposed algorithm.	41
4 Truncation error in SAR and R-SAR with NUFFT.....	45
5 Illustration of nonuniform mapping of k_z with $k_y = 0$ and uniformly spaced k_x and ω	48
6 Accumulated errors in $f(x, y, \omega)$ after each SAR and R-SAR transform pair using NUFFT with and without truncation repair.	49
7 The block diagram of iterations for orthogonal basis.	51

8	Schematic of the rubber pads in the scanned area of Specimen 1, where unit in figure is mm, and z is the distance from the probe (not to scale). .	52
9	Slices of 3D SAR images of Specimen 1 from complete data and recovered data from 20% randomly selected points.	53
10	Schematic of the rubber pads in sand in the scanned area of Specimen 2, where unit in figure is mm, and z is the distance from the probe (not to scale).	54
11	Slices of 3D SAR images of Specimen 2 from complete data and recovered data from 30% randomly selected points.	55
12	Schematic of the rebars in mortar in the scanned area of Specimen 3, where unit in figure is mm (not to scale).	56
13	Slices of 3D SAR images of Specimen 3 from complete data and recovered data from 30% randomly selected points.	57

PAPER III

1	2D SAR images of the SUT from complete data and recovered using fixed bases from 20% randomly selected points at $z = -28$	81
2	2D SAR images of the SUT from complete data and recovered data from 20% randomly selected points using ABS.	83
3	Decision metric and error vs. number of iterations for SAR data.	84
4	Basis convergence vs. number of iterations for SAR data for different basis initialization.	84
5	Shepp-Logan phantom images from complete data and recovered using fixed bases from 30% randomly selected frequency points.	85
6	Shepp-Logan phantom images from complete data and recovered data from 30% randomly selected frequency points.	86
7	Decision metric and error vs. number of iterations for Shepp-Logan phantom data.	86
8	Basis convergence vs. number of iterations for Shepp-Logan phantom data for different basis initialization.	87

PAPER IV

1	Schematic of scanned area of SUT, where unit in figure is mm.	94
2	Normalized RMS error for 3D images reconstructed from experimental data using CS and NUFFT.	95

3	Weber contrast of 3D images reconstructed from experimental data using CS and NUFFT.....	95
4	RMS contrast of 3D images reconstructed from experimental data using CS and NUFFT.....	96
5	SNR of 3D images reconstructed from experimental data using CS and NUFFT.....	96
6	Wideband SAR images.....	99
7	Slices of wideband SAR images of full data set (unit in the figure is mm).	100
8	Slices of wideband SAR images from incomplete data using CS (unit in the figure is mm).	100
9	Slices of wideband SAR images from incomplete data using NUFFT SAR (unit in the figure is mm).	101
PAPER V		
1	Schematic of imaging system setup configuration.	104
2	Locations of the rubber pads in the scanned area of SUT, where unit in figure is mm, and z is the distance from the SAR probe.	107
3	Wideband SAR images.....	108
4	Slices of reconstructed wideband SAR images using measured data as in Fig. 3. Unit in the figure is mm.	109
5	Normalized RMS error for 3D images reconstructed by the DFT and DCT CS methods.....	110
6	Number of iterations for 3D images reconstructed by the DFT and DCT CS methods.	110

LIST OF TABLES

Table	Page
PAPER II	
1 Slope of NRMS error curves vs. iteration	49
2 CS model parameters for three sets of experiments.....	52
PAPER III	
1 Sets of bases	77

1. INTRODUCTION

1.1. BACKGROUND

Microwave and millimeter wave imaging are effective nondestructive testing and evaluation (NDT&E) methods with important applications in testing critical structures such as spacecraft tiles, airplane coating, bonding of either adhesive or composite materials, etc. [1] They have the potential to both inspect and evaluate a wide range of non-conducting (i.e., dielectric) materials and composites [2]. These NDT&E methods are varied and may be implemented in many different ways depending on the type of indication, properties of the structure, desired measurement resolution, etc.

Microwave synthetic aperture radar (SAR) imaging techniques have shown great potential for a variety of NDT applications. These applications involve the detection of discontinuities and defects in many critical structures [1,3–6]. Because of the high resolution imaging capability of synthetic aperture radar technology, a wideband 3D SAR imaging system is capable of detecting tiny defects of millimeter size embedded within the specimen under test (SUT) without compromising either the usefulness or utility of the SUT [7]. The wideband SAR is capable of determining the depth of discontinuities and providing 3D images of SUTs.

Conventionally, the microwave SAR imaging techniques used for nondestructive testing applications utilize raster scanning. The scanning system uses a single antenna probe (commonly an open-ended waveguide) over the SUT [1,4,5]. In this method, the scanner begins measurements at one point on the SUT and scans on a 2D spatial grid of uniform points in a raster way while collecting coherent (magnitude and phase) reflection coefficient data. Subsequently, using a robust SAR algorithm, either 2D or

3D SAR images of the SUT are produced. Focusing on the target location using the SAR algorithm at a single frequency results in a 2D image of the SUT at that location. Image quality can be significantly improved by coherently averaging focused data from several frequencies. Alternatively, 3D SAR images (i.e., holographical images) may be produced using wideband measured data from the SUT.

The schematic of a SAR imaging system inspecting an SUT in an XYZ-Cartesian space is given in Fig. 1.1. In this figure, the probe is scanning the SUT where a stratified medium is assumed. This medium consists of two layers with a relative permittivity of $\bar{\epsilon}_r$ and ϵ_r , respectively. The standoff distance between the probe and the surface of the SUT is Z_0 . The raster scanner moves along X and Y with uniform steps. The scanner stops at each (x_f, y_f) location. The probe then measures the complex reflection coefficients for each angular frequency ω_i , uniformly spaced in $[\omega_{\min}, \omega_{\max}]$, with a step size of $\Delta\omega$.

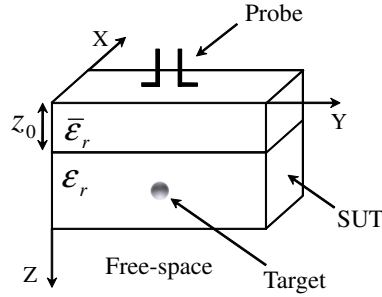


Figure 1.1: The schematic of a SAR-based microwave imaging system.

The measured reflection coefficients are denoted $f(x, y, \omega)$, with (x, y, ω) taken from the set $\mathcal{S}_f = \{(x_q, y_q, \omega_q)\}_{q=1}^{N_f}$, where N_f is the number of uniformly spaced measurements. To reconstruct the image from the full-set measurements, a phase adjustment operator \mathcal{I} is used to convert the measurement to the $\omega - k$ space. The

$\omega - k$ space data is corresponding to the surface of the second layer of the stratified medium as

$$F(k_x, k_y, \omega) = \mathcal{I}[f(x, y, \omega)] = \mathcal{F}_{2D} \{f(x, y, \omega)\} \exp \left[-jz_0 \sqrt{(2\omega/\bar{v})^2 - k_x^2 - k_y^2} \right] \quad (1)$$

where (k_x, k_y, ω) is also in the set $\{(k_{x,q}, k_{y,q}, \omega_q)\}_{q=1}^{N_f}$, $\mathcal{F}_{2D}\{\cdot\}$ is the two dimensional discrete Fourier transform (DFT), $\bar{v} = c/\sqrt{\varepsilon_r}$ is the wave propagation speed in the first layer (with c being the propagation speed of light in free-space), and k_x - k_y (and k_z) are the frequency components in the X-Y (and Z) dimensions, respectively.

Once these measurements have been converted, a forward SAR transform computes the high-resolution, uniformly-spaced volumetric image $s(x, y, z)$ from $F(k_x, k_y, \omega)$ by the NUFFT-based SAR algorithm [8–10]

$$s(x, y, z) = \mathcal{F}_{2D}^{-1} \left\{ \mathcal{F}_{NU}^{-1} \{F(k_x, k_y, \omega)\} \right\} \quad (2)$$

where $\mathcal{F}_{2D}^{-1}\{\cdot\}$ is the two dimensional inverse DFT and $\mathcal{F}_{NU}^{-1}\{\cdot\}$ is the one dimensional inverse NUFFT along k_z . The image $s(x, y, z)$ in (2) is defined on the set of N_s uniformly sampled locations $(x, y, z) \in \{(x_r, y_r, z_r)\}_{r=1}^{N_s}$. It is vectorized as \mathbf{s} , where N_s is the number of SAR image voxels. The forward SAR transform is formulated into a matrix form as

$$\mathbf{s} = \mathbf{\Omega} \mathbf{f} \quad (3)$$

where $\mathbf{f} \in \mathbb{C}^{N_f}$ is the vectorized measurement $f(x, y, \omega)$ and $\mathbf{\Omega} \in \mathbb{C}^{N_s \times N_f}$ is the forward SAR transform matrix for the stratified medium, combining the operators \mathcal{I} , $\mathcal{F}_{2D}^{-1}\{\cdot\}$, and $\mathcal{F}_{NU}^{-1}\{\cdot\}$. Note that the XY-coordinates (x_s, y_s) in the image space may be

selected consistently with (x_f, y_f) in the measurement space. The SAR transform may also be implemented by other $\omega - k$ algorithms, such as the Stolt transform [11–13].

1.2. PROBLEM STATEMENT

Although SAR imaging has tremendous applicability for NDT applications, conventionally it requires a significant amount of time to acquire the coherent reflection coefficients while scanning the region of interest. This long acquisition time is a result of the spatial movement of the probe acquiring the reflection coefficients from uniform spatial points with small step size for high spatial resolution. This acquisition time is further exasperated when wideband measurements are taken to produce 3D images (i.e., longer time to also step through the measured frequency band). For example, a $120 \text{ mm} \times 180 \text{ mm}$ SUT requires a data acquisition time of approximately 50 minutes if uniform spacing with a step size of 2 mm is used. For a relatively large SUT, the data acquisition might require hours of acquisition time. Therefore, it is of practical interest to reduce the acquisition time.

Reducing the number of spatial samples significantly helps decrease the acquisition time. Spatial sample reduction, however, leads to a reduction in spatial resolution. Recently, compressed sensing (CS) has been used to reduce the sampling rate below the Nyquist rate while guaranteeing perfect recovery from sub-Nyquist measurements if the required conditions are satisfied [14–18]. In this research, we proposed incorporating compressed sensing theory to significantly reduce the number of spatial samples needed to produce both 2D and 3D SAR images. This results in a substantially shorter data acquisition time.

In compressed sensing theory, the sub-Nyquist sampling of a signal is achieved by utilizing a sparse representation of the signal with an orthogonal basis. Consider signal $\mathbf{f} \in \mathbb{C}^N$ and its transform coding \mathbf{c} with an orthonormal basis $\Psi = [\psi_1 \psi_2 \dots \psi_N]$, such that $\mathbf{f} = \Psi \mathbf{c}$. If most of the signal's information is contained within only a few

elements of the transformed signal \mathbf{c} , signal \mathbf{f} is called *S-sparse* in basis Ψ if only S of its coefficients are significant and the rest $(N - S)$ coefficients are zero. Therefore, a fixed signal support T of size $|T| = S$ can form an *S-sparse* signal such that

$$S = \|\mathbf{c}\|_0 \quad (4)$$

where $\|\cdot\|_0$ is the ℓ_0 pseudo-norm operator and counts the nonzero elements of the vector of coefficients \mathbf{c} .

In compressed sensing, the sparsity of the signal is used to sample the signal \mathbf{f} more efficiently by measuring $M < N$ linear combinations. Let us define the measurement matrix $\Phi_\Omega \in \mathbb{R}^{M \times N}$ by selecting the rows of a measurement matrix $\Phi \in \mathbb{R}^{N \times N}$ on a set $\Omega \subset \{1, 2, \dots, N\}$ with the size $|\Omega| = M$ where Φ is modeling the linear measurement procedure. The linear measurement procedure can be modeled in matrix form as

$$\mathbf{y} = \Phi_\Omega \mathbf{f} \quad (5)$$

where \mathbf{y} is the measured signal. The inverse problem involves recovering the original signal from linear measurements. In general, this inverse problem is underdetermined with infinite solutions which satisfy (5). In compressed sensing, the sparsity of the signal is used to find a unique sparse solution for this problem.

Compressed sensing is similar to the decoding procedure in transform coding; both estimate the signal by applying the inverse of the encoder orthonormal basis Ψ on the sparse coefficients \mathbf{c} supported on set T . CS differs from transform coding as both the location of support T and the value of the coefficients at these locations \mathbf{c}_T are unknown. The only known variable is a sampled linear combination of the signal.

The sparsity of the signal helps solve the system of equations (5) by searching for the sparsest coefficients \mathbf{c} which matches the incomplete measurement signal \mathbf{y} .

By defining both $\mathbf{A} = \Phi\Psi$ and $\mathbf{A}_\Omega = \Phi_\Omega\Psi$, this process can be formulated as

$$\min_{\mathbf{c} \in \mathbb{C}^N} \|\mathbf{c}\|_1 \quad \text{subject to} \quad \mathbf{y} = \mathbf{A}_\Omega \mathbf{c}. \quad (6)$$

Convex optimization (6) is guaranteed to recover \mathbf{f} with a high probability from linear measurements if some conditions are satisfied [16]. The minimum number of linear measurements guaranteeing perfect recovery is related to both the sparsity of the signal and the coherence between the measurement and sparsifying bases. The coherence $\mu(\Phi, \Psi)$ between the measurement matrix Φ and transform matrix Ψ is defined as

$$\mu(\Phi, \Psi) = \sqrt{N} \max_{1 \leq u, v \leq N} |\langle \phi_u, \psi_v \rangle|. \quad (7)$$

The coherence is an indication of how correlated the measurement and the sparsifying bases are.

Three CS approaches are proposed for reconstruction of the wideband microwave SAR-based imaging systems. The first approach reconstructs a full-set of raw data from undersampled measurements via L1-norm optimization. It then applies 3D forward SAR on the reconstructed raw data as post-processing to form the 3D SAR image. The second proposed approach employs forward SAR and reverse SAR (R-SAR) transforms in each L1-norm optimization iteration reconstructing images directly. The truncation error, along with the SAR and R-SAR transform error, is identified as a critical obstacle to the convergence of the CS iterative algorithm and the quality of the reconstructed images. This dissertation proposes a simple, elegant truncation repair method to combat the truncation error. It utilizes a nonuniform fast Fourier transform (NUFFT) to reduce the SAR and R-SAR transform errors. The third proposed CS reconstruction algorithm is the adaptive basis selection (ABS) compressed sensing. Rather than a fixed sparsifying basis, the proposed ABS method adaptively

selects the best basis from a set of bases in each iteration of the L1-norm optimization according to a proposed decision metric that is derived from the sparsity of the image and the coherence between the measurement and sparsifying matrices.

1.3. SUMMARY OF CONTRIBUTIONS

This dissertation addresses the technical challenges of applying compressed sensing on microwave and millimeter wave SAR-based 3D imaging systems. This research has been presented in two conference papers, one journal publication, and two journal submissions listed under publications list. The published and expected contributions include the following:

1. Compressed sensing methodology is successfully applied to a 3D SAR imaging system. Several sets of experiments are performed on different specimens to evaluate the performance of the CS algorithm. Benefiting from a reduced number of samples, we propose two scanning procedures, namely nonuniform raster and optimum path. Our experiments show that a 120 mm \times 180 mm SUT requires data acquisition time of approximately 50 minutes to measure 5551 points if uniform spacing is used with step size of 2 mm. In contrast, our proposed CS technique measuring 20% of random spatial points uniformly selected from the full dataset requires only 17 minutes of scanning and achieving comparable quality as the one obtained using the full dataset.
2. A new compressed sensing image reconstruction method is proposed for high-resolution wideband 3D SAR imaging systems. In contrast to existing CS SAR methods that employ only a forward SAR transform in pre- or post-processing, the proposed method employs both forward SAR and reverse SAR (R-SAR) transforms in each CS iteration to improve the quality of reconstructed images. The truncation error, along with both the SAR and R-SAR transform error, is

identified as a critical obstacle to the convergence of the CS iterative algorithm and the quality of the reconstructed images. This study proposes a simple and elegant truncation repair method to combat the truncation error. It utilizes NUFFT to reduce both the SAR and R-SAR transform errors. The proposed CS SAR method is applied to microwave and millimeter wave imaging systems for the nondestructive evaluation of materials embedded in stratified media. The results of the CS reconstructed images show that the proposed method improves the quality of the final SAR images. Also, it reduces the background artifacts in comparison with the images reconstructed from the original fully sampled measurements.

3. In this research, the adaptive basis selection (ABS) compressed sensing method is proposed. In contrast to conventional compressed sensing with fixed sparsifying basis, the proposed ABS method adapts the basis to the image as the image evolves during the algorithm iterations. In this method, the sparsifying basis is selected from a set of bases based on information from incomplete measurements without any *a priori* knowledge of a proper basis. The algorithm benefits from the ability to search through a diverse set of bases for unknown signals. A decision metric is introduced based on both the sparsity of the image and the coherence between the measurement and sparsifying matrices. This decision metric makes the adapting process possible for practical applications. The results of our experiments show that the proposed algorithm is capable of recovering 2D SAR images very well without compromising the complexity of the recovery process. Additionally, the algorithm indicates promising results for k -space imaging techniques.
4. The proposed compressed sensing method for random sample reduction is both qualitatively and quantitatively compared with conventional nonuniform fast

Fourier transform (NUFFT) undersampling method. The results of our study show that CS-based undersampling significantly improves the quality of 3D SAR images. Solving the ℓ_1 norm minimization for CS, however, increases the overall complexity of SAR image reconstruction. Therefore, the SAR image quality improvement using CS is with the cost of higher computational complexity.

PAPER

I. IMPROVING EFFICIENCY OF MICROWAVE WIDEBAND IMAGING USING COMPRESSED SENSING TECHNIQUES

Hamed Kajbaf, Yahong Rosa Zheng, and Reza Zoughi

ABSTRACT—A compressed sensing (CS) technique is developed for wideband microwave synthetic aperture radar (SAR) imaging techniques, particularly suitable for nondestructive testing applications. This technique helps to significantly reduce the number of spatial measurement points and consequently the acquisition time by sampling at lower than the Nyquist-Shannon rate. The reduced measurement data are processed to reconstruct SAR images via basis pursuit and orthogonal matching pursuit using discrete cosine transform sparse representation. Benefiting from a reduced number of samples, we propose two scanning procedures, namely; nonuniform raster and optimum path. Two sets of experiments are conducted to show the performance of the proposed method. The first set of experiments is performed on a $120\text{mm} \times 180\text{mm}$ area with thin rubber and copper patches placed on foam posts in the 18 GHz to 26.5 GHz frequency band (K-band) using conventional raster scanning and the proposed CS sampling methods. Conventional raster scanning with step size of 2 mm requires 2947 seconds to measure the 5551 points. In contrast, the proposed CS technique measuring 20% of random spatial points uniformly selected from the full dataset requires only 1020 seconds of scanning and achieves comparable quality as the one obtained using the full dataset. Another set of experiments is performed on corrosion under paint sample. The results of this experiment show that we can detect the corrosion very well by measuring only 20% of the full dataset. This paper describes the CS algorithm as well as the measurement technique and the obtained results.

1. INTRODUCTION

Microwave nondestructive testing (NDT) techniques have shown tremendous potential for inspecting and evaluating a wide range of non-conducting (i.e., dielectric) materials and composites [2]. These techniques are varied and may be implemented in many different ways depending on the type of indication, properties of the structure, desired measurement resolution, etc. Incorporation of imaging techniques gives visual information that may also be analyzed for property characterization. To this end, microwave synthetic aperture radar (SAR) imaging techniques have shown great potential for a variety of NDT applications involving the detection of discontinuities and defects in many critical structures [1, 3–6]. Conventionally, microwave SAR images are produced by raster scanning the measurement probe (commonly an open-ended waveguide) over the specimen under test (SUT), with uniform spatial step size, while coherent (magnitude and phase) reflection coefficient data is collected. Subsequently, using a robust SAR algorithm, 2D or 3D SAR images of the SUT are produced. Focusing on the target location using a SAR algorithm at a single frequency results in a 2D image of the SUT at that location. Image quality can be significantly improved by coherently averaging focused data from several frequencies. Alternatively, 3D SAR images (i.e., holographical images) may be produced using wideband measured data from the SUT. The schematic of a SAR imaging system, which uniformly raster scans a composite structure is shown in Figure 1. Although SAR imaging has tremendous applicability for NDT applications, it conventionally requires a significant amount of time to acquire the coherent reflection data. This is further exasperated when wideband measurements are conducted for producing 3D images (i.e., longer time to also step through the measured frequency band).

In this paper we propose incorporating compressed sensing (CS) methodology to significantly reduce the number of spatial samples that is needed to produce 2D

and 3D SAR images, resulting in a substantially shorter data acquisition time. In addition, the implementation of nonuniform and optimum path raster scanning can further aid in reducing this time. Finally, basis pursuit (BP) and stagewise orthogonal matching pursuit (StOMP) methods are used to recover the data from the nonuniform/random measurements [14, 19]. To illustrate the performance of the proposed methods, two sets of experimental tests are performed on two different samples. The first sample consists of small rubber and copper patches placed on construction foam posts producing a SUT with three dimensional geometrical variations. Subsequently, the performance of CS on 2D and 3D SAR imaging on this sample is qualitatively and quantitatively compared to show that the proposed method reduces the acquisition time significantly without compromising of the quality of the images. The other sample consists of a painted steel panel with a localized area of corrosion under the paint. The imaging results for this sample shows the performance of the proposed method for real world application of microwave SAR imaging.

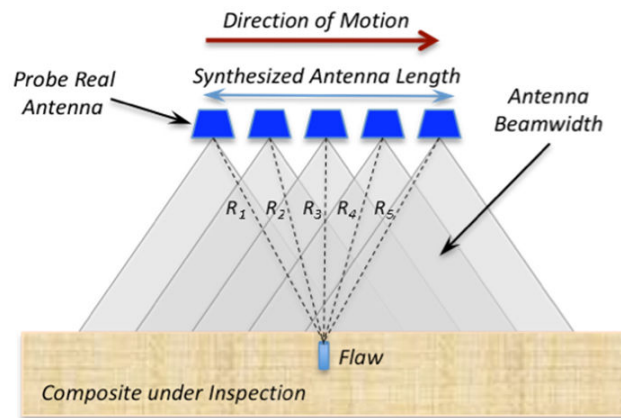


Figure 1: Schematic of synthetic aperture radar system imaging a flaw inside a composite using uniform raster scanning.

2. EXPERIMENTAL PROCEDURE

In the conventional uniform raster scanning approach for imaging the SUTs, the probe starts movement from point (x_0, y_0) and scans the scene with uniform step size by stopping at each (x_a, x_b) location to acquire the data. By incorporating the CS methodology, we are capable of scanning the same scene with a far less amount of measured data using nonuniform/random measurements and reconstructing the missing data using BP or OMP methods. This results in the number of measured data samples being much less than the uniformly sampled data (typically 70 to 80 percent less, as shown in this paper). In this paper we propose two scanning procedures called nonuniform raster (NUR) and optimum path (OptP) scanning which take advantage of undersampled measurements to significantly reduce the required time for scanning the SUTs. In both methods the probe acquires the data at random locations, which are designed and modeled by the measurement matrix, Φ , which will be introduced in the Compressed Sensing for SAR Imaging section. In nonuniform raster scanning, the measurement probe follows the raster path and stops only at random locations that are determined in advance. On the other hand, the optimum path method uses a genetic algorithm (GA) to find the shortest traveled distance by solving the "travelling salesman" problem. Using this approach further decreases the total scanning time and reduces the number of needed measurement points. Figure 2 shows the NUR along X, NUR along Y, and OptP scanning procedures for a $120\text{mm} \times 180\text{mm}$ scan area with step size of multiples of 2 mm. For better illustration, in this figure, we have only shown the path for acquiring only 5% of the needed measurement points.

An experimental setup is prepared to verify the performance of the proposed method. The SUT consists of eight thin rubber (Rbr) patches and one thin copper (Cu) patch placed on construction foam substrates with different heights, as shown in Figure 3a (sample 1). The top view and side view schematics of the sample are

shown in Figure 3b and Figure 3c, respectively. The imaging probe is a K-band open-ended waveguide, with an aperture dimension of 4.32 mm by 10.67 mm, located at 28 mm above the tallest target along the Z-axis. Since the sample substrate is located at 104 mm below the probe aperture (maximum range), the maximum frequency step size to image this scene is $\Delta f = c/(4R_{\max}) = 0.7$ GHz [13]. In our experiments, the measurements are performed using a swept-frequency approach [5], covering a range from 18 GHz to 26.5 GHz (K-band) with a frequency step size of 0.6 GHz. An area of 120mm \times 180mm is scanned and the calibrated coherent reflections are received by the same probe. Subsequently, the baseband complex-valued reflection coefficients are measured and recorded by an HP8510C vector network analyzer. The scanning platform is programmed and controlled by a PC through a National Instrument PCI-6254 data acquisition (DAQ) card. A LabVIEW program is used to perform the scan over the desired area by uniform raster, nonuniform raster, or optimum path scanning procedures. The LabVIEW program also performs the required synchronization between the scanner and the network analyzer. Finally, the acquired data is processed by CS processors to reconstruct the missing (or not measured) data and SAR processors are used to form the 2D or 3D images, respectively.

3. 2D AND 3D SAR IMAGING

Consider the antenna probe located at (x', y', z_0) transmitting a single frequency signal and illuminating a target. A general point, (x, y, z) , on the target reflects back the signal with round trip delay. The distance between the probe and the target point, R is then given by

$$R = \sqrt{(x - x')^2 + (y - y')^2 + (z - z_0)^2}. \quad (1)$$

The same probe acquires the backscattered microwave coherent reflection coefficients $f(x', y')$ which is the superposition of microwave reflections from all points in the illuminated area

$$f(x', y') = \iint s(x, y) e^{-jkR} dx dy \quad (2)$$

where $k = \frac{\omega}{c}$ is the wavenumber with ω being the temporal angular frequency and c the propagation speed. $s(x, y)$ is the 2D SAR image and is defined as the reflectivity function of the target, which is the ratio of the reflected to the incident field.

After decomposing the propagating spherical waves into superposition of several plane wave components, dropping the distinction between primed and unprimed coordinates, and solving for $s(x, y)$ we have [13]

$$s(x, y) = F_{2D}^{-1} \left\{ F_{2D} \{f(x, y)\} e^{-j\sqrt{4k^2 - k_x^2 - k_y^2} z_0} \right\} \quad (3)$$

where k_x and k_y are the Fourier transform variables corresponding to x and y , respectively, z_0 is the standoff distance of the probe which is the distance between the probe

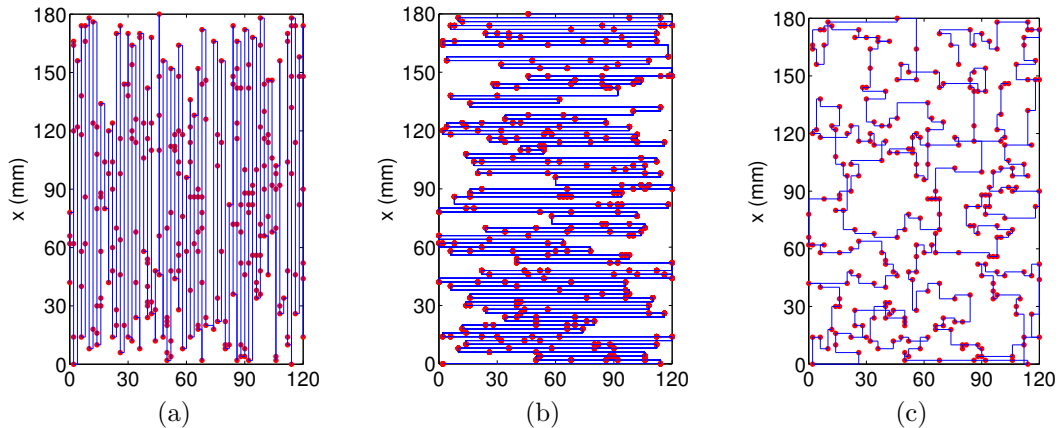
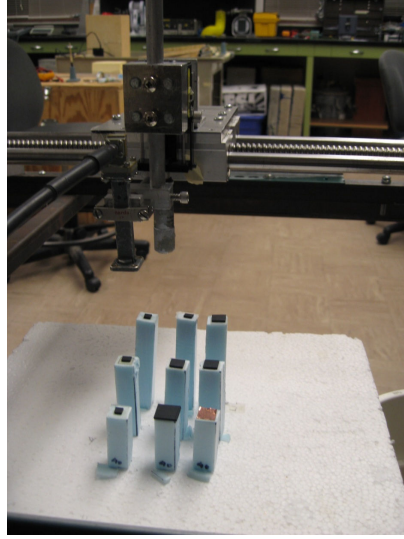
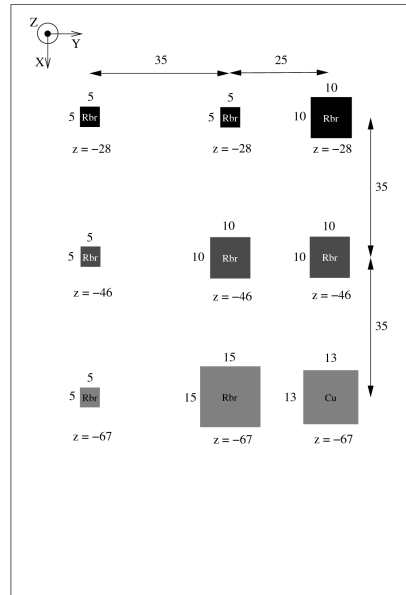


Figure 2: Scan path for 5% of the spatial points (red dots are measurement points and blue lines are traveled path by the probe) (a) nonuniform raster scan along X, (b) nonuniform raster scan along Y, (c) optimum scan.

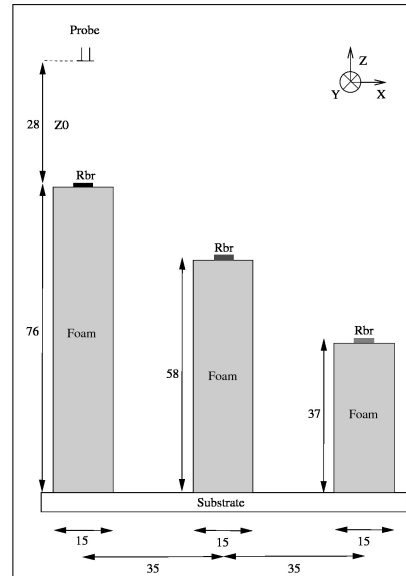
aperture and the targets, and $F_{2D}\{\cdot\}$ and $F_{2D}^{-1}\{\cdot\}$ denote the 2D Fourier transform and the 2D inverse Fourier transform, respectively [13]. To improve the quality of an image, we measure the reflection coefficients, $f(x', y', \omega)$, for a range of frequencies, as mentioned earlier. Then, we average over all focused images, $s(x, y, \omega_m, z_n)$, for



(a)



(b)



(c)

Figure 3: Photo and schematic of sample 1 (a) photo, (b) top view schematic, (c) side view schematic (unit in figures is mm).

different distances of the probe to the targets, z_n

$$s(x, y, z_n) = \frac{1}{N_\omega} \sum_{N=1}^{N_\omega} s(x, y, \omega_m, z_n) \quad (4)$$

where N_ω is the number of measured frequency points.

Expanding (2) to the case of wideband measurements we have

$$s(x, y, z) = F_{3D}^{-1} \left\{ F_{2D} \{f(x, y, \omega)\} e^{-j\sqrt{4k^2 - k_x^2 - k_y^2}z_0} \right\}. \quad (5)$$

where $s(x, y, z)$ is the 3D SAR image of the SUT and F_{3D}^{-1} is the 3D inverse Fourier transform.

The temporal angular frequency, ω , is uniformly sampled in the frequency band and the probe scans at uniform spatial step size. Consequently, the K_z 's are nonuniformly distributed and Stolt interpolation is usually used to achieve uniform K_z 's [9, 12, 13, 20]. Alternatively, the nonuniform fast Fourier transform (NUFFT) can be exploited to improve the performance and accuracy of SAR imaging since it is a good approximation of the nonuniform discrete Fourier transform [8, 21–24]. Therefore, (5) becomes

$$s(x, y, z) = F_{2D}^{-1} \left\{ F_{NU}^{-1} \left\{ F_{2D} \{f(x, y, \omega)\} e^{-j\sqrt{4k^2 - k_x^2 - k_y^2}z_0} \right\} \right\}. \quad (6)$$

where $F_{NU}^{-1}\{\cdot\}$ is the one dimensional inverse NUFFT operator in the k_z domain.

4. COMPRESSED SENSING FOR SAR IMAGING

Modern digital signal processing technology is based on the well-known Nyquist-Shannon sampling theorem, which states that the sampling rate must be at least twice the maximum frequency present in a band-limited signal for perfect recovery.

In practice, acquiring the signal with the Nyquist rate might be time-consuming, expensive, or inefficient. A better approach to acquire a signal is to measure it with the rate of its sparsity (i.e., information contained in the signal) rather than the rate of changes. Here, sparsity means that a few of the coefficients in the sparse domain are significant and the rest of them are zero or very close to zero. Recently, a theory called compressed sensing (CS) was developed to help data acquisition hardware measure the signal with the rate of sparsity [17, 18, 25–27].

Suppose that we need to measure the reflection coefficients, $f(x, y, \omega)$, vectorized in a vector of reflection coefficients, \mathbf{f} , by uniform raster scanning of a specimen under test. Consider an orthonormal basis

$$\Psi = [\boldsymbol{\psi}_1, \boldsymbol{\psi}_2, \dots, \boldsymbol{\psi}_N] \quad (7)$$

consisting of the $N \times 1$ vectors $\boldsymbol{\psi}_u$ vectors as bases. The signal, \mathbf{f} , can be expanded in this basis as

$$\mathbf{f} = \Psi \mathbf{c} \quad (8)$$

where \mathbf{c} is vector of atoms

$$c_r = \langle \mathbf{f}, \boldsymbol{\psi}_u \rangle = \boldsymbol{\psi}_u^H \mathbf{f} \quad (9)$$

and $(.)^H$ denoting conjugate transpose. The signal \mathbf{f} is called *S-sparse* if it can be represented by S most significant c_r coefficients. In this paper the 2D discrete cosine transform (DCT) is used as the sparsifying transform for the 2D SAR imaging and the 3D discrete cosine transform is used for wideband measurements to form the 3D images.

We designed an $M \times N$ linear measurement matrix Φ with $M < N$ to under-sample \mathbf{f} . This matrix is designed to have a “one” randomly placed in each row with the rest of elements being zero. The ones are uniformly distributed according to the corresponding (x, y) probe location. This means the measurement probe only stops at a fractional number of (x, y) points that are required by full sampling of conventional methods. For each selected location, we use all of the frequency points in \mathbf{f} because reducing the number of frequency points does not save measurement time but complicates the data acquisition control and increases the complexity of image reconstruction. The measurement and sparsifying procedure can then be modeled as

$$\mathbf{y} = \Phi \mathbf{f} = \Phi \Psi \mathbf{c} = \mathbf{A} \mathbf{c} \tag{10}$$

where \mathbf{y} is the undersampled measured signal and $\mathbf{A} = \Phi \Psi$ is the measurement and sparsifying matrix together.

Now the problem is to solve the underdetermined system of equations (10) for \mathbf{c} . Using (8) we can find the original signal \mathbf{f} . In general an underdetermined system of equations has infinite solutions, but if $S \ll N$, Ψ and Φ are incoherent, and matrix \mathbf{A} has restricted isometry property (RIP) we can find \mathbf{f} perfectly [17]. This can be done through a range of techniques from linear programming to greedy algorithms. In this paper we use two recovery techniques: basis pursuit (BP) [19] and orthogonal matching pursuit (OMP) [14]. BP is a linear programming algorithm which minimizes the ℓ_1 norm of coefficients \mathbf{c} with the constraint that the solution matches the undersampled measurements

$$\min_{\mathbf{c} \in \mathbb{C}^N} \|\mathbf{c}\|_1 \quad \text{subject to} \quad \mathbf{y} = \mathbf{A} \mathbf{c} \tag{11}$$

where $\|\cdot\|_1$ denotes the ℓ_1 norm and is defined as the sum of absolute values. It is shown that if \mathbf{c} is sparse; the minimization (11) recovers the signal \mathbf{f} with very high

probability. The probability of the recovery is directly related to the sparsity of \mathbf{c} and to the coherence $\mu(\Psi, \Phi)$ between Ψ and Φ defined as

$$\mu(\Psi, \Phi) = \sqrt{N} \max_{1 \leq u, v \leq N} |\langle \psi_u, \phi_v \rangle| \quad (12)$$

where ψ_u and ϕ_v are the columns of Ψ and Φ , respectively. The probability of recovery increases, if sparsity S and coherence μ decrease at the same time [17]. In this paper we use alternating direction method (ADM) to solve the dual of the ℓ_1 norm minimization (11) by minimizing the augmented Lagrangian of the problem [28]. On the other hand OMP methods are greedy algorithms which try to find an approximate sparse solution of $\mathbf{y} = \mathbf{A}\mathbf{c}$ iteratively. OMP methods usually have significantly lower computational complexity than BP, but typically need more signal samples to achieve the BP performance. In this paper we use stagewise orthogonal matching pursuit (StOMP). This method builds up a sequence of approximates of sparse solution \mathbf{c} by removing detected structure from a sequence of residual vectors through a hard thresholding scheme [14]. Two thresholding strategies are used in this paper based on constant false alarm rate (CFAR) and constant false discovery rate (CFDR). After the CS algorithm reconstructs the full data vector \mathbf{f} from undersampled measurements, the SAR image is formed via (5).

5. EXPERIMENTAL RESULTS AND DISCUSSIONS

5.1. 2D EXPERIMENTS

Specimen 1 is imaged by the 2D SAR technique using the full dataset with uniform raster scanning procedure. Then, the same SUT is scanned using 30% and 20% random spatial points. The undersampled measurements are recovered using

basis pursuit and stagewise orthogonal matching pursuit. The thresholding strategy for 2D imaging is CFDR. For this data CFAR does not converge especially for lower percentages. The resulting 2D images for the full dataset, 30%, and 20% random measurements are shown in Figure 4. This figure shows the SAR images focused on three different levels of the targets and images from substrate level. Since the recovery technique is independent of scanning procedure the images of nonuniform raster and optimum path scanning are exactly the same and are not shown here. This is while the scan time of the optimum path method is substantially less than the nonuniform raster scan for these percentages of data.

5.2. 3D EXPERIMENTS

The same specimen is imaged by the 3D SAR technique. Thirty percent and 20% random measurements are recovered by BP and StOMP techniques. For StOMP method, CFAR thresholding converges very well for data percentages below 60%. For larger data percentages, we need to switch to the CFDR thresholding strategy in order to achieve good convergence. This is due to different behavior of the two thresholding strategies as CFAR attempts to control the total number of false alarms and CFDR attempts to maintain the number of false discoveries below a fixed fraction of all discoveries. The resulting volumetric images of the full dataset, 30%, and 20% random measurements are shown in Figure 5. To see the details of the 3D images, slices of the images are shown in Figure 6. This figure shows the slices from three different levels of the targets and one slice from substrate level which has very low power.

5.3. FIGURES OF MERIT

Each data recovery method is evaluated in terms of image quality and computational complexity. Five metrics are defined to evaluate the image quality. The first

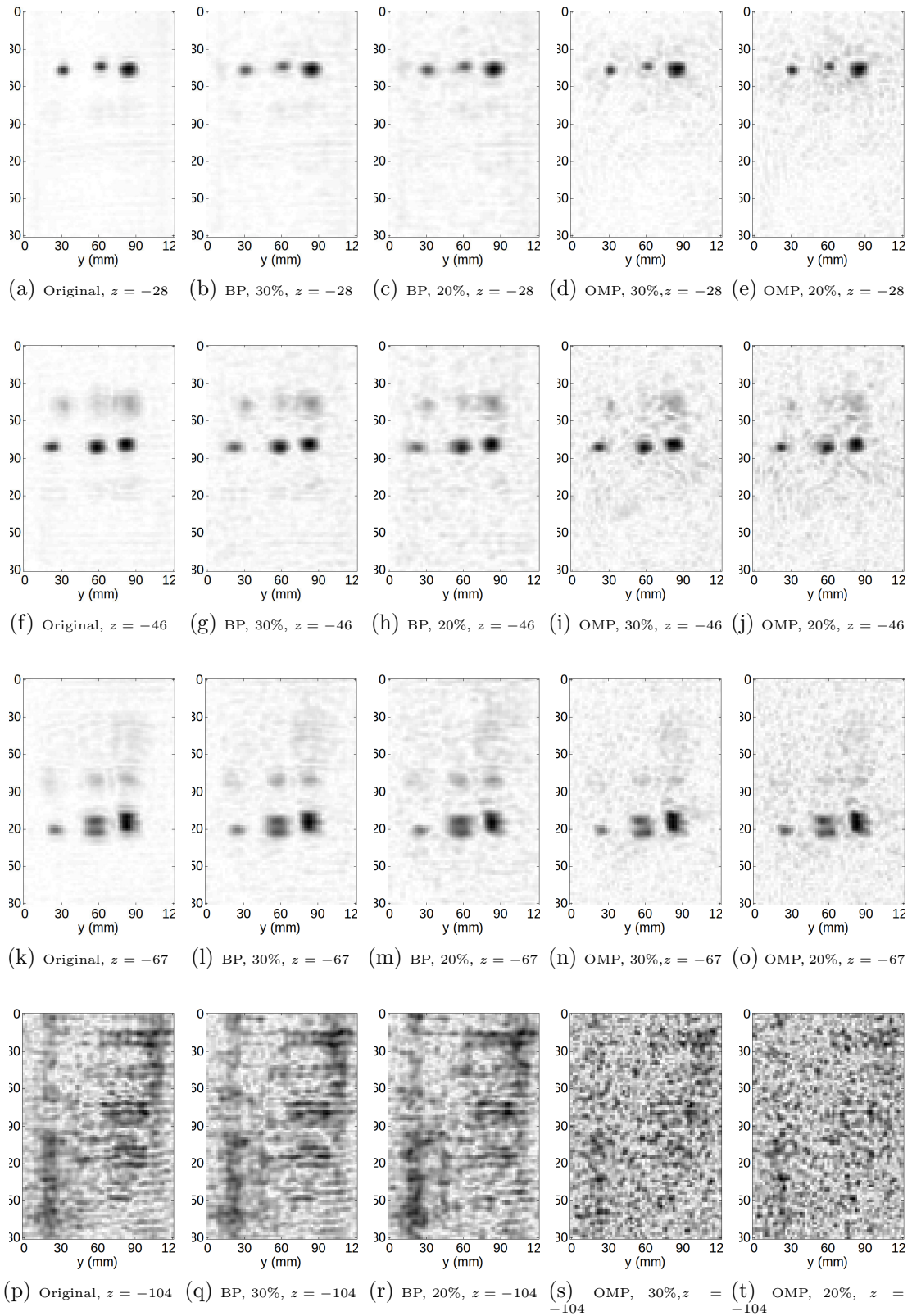


Figure 4: 2D SAR images of sample 1 from full-set data, 30%, and 20% random points reconstructed by BP and OMP (CFDR).

metric is the normalized root mean squared (NRMS) error of the reflection coefficients that is the Euclidean distance between the full-set data and the estimated one

$$\epsilon_{\mathbf{f}} = \left\| \mathbf{f} - \tilde{\mathbf{f}} \right\|_2 / \left\| \mathbf{f} \right\|_2 \quad (13)$$

where $\|\cdot\|_2$ is the ℓ_2 norm operator, \mathbf{f} is the vectorized full-set reflection coefficients, and $\tilde{\mathbf{f}}$ is the vectorized estimated reflection coefficients from incomplete data. The second metric is the NRMS of the SAR images

$$\epsilon_{\mathbf{s}} = \left\| \mathbf{s} - \tilde{\mathbf{s}} \right\|_2 / \left\| \mathbf{s} \right\|_2 \quad (14)$$

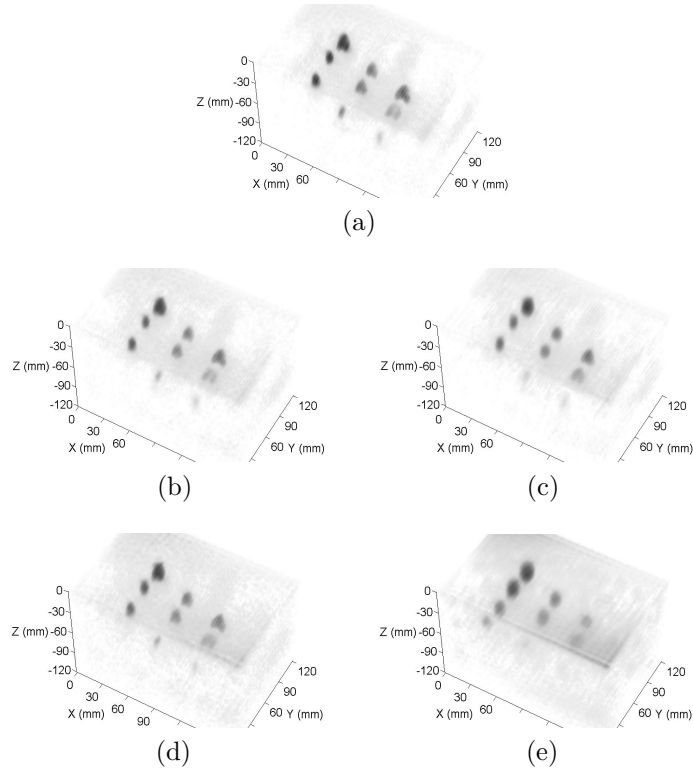


Figure 5: 3D SAR images of sample 1 (a) full-set data, (b) 30% random points using BP, (c) 30% random points using OMP (CFAR), (d) 20% random points using BP, (e) 20% random points using OMP (CFAR).

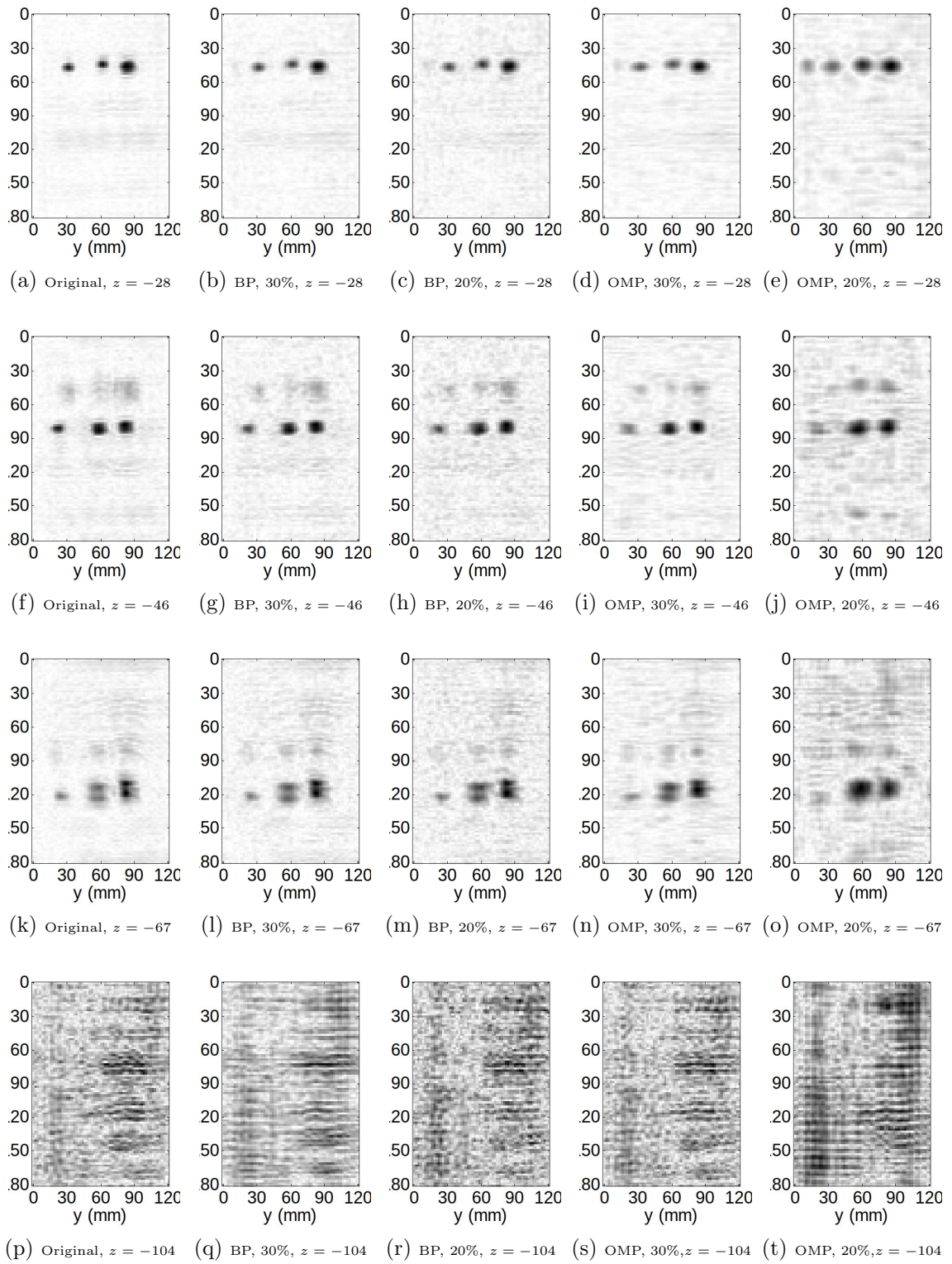


Figure 6: Slices of 3D SAR images of sample 1 from full-set data, 30%, and 20% random points reconstructed by BP and OMP (CFAR).

where \mathbf{s} is the vectorized full-set image and $\tilde{\mathbf{s}}$ is the vectorized image from incomplete data.

The third, fourth, and fifth metrics each quantify the SAR image from incomplete data in comparison to itself in terms of two types of contrast and signal-to-noise ratio (SNR). The contrast definitions used are Weber and root mean squared (RMS) contrasts. Weber contrast is usually used in cases where small targets are presented on a wide uniform background and is defined as the normalized difference between target and background intensity

$$C_w = |s_t - s_b| / s_b \quad (15)$$

where s_t is the target intensity and s_b is the plain background intensity [29]. On the other hand, RMS contrast does not use the spatial distribution of contrast since it is defined as the standard deviation of voxels intensity

$$C_{\text{rms}} = \left[\frac{1}{n-1} \sum_{i=1}^n (s_i - \bar{s})^2 \right]^{1/2} \quad (16)$$

where s_i is the intensity of each voxel, \bar{s} is the mean of voxels intensity, and n is the number of voxels in the image. SNR is the last metric utilized. It is defined as the ratio of the target intensity to background noise intensity in dB scale

$$\text{SNR} = 20 \log_{10} \left[\frac{s_{\text{max}} - s_{\text{min}}}{\sigma_s} \right] \quad (17)$$

where σ_s is the standard deviation of the image. The defined metrics are calculated for 2D and 3D SAR images. Figure 7 shows these metrics for 2D and 3D images for different recovery techniques.

The two approaches are also compared in terms of computational complexity and time required to estimate the image. The data processing is performed on a

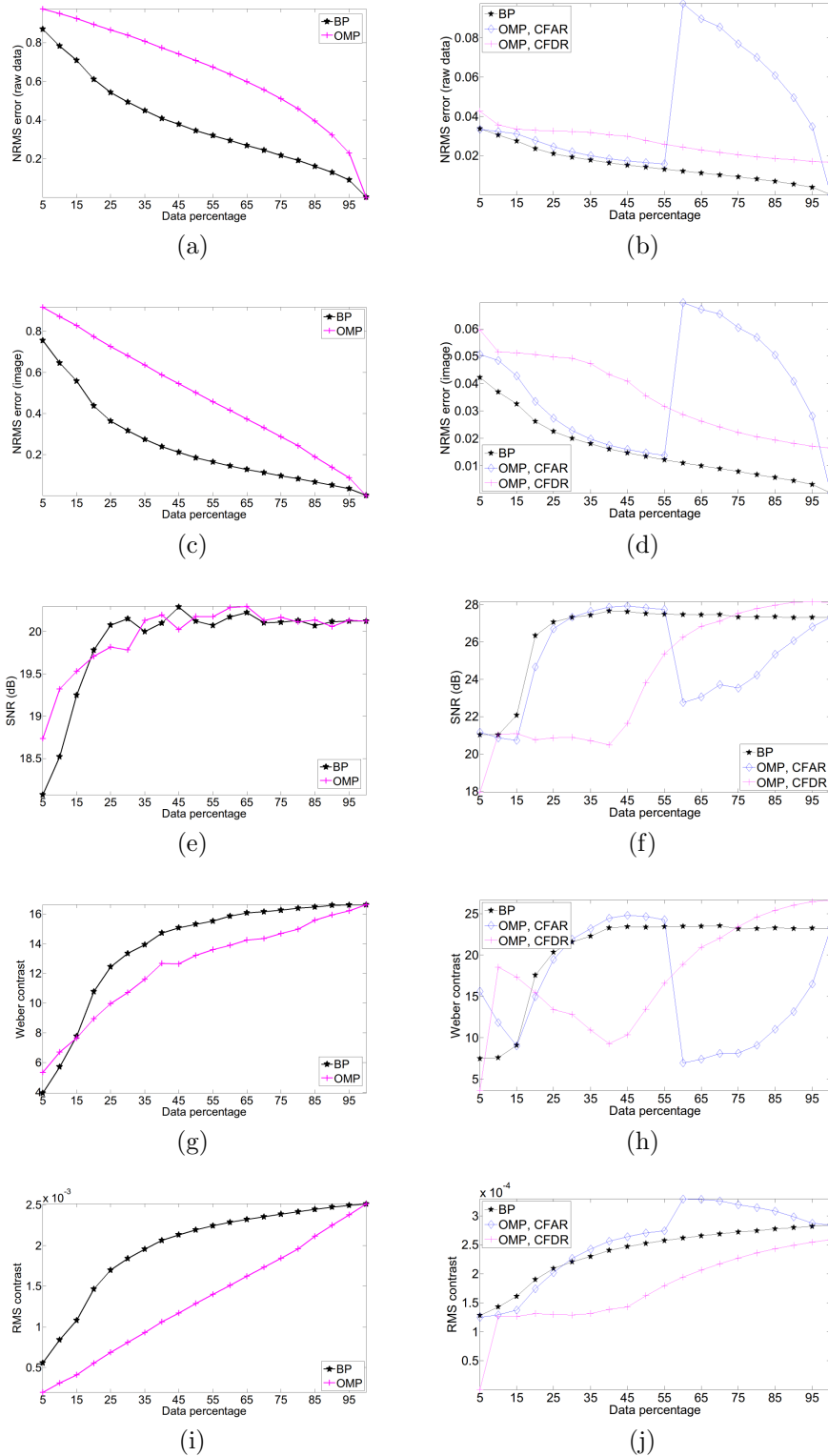


Figure 7: Figures of merit for SAR images of sample 1 (a) NRMS error of the raw data (2D), (b) NRMS error of the raw data (3D), (c) NRMS error of images (2D), (d) NRMS error of images (3D), (e) SNR of images (2D), (f) SNR of images (3D), (g) Weber contrast of images (2D), (h) Weber contrast of images (3D), (i) RMS contrast of images (2D), RMS contrast of images (3D).

personal computer with an Intel Core 2 Duo 3.33 GHz CPU and 8 GB Ram. For different percentages of data, Figure 8a-d illustrates the number of iterations and CPU time needed for data recovery for 2D and 3D SAR imaging. It can be seen that StOMP needs much fewer iterations than BP and recovers the data faster.

The scanning procedures performance is evaluated based on the time needed for scanning the whole SUT. Figure 8e illustrates the traveled distance by the scanner to scan the scene for different percentages of data. It also shows the traveled distance

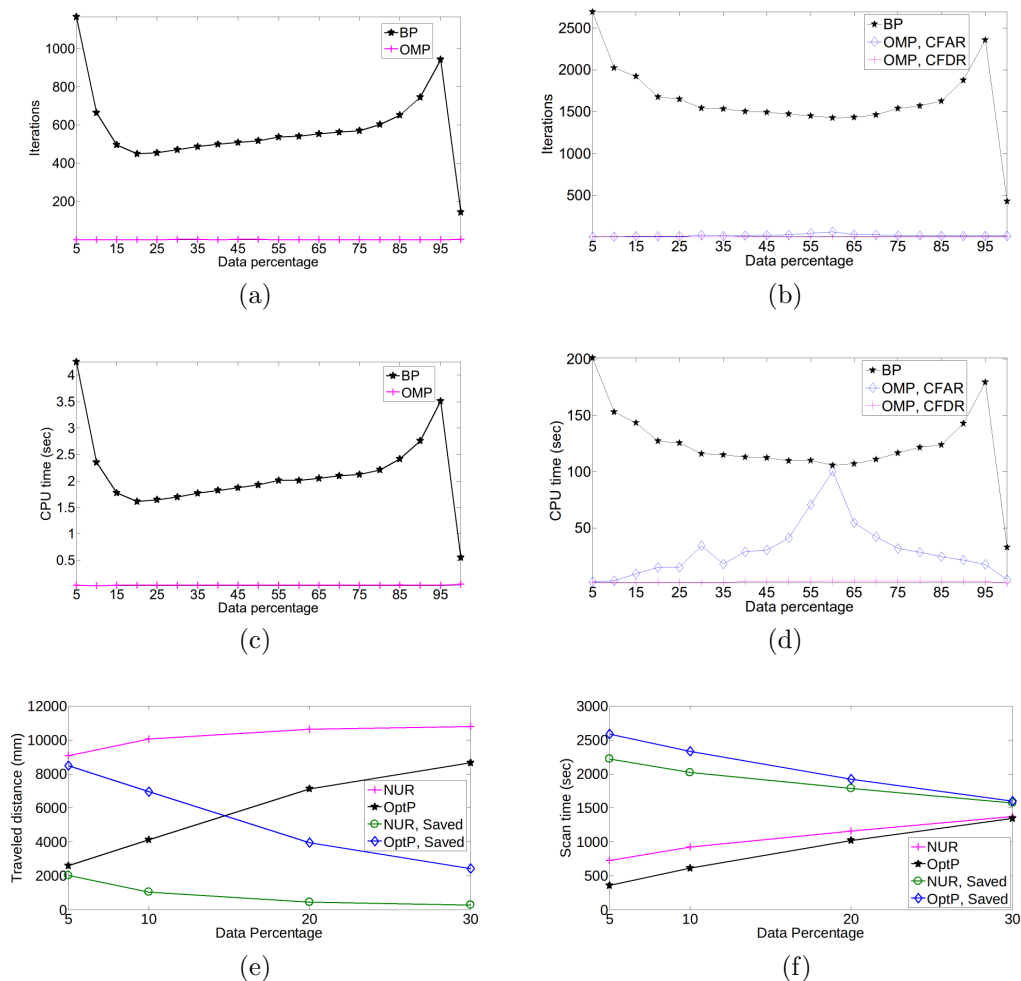


Figure 8: CS processor and scanner performance for sample 1 (a) number of iterations for 2D imaging, (b) number of iterations for 3D imaging, (c) CPU time for 2D imaging, (d) CPU time for 3D imaging, (e) traveled distance by the probe, (f) total scan time (NUR is along X).

which is reduced by incorporating the proposed scanning procedures. Figure 8f shows the scan time and the corresponding saved time for different percentages of data. It can be seen that scan time is reduced from 2947 seconds to 1020 seconds for 20% of measurement points using optimum path scanning. Because of hardware limitations, the measurement probe could not move diagonally and was limited to movement along x and y directions. Assuming that the probe could move diagonally, the acquisition time would have been reduced to as low as 722 seconds for 20% of measurement points.

5.4. CORROSION UNDER PAINT EXPERIMENT

To show the practical application of the proposed method two additional experiments are conducted on a corrosion under paint sample (sample 2). Figure 9a shows a steel sheet with a $40\text{mm} \times 40\text{mm}$ area of corrosion in it. The thickness of the corrosion layer is measured to be approximately 0.08 mm. This sample has a paint thickness of 0.60 mm of common spray paint, sprayed as uniformly as possible, as shown in Figure 9b. A complete description of the specimen can be found in [30]. The sample is measured at 18 GHz to 26.5 GHz with frequency step size of 0.6 GHz using an open-ended waveguide probe. The first experiment is conducted at a standoff distance of 1 mm while the second experiment is performed at standoff distance of 32 mm.

An $80\text{mm} \times 80\text{mm}$ area of the specimen is scanned with uniform raster, nonuniform raster, and optimum path procedures with a step size of multiples of 2 mm. Figure 9c-g show the 2D SAR images of both full and reconstructed from undersampled datasets for a standoff distance of 1 mm. Figure 9h-l show the same results for a standoff distance of 32 mm. It can be seen that basis pursuit with 2D DCT sparse representation has recovered the images very well even with 20% of data points. The uniform raster scan took 1029 seconds for this specimen. Measuring 30% of this data

takes 446 seconds and 460 seconds using nonuniform raster and optimum path, respectively. For 20% of the data, nonuniform raster and optimum path took 364 and 290 seconds, respectively.

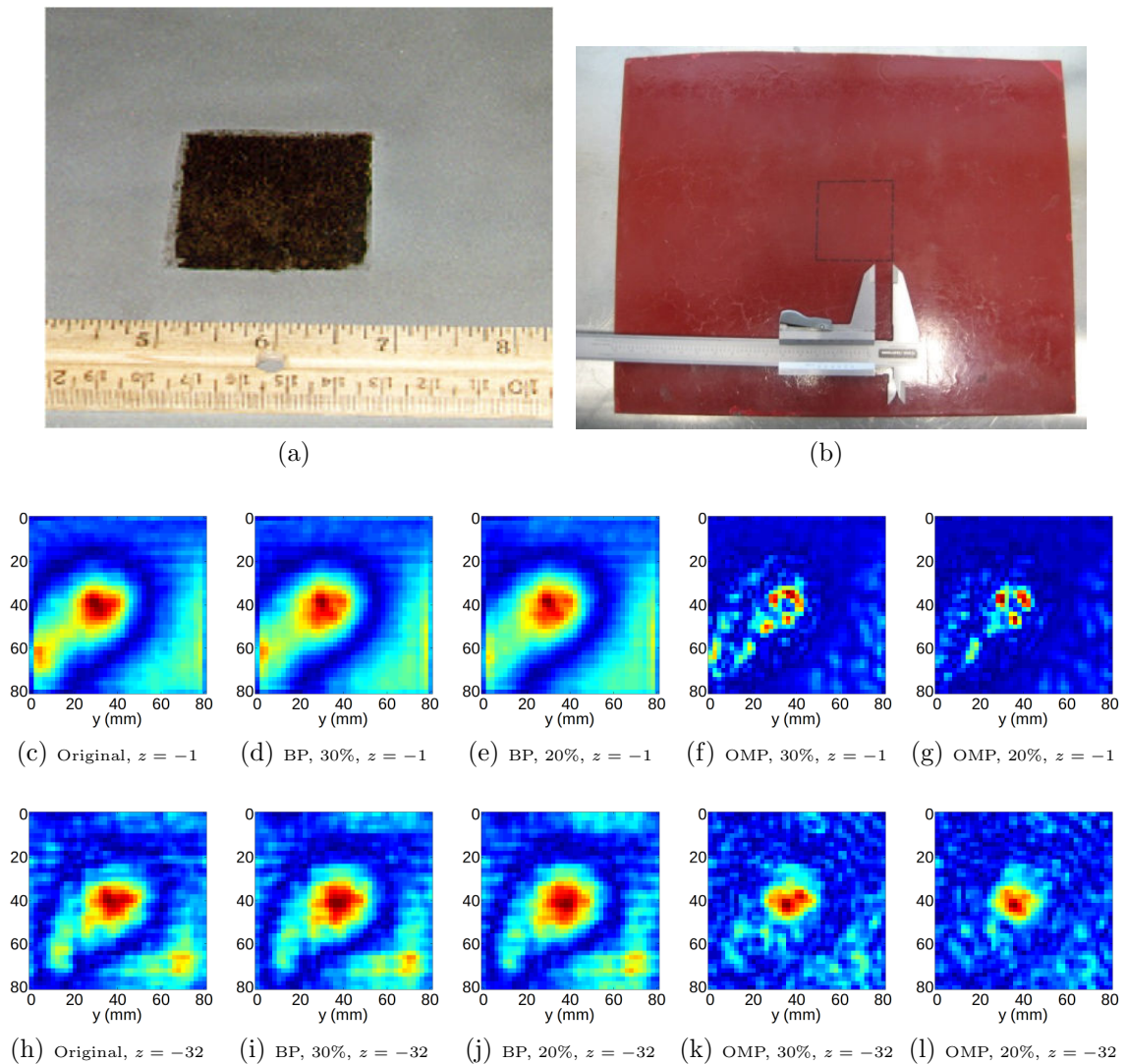


Figure 9: Corrosion under paint experiment (sample 2) (a) photo of the sample before paint, (b) photo of the specimen after paint, (c)-(g) 2D SAR images for probe standoff distance of 1 mm of full-set data, 30%, and 20% random points reconstructed by BP and OMP (CFDR), (h)-(l) 2D SAR images for probe standoff distance of 32 mm of full-set data, 30%, and 20% random points reconstructed by BP and OMP (CFDR). Figure 9a is reproduced from: Research in Nondestructive Evaluation, Vol. 9, No. 4, 1997, pp. 201-212, copyright American Society for Nondestructive Testing, 1997.

6. CONCLUSION

The results of experimental tests show that compressed sensing can be successfully applied to 2D and 3D microwave SAR imaging for nondestructive testing applications. Using the proposed methods, we can significantly reduce the acquisition time and keep the computational complexity of the post processing low while producing very similar images. Due to truncation errors occurring in each iteration of data recovery, the 3D SAR sparse representation failed to converge. In the future, we plan to address this issue by reducing the effect of truncation error to produce high-quality 3D images from undersampled measurements.

7. ACKNOWLEDGMENT

We wish to thank Dr. Sergey Kharkovsky and Dr. Mohammad T. Ghasr for their valuable assistance in setting up the measurement apparatus. We also thank Mr. Joseph T. Case and Mr. Mojtaba Fallahpour for their assistance in producing the SAR images and making measurements. This work is partially supported by an ASNT Graduate Fellowship award and by the University of Missouri Research Board fund.

II. COMPRESSED SENSING FOR SAR-BASED WIDEBAND 3D MICROWAVE IMAGING SYSTEM USING NONUNIFORM FFT

Hamed Kajbaf, Joseph T. Case, Zengli Yang, and Yahong Rosa Zheng

ABSTRACT—A new compressed sensing (CS) image reconstruction method is proposed for high-resolution wideband 3D synthetic aperture radar (SAR) imaging systems. In contrast to existing CS SAR methods that employ only a forward SAR transform in pre- or post-processing, the proposed method employs both forward SAR and reverse SAR (R-SAR) transforms in each CS iteration to improve the quality of reconstructed images. The truncation error, along with the SAR and R-SAR transform error, is identified as a critical obstacle to the convergence of the CS iterative algorithm and the quality of the reconstructed images. This paper proposes a simple and elegant truncation repair method to combat the truncation error and utilizes the nonuniform fast Fourier transform (NUFFT) to reduce the SAR and R-SAR transform errors. The proposed CS SAR method is applied to microwave and millimeter wave imaging systems for nondestructive evaluation of materials embedded in stratified media. Three different specimens under test (SUTs) are randomly under-sampled with 20% or 30% spatial points to show the efficacy of the proposed method. The results of the CS reconstructed images show that the proposed method improves the quality of the final SAR images and reduces the background artifacts in comparison with the images reconstructed from the original fully sampled measurements.

1. INTRODUCTION

Wideband 3D synthetic aperture radar (SAR) imaging systems have been successfully developed for nondestructive evaluation (NDE) of materials and structures

[1, 5]. These systems employ wideband microwave or millimeter waves to raster scan targets that are placed in air (free-space) or embedded in a dielectric medium. Then, the wideband complex reflection coefficients are measured by the same antenna probe and high-resolution volumetric images are reconstructed from the measurements via the SAR transform. With a frequency bandwidth of several tens of GHz and the step size of raster scanner on the order of a millimeter, the 3D imaging systems can achieve resolution on the order of a millimeter and enable detection and quantification of small flaws or targets in a specimen under test (SUT). Therefore, the wideband 3D imaging systems have found important applications to nondestructive testing and evaluation of industrial materials.

Unfortunately, high spatial resolution requires a small step size of the raster scanner and thus the data acquisition time can be relatively long for large SUTs. For example, a SUT of size $120 \text{ mm} \times 180 \text{ mm}$ requires data acquisition time of about 50 minutes if uniform spacing is used with step a size of 2 mm. Therefore, it is of practical interest to reduce the number of required spatial samples and consequently reduce the acquisition time.

Recently, compressed sensing (CS) has been used to reduce the sampling rate below the Nyquist rate while guaranteeing perfect recovery from sub-Nyquist measurements if the required conditions are satisfied [14, 16, 18]. Compressed sensing techniques have been successfully applied to Magnetic Resonance Imaging (MRI) and radar systems by using ℓ_1 norm optimization algorithms for image reconstruction. Specifically for 3D SAR-based radar imaging systems, several approaches have been proposed in the literature. In [31], the ω - k algorithm with Stolt interpolation is used first to convert the raw measurement into images as a preprocessing step. Then, an iterative recovery algorithm is applied to the incomplete SAR images to reconstruct the full images. This method benefits from the low complexity of Stolt interpolation and reduces the overall complexity of the algorithm. On the other hand, [32] uses the

forward SAR and reverse SAR (R-SAR) transforms in each iteration of the CS recovery algorithm along with total variation (TV) penalty. The ω - k algorithm with Stolt interpolation is employed in both SAR and R-SAR to enforce the convergence of the CS iterative algorithm by exploiting TV penalty. In [22], CS is applied to incomplete measurements without SAR transform to yield an estimate of the full measurement domain data first. Then, the ω - k algorithm using nonuniform fast Fourier transform (NUFFT) is used as postprocessing to transform the recovered measurement domain data to 3D SAR images. In all the three methods, the CS algorithm uses sparse representation of measurements or images in a well-known orthogonal basis such as discrete Fourier transform (DFT), discrete cosine transform (DCT), etc. While these methods have been shown to recover images with good quality, artifacts are often seen in the CS recovered images in comparison with those created from full-set measurements.

In this paper, we propose a new 3D CS imaging reconstruction method that utilizes the accurate NUFFT and inverse NUFFT algorithms in both reverse SAR (R-SAR) and forward SAR in each CS iteration. Although the NUFFT-based SAR algorithms have been shown to achieve higher accuracy with slightly higher computational complexity than the Stolt interpolation [8–10, 33], we discover that utilizing both NUFFT and inverse NUFFT in each CS iteration results in significant errors due to an inherent truncation window applied in the inverse NUFFT of the forward SAR. If not compensated, the error is accumulated via NUFFT in the reverse SAR in each iteration of the CS, and it results in non-convergence of the CS algorithm for reconstruction of high resolution volumetric images. Therefore, we propose a new truncation repair algorithm that deconvolves the windowing effect in the R-SAR, thus drastically reducing the truncation error. The proposed CS algorithm can enhance the quality of recovered images by reducing artifacts without using TV penalty, so that weak, small targets can also be well preserved.

The proposed CS image reconstruction algorithm is also capable of recovering SAR images from incomplete measurements for targets in stratified media that have different propagation velocities ($\bar{\nu}$ and ν). A forward-reverse referencing scheme is proposed to convert the incomplete measurement data and R-SAR transformed data to the second medium where the targets reside. The referencing scheme is applied in combination with the proposed CS image reconstruction algorithms. Several experimental tests are conducted for three different SUTs to demonstrate the efficacy of the proposed method. The first specimen consists of nine small rubber pads embedded in layers of construction foam. The second specimen consists of small rubber pads embedded in dry sand at different heights, which is an example of a stratified structure. The third specimen consists of steel rebar in cement-based mortar laid parallel to the measurement plane, which is a stratified structure similar to the second specimen but with embedded targets not sparse in the image domain. The raster scanner randomly samples 20% or 30% spatial points with uniform-spaced frequency points. The under-sampled measured data are reconstructed into 3D images using the proposed method. It is worth noting that randomly undersampled frequency points may also be used in the measurements. However, reduction in the number of frequency points affects acquisition time very little. Therefore, we choose uniform sampling in the frequency domain. The results of the experiments show that the proposed algorithm is capable of recovering high quality images from incomplete measurements.

2. CS ALGORITHMS FOR 3D SAR

Consider a wideband 3D SAR imaging system inspecting an SUT in an XYZ-Cartesian space, as shown in Fig. 1, where a stratified medium is assumed, that consists of two layers with relative permittivity of $\bar{\epsilon}_r$ and ϵ_r , respectively. In our experiments, the second layer of the medium is backed by free-space. For full-set

measurements and without CS, the microwave probe, mounted on a raster scanner, stops at all points on a uniform grid of (x_f, y_f) and performs stepped frequency reflection coefficient measurements with angular frequencies ω_i uniformly spaced in $[\omega_{\min}, \omega_{\max}]$ with step size of $\Delta\omega$. Meanwhile, the reflection from the SUT is measured by the probe and the received complex measurements (*i.e.* magnitude and phase) are denoted $f(x, y, \omega)$ with (x, y, ω) taken from the set $\mathcal{S}_f = \{(x_q, y_q, \omega_q)\}_{q=1}^{N_f}$, where N_f is the number of uniformly spaced measurements. To reconstruct the image from the full-set measurements, a phase adjustment operator \mathcal{I} is used to convert the measurement to the $\omega - k$ space corresponding to the surface of the second layer of the stratified medium as

$$F(k_x, k_y, \omega) = \mathcal{I}[f(x, y, \omega)] = \mathcal{F}_{2D} \{f(x, y, \omega)\} \exp \left[-jz_0 \sqrt{(2\omega/\bar{v})^2 - k_x^2 - k_y^2} \right] \quad (1)$$

where (k_x, k_y, ω) is also in the set $\{(k_{x,q}, k_{y,q}, \omega_q)\}_{q=1}^{N_f}$, $\mathcal{F}_{2D}\{\cdot\}$ is the two dimensional discrete Fourier transform (DFT), $\bar{v} = c/\sqrt{\bar{\epsilon}_r}$ is the wave propagation speed in the first layer with c being the propagation speed of light in free-space, and k_x - k_y (and k_z) are the frequency components in the X-Y (and Z) dimensions, respectively.

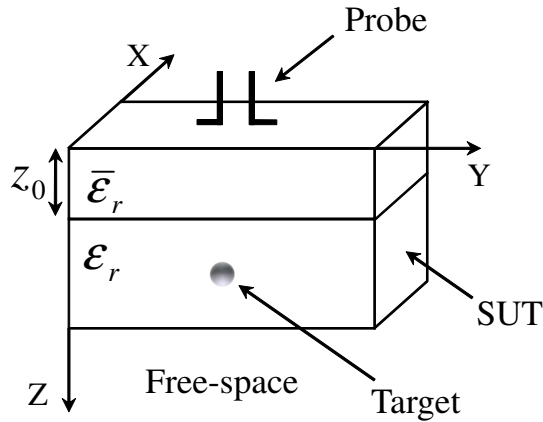


Figure 1: The schematic of a SAR-based microwave imaging system.

Then, a forward SAR transform computes the high-resolution, uniformly-spaced volumetric image $s(x, y, z)$ from $F(k_x, k_y, \omega)$ by the NUFFT-based SAR algorithm [8–10]

$$s(x, y, z) = \mathcal{F}_{2D}^{-1} \left\{ \mathcal{F}_{NU}^{-1} \{ F(k_x, k_y, \omega) \} \right\} \quad (2)$$

where $\mathcal{F}_{2D}^{-1}\{\cdot\}$ is the two dimensional inverse DFT, and $\mathcal{F}_{NU}^{-1}\{\cdot\}$ is the one dimensional inverse NUFFT along k_z . The image $s(x, y, z)$ in (2) is defined on the set of N_s uniformly sampled locations $(x, y, z) \in \{(x_r, y_r, z_r)\}_{r=1}^{N_s}$ and is vectorized as \mathbf{s} , where N_s is the number of SAR image voxels. The forward SAR transform is formulated in matrix form as

$$\mathbf{s} = \mathbf{\Omega} \mathbf{f} \quad (3)$$

where $\mathbf{f} \in \mathbb{C}^{N_f}$ is the vectorized measurement $f(x, y, \omega)$, and $\mathbf{\Omega} \in \mathbb{C}^{N_s \times N_f}$ is the forward SAR transform matrix for the stratified medium combining the operators \mathcal{I} , $\mathcal{F}_{2D}^{-1}\{\cdot\}$, and $\mathcal{F}_{NU}^{-1}\{\cdot\}$. The approximate matrix formulation of $\mathbf{\Omega}$ is detailed in the Appendix. Note that the XY-coordinates (x_s, y_s) in the image space may be selected consistently with (x_f, y_f) in the measurement space and the SAR transform may also be implemented by other $\omega - k$ algorithms such as the Stolt transform [11–13].

To apply CS to the 3D imaging system, the probe stops at undersampled random points on the XY-plane and the measured signal vector becomes $\mathbf{y} = \mathbf{\Phi} \mathbf{f}$, where $\mathbf{\Phi}$ is an $N_y \times N_f$ linear undersampling measurement matrix with $N_y < N_f$. Each row of $\mathbf{\Phi}$ contains all zeros but only one element with value one. N_y is the number of undersampled measurements \mathbf{y} . The ones in $\mathbf{\Phi}$ are uniformly distributed along the columns corresponding to the selected random probing points on the XY-plane. For each selected probing point, we use all equi-spaced angular frequencies because the vector network analyzer used in the imaging system sweeps the frequency very fast

and reducing frequency points does not save acquisition time. An optimal path may be designed for the raster scanner with the Traveling Salesman Algorithm (TSA) and an example path with 5% randomly selected points is shown in Fig. 2, where the lines show the path of the probe and the dots are the selected random sampling points in the XY plane. Figures 2a and 2b show the optimal path and nonuniform raster scan for a 120×180 scan area. Our experiments show that by random undersampling and using the optimum scanning method, we can reduce the acquisition time from 50 minutes for full-set measurement to 17 minutes for a typical random sampling of 20% of spatial points.

To reconstruct the image \mathbf{s} from the undersampled measurement signal \mathbf{y} , we use the ℓ_1 norm CS approach

$$\min_{\mathbf{s} \in \mathbb{C}^{N_s}} \|\Psi \mathbf{s}\|_1 \quad \text{subject to} \quad \mathbf{y} = \Phi \Omega^{-1} \mathbf{s} \quad (4)$$

where $\|\cdot\|_1$ denotes ℓ_1 norm, Ψ is the sparsifying transform and N_s is the number of voxels in the 3D image \mathbf{s} .

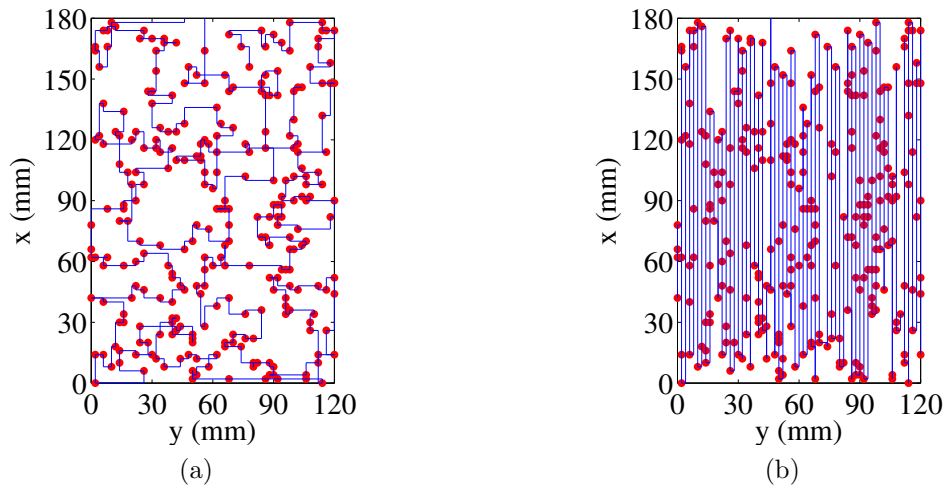


Figure 2: Optimal path vs. raster scanning path for 5% random undersampling.

Adding a total variation (TV) penalty, (4) can be solved by minimizing the cost function

$$\mathcal{J}(\mathbf{s}) = \lambda_\ell \|\Psi\mathbf{s}\|_1 + \lambda_t \text{TV}(\mathbf{s}) + \|\mathbf{y} - \Phi\Omega^{-1}\mathbf{s}\|_2^2 \quad (5)$$

where $\|\cdot\|_2$ denotes ℓ_2 norm and the λ_ℓ and λ_t are weighting factors to determine the penalty on the ℓ_1 norm and TV, respectively. The operator Ω^{-1} is a matrix representation of the reverse SAR (R-SAR) transform and is a pseudo-inverse of matrix Ω . However, for implementation, we use the accurate SAR and R-SAR transforms that will be detailed in Sec. 3.

Many algorithms can be used to minimize (5) iteratively, for example, the majorization-minimization algorithm [34], alternative direction method (ADM) [35], and nonlinear conjugate gradient descent (CGD) algorithm [36]. In this work, we use the CGD with backtracking line search. The algorithm is listed in Algorithm 1, where $\text{Re}\{\cdot\}$ is the real part of a complex variable, $\Delta\mathbf{s}_i$ is the change of \mathbf{s}_i at the i -th iteration, and $\nabla\mathcal{J}$ is the derivative of \mathcal{J} with respect to \mathbf{s} and is calculated as

$$\nabla\mathcal{J}(\mathbf{s}) = \lambda_\ell \nabla \|\Psi\mathbf{s}\|_1 + \lambda_t \nabla \text{TV}(\mathbf{s}) + 2\Omega\Phi^H(\Phi\Omega^{-1}\mathbf{s} - \mathbf{y}). \quad (6)$$

In (6), the TV penalty and the gradient of the penalty are calculated as in [37]. Also, since the absolute value function in ℓ_1 norm is not differentiable, the approximation $|s_r| \approx \sqrt{s_r^H s_r + \zeta}$ is used, where ζ is a positive smoothing parameter. Therefore, $\frac{d}{ds_r} \approx \frac{s_r}{\sqrt{s_r^H s_r + \zeta}}$.

As it can be seen from Algorithm 1, the conjugate gradient requires the computation of the forward SAR transform Ω and reverse SAR transform Ω^{-1} in each iteration at line 9. However, the original NUFFT and inverse NUFFT introduce truncation errors that accumulate quickly after several iterations and cause the CS algorithm to never reach the convergence condition of $\|\nabla\mathcal{J}_i\| < \rho$. For this rea-

son, we propose an accurate R-SAR transform in Section 3 that utilizes a technique called “truncation repair” to reduce the truncation error; thereby preventing error accumulation and ensuring the convergence of the CS algorithm.

Algorithm 1 CGD with backtracking line search

% Parameters:

β and ζ – line search parameters

ρ – stopping parameter by gradient magnitude

% Reconstruction Algorithm

1: $\mathbf{s}_0 := \mathbf{\Omega}\Phi^H \mathbf{y}$, $\nabla \mathcal{J}_0 := \nabla \mathcal{J}(\mathbf{s}_0)$, $\Delta \mathbf{s}_0 := -\nabla \mathcal{J}_0$

2: $i := 0$

3: **repeat**

4: $t := 1$

5: **repeat**

6: $t := \beta t$

7: **until** $\mathcal{J}(\mathbf{s}_i + t\Delta \mathbf{s}_i) < \mathcal{J}(\mathbf{s}_i) + \zeta t \text{Re}\{(\nabla \mathcal{J}_i)^H \Delta \mathbf{s}_i\}$

8: $\mathbf{s}_{i+1} := \mathbf{s}_i + t\Delta \mathbf{s}_i$

9: $\nabla \mathcal{J}_{i+1} := \nabla \mathcal{J}(\mathbf{s}_{i+1})$

10: $\Delta \mathbf{s}_{i+1} := -\nabla \mathcal{J}_{i+1} + \frac{\|\nabla \mathcal{J}_{i+1}\|^2}{\|\nabla \mathcal{J}_i\|^2} \Delta \mathbf{s}_i$

11: $i := i + 1$

12: **until** $\|\nabla \mathcal{J}_i\| < \rho$

3. ACCURATE SAR AND R-SAR TRANSFORMS

In this section, we first illustrate the truncation errors introduced by the NUFFT of the forward SAR transform and then propose a new truncation repair scheme for the R-SAR transform to achieve the accuracy required for the iterative CS reconstruction Algorithm 1.

For the forward SAR transform, we modify the standard NUFFT algorithm [8–10] to include stratified media, with details shown on the left side of Fig. 3, where the exponential term in (1) is referred to as “Reference Forward” and the phase adjustment operator (\mathcal{I}) is followed by a conversion from $F(k_x, k_y, \omega)$ to k -space data $F(k_x, k_y, k_z)$. For each pair of (k_x, k_y) , k_z is drawn from the nonuniformly spaced set $\{k_{z,i}\}_{i=1}^{N_\omega}$ with

$$k_{z,i} = \sqrt{\left(\frac{2\omega_i}{\nu}\right)^2 - k_x^2 - k_y^2} \quad (7)$$

where ν is the propagation speed in the second layer that has a dielectric constant ε_r , and $\nu = c/\sqrt{\varepsilon_r}$.

The next step of the SAR algorithm is the inverse NUFFT algorithm that transforms the $F(k_x, k_y, k_z)$ data nonuniformly spaced in k_z into

$$S(k_x, k_y, z) = \mathcal{F}_{\text{NU}}^{-1}\{F(k_x, k_y, k_z)\} \quad (8)$$

with z sampled at $(2N_z + 1)$ uniformly spaced locations $\{z_n\}_{n=-N_z}^{N_z}$. Since the wide-band 3D imaging system uses a frequency band of $[\omega_{\min}, \omega_{\max}]$ with step size $\Delta\omega$, the number of frequency points is N_ω and the resolution in z is determined by

$$\delta_z = \frac{\nu\pi}{\omega_{\max} - \omega_{\min}}. \quad (9)$$

We assume that the uniform step size of z_n for the inverse NUFFT satisfies $\Delta z \leq \delta_z$.

Note that the inverse NUFFT is a fast and accurate approximation to the inverse nonuniform discrete Fourier transform (NDFT) [23, 38]

$$F(k_x, k_y, k_z) \xleftrightarrow{\mathcal{F}_{\text{NDFT}}} S(k_x, k_y, z) = \sum_{\iota=1}^{N_\omega} F(k_x, k_y, k_{z,\iota}) e^{jz k_{z,\iota}} \quad (10)$$

where $k_{z,\iota}$'s are nonuniformly spaced. While the computational complexity of the inverse NDFT is $\mathcal{O}(N_z N_\omega)$, the complexity of the inverse NUFFT is

$$\mathcal{O}(\sigma(2N_z + 1) \log(\sigma(2N_z + 1)) + (2p + 1)N_\omega)$$

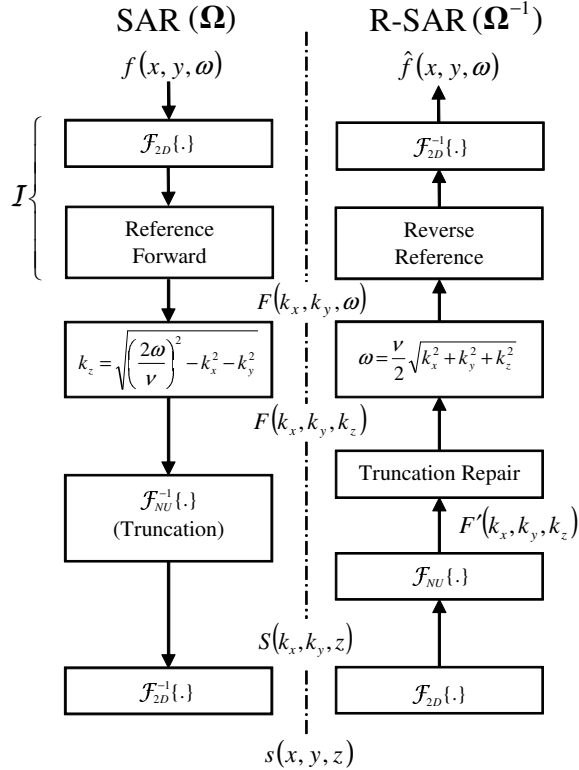


Figure 3: The block diagram of SAR and R-SAR using NUFFT for the proposed algorithm.

where σ is the oversampling factor for the Gaussian kernel in the calculation of the inverse NUFFT and p is the overlapping factor. The Gaussian kernel is defined as

$$G(k_z) = (\pi b)^{-1/2} e^{-\frac{(\sigma(2N_z+1)k_z)^2}{b}} \quad (11)$$

where $b = \frac{2\sigma p}{\pi(2\sigma-1)}$. Let us define

$$H(k_z) = F(k_z) * G(k_z) \quad (12)$$

and its discrete Fourier transform of $h(z_n)$ where $*$ denotes convolution. Then, the values of $S(z_n)$ can be approximated by the NUFFT as

$$S(z_n) = \frac{h(z_n)}{\sigma(2N_z + 1)g(z_n)} \quad (13)$$

where $g(z_n)$ is the inverse discrete Fourier transform of $G(k_z)$ [23].

However, by using NUFFT, a truncation in z occurs since computing an unbounded image in the Z domain is practically infeasible. Thus, the inverse NUFFT should maximally be computed in the range $-Z_{\max} \leq z_n \leq Z_{\max}$, where Z_{\max} is the maximum unambiguous range for the propagating wave along the Z axis from the measurement plane, and it is defined as

$$Z_{\max} = \frac{\nu\pi}{2\Delta\omega} \quad (14)$$

The truncation in z can result in significant error in the estimate of the spectrum from the NUFFT of the reverse SAR transform. Truncation repair has to be inserted between the NUFFT and coordinate mapping of $\omega_i = \frac{\nu}{2}\sqrt{k_x^2 + k_y^2 + k_{z,i}^2}$, as shown on the right side of Fig. 3, where $F'(k_x, k_y, k_z)$ and $F(k_x, k_y, k_z)$ are the k -space data

before and after the truncation repair, respectively. Since truncation error occurs only for the z and k_z dimensions, we simplify the nomenclature from $S(k_x, k_y, z)$ defined in (8) to $S(z_n)$ for truncated z_n and $S_\infty(z_n)$ for $-\infty < z_n < +\infty$. Similarly, we also reduce $F(k_x, k_y, k_z)$ to $F(k_z)$ and $F'(k_x, k_y, k_z)$ to $F'(k_z)$. The truncated $S(z_n)$ can be represented in terms of $S_\infty(z_n)$ as

$$S(z_n) = m(z_n)S_\infty(z_n) \quad (15)$$

where the mask function is defined as

$$m(z_n) = \begin{cases} 1, & -Z_{\max} \leq z_n \leq Z_{\max} \\ 0, & \text{otherwise.} \end{cases} \quad (16)$$

Furthermore, $F(k_z)$ and $F'(k_z)$ are related with $S_\infty(z_n)$ and $S(z_n)$, respectively, as the discrete-time Fourier transform (DTFT) pairs

$$S_\infty(z_n) \xleftrightarrow{\mathcal{F}_{\text{DTFT}}} F(k_z) \quad (17)$$

$$S(z_n) \xleftrightarrow{\mathcal{F}_{\text{DTFT}}} F'(k_z). \quad (18)$$

Also, let $m(z_n) \xleftrightarrow{\mathcal{F}_{\text{DTFT}}} M(k_z)$. Then we have [39]

$$\begin{aligned} M(k_z) &= \sum_{z_n=-\infty}^{\infty} m(z_n)e^{-jz_n k_z} \\ &= \frac{\sin(\Delta z k_z (2N_z + 1)/2)}{\sin(\Delta z k_z / 2)} \end{aligned} \quad (19)$$

and

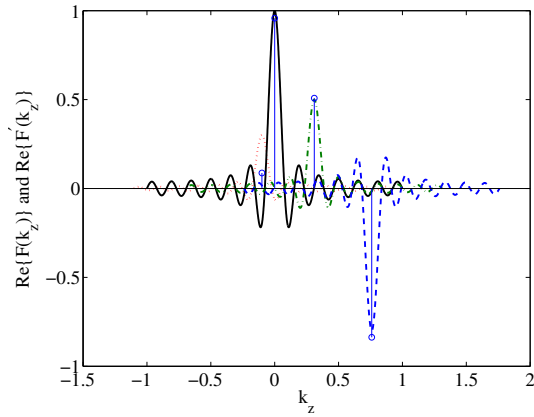
$$F'(k_z) = M(k_z) * F(k_z). \quad (20)$$

The difference between $F(k_z)$ and $F'(k_z)$ is the truncation error due to nonuniform k_z sampling and truncation in z . The truncation error is illustrated in Fig. 4, where four nonuniform points $k_{z,i}$ are selected as $\{k_{z,i}\}_{i=1}^4 = [-0.1/\pi, 0, 0.1\pi, 0.76/\pi]$, and the corresponding $\{F(k_{z,i})\}_{i=1}^4 = [0.3 - 0.3j, 1 - 0.8j, 0.5 + 0.75j, -0.8 + j]$. Since the main lobe width of $M(k_z)$ is 0.05π , it is clear that the main lobes of $F(k_{z,1})M(k_z - k_{z,1})$ and $F(k_{z,2})M(k_z - k_{z,2})$ overlap and a significant error is introduced into $F'(k_{z,1})$ due to $F(k_{z,2})M(k_z - k_{z,2})$ because $F'(k_{z,1}) = \sum_{i=1}^4 F(k_{z,i})M(k_z - k_{z,i})$. Meanwhile, $F(k_{z,3})M(k_z - k_{z,3})$ and $F(k_{z,4})M(k_z - k_{z,4})$ contribute small errors to $F'(k_{z,1})$ because the sampling points $k_{z,3}$ and $k_{z,4}$ are far apart from $k_{z,1}$. The resulting $F'(k_z)$ values are shown in stems in Figs. 4a and 4b for the real and imaginary parts, respectively. It is also interesting to note that $F(k_{z,2})$ and $F(k_{z,3})$ introduce no errors to each other because their sampling points are spaced at precisely twice the main lobe width. If k_z is uniformly spaced in integer multiples of the main lobe width, then truncation in z will yield no errors between $F(k_z)$ and $F'(k_z)$. Figure 4c illustrates $F(k_z)$ and $F'(k_z)$ in vector form for the nonuniformly spaced k_z and the difference between the corresponding vectors are clearly shown in terms of magnitude and phase.

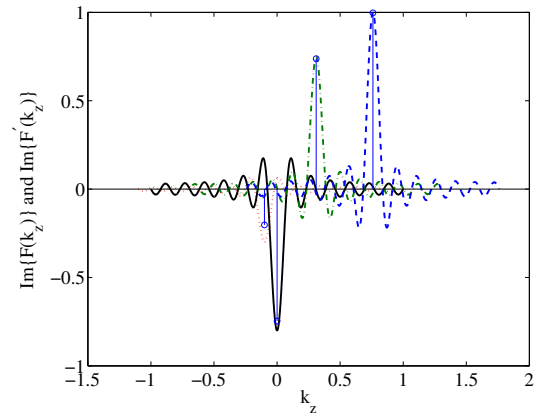
The truncation error may be reduced by several error minimization methods [23, 40]. However, the computational complexity of these methods is unnecessarily high and we propose a simple and direct deconvolution method for recovering $F(k_z)$ from $F'(k_z)$. To deconvolve the effect of truncation efficiently, let us formulate the convolution in (20) in matrix form

$$\mathbf{F}' = \mathbf{M}\mathbf{F} \quad (21)$$

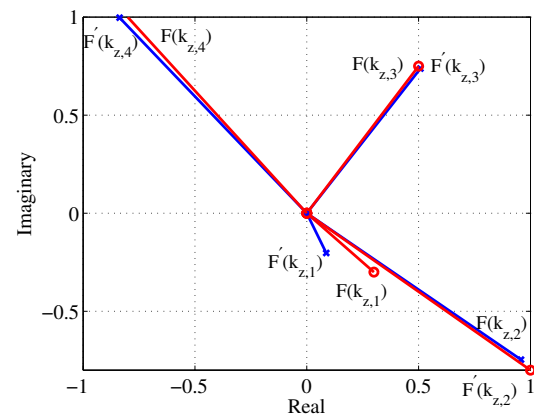
where \mathbf{F} and \mathbf{F}' are the vectorized $F(k_z)$ and $F'(k_z)$ sampled at nonuniform locations of $\{k_{z,i}\}_{i=1}^{N_w}$, as calculated in (7), and \mathbf{M} is the $N_w \times N_w$ convolution matrix with its



(a) Real part



(b) Imaginary part



(c) Vector plot

Figure 4: Truncation error in SAR and R-SAR with NUFFT (a) real part, (b) imaginary part, and (c) vector plot of $F(k_z)$ and $F'(k_z)$.

element at row r and column c being

$$M_{r,c} = M(k_{z,r} - k_{z,c}). \quad (22)$$

It should be noted that for some pairs of (k_x, k_y) , the k_z values become complex and are invalid as it can be seen from (7). The inverse NUFFT along k_z is calculated only for valid k_z 's and the dimension of \mathbf{M} is smaller than $N_w \times N_w$ for the pairs of (k_x, k_y) corresponding to invalid k_z 's. Figure 5 shows the nonuniform mapping of k_z where k_y is set to zero and k_x and ω are uniformly spaced. The invalid k_z 's are the ones corresponding to the area inside the inner circle and outside the outer circle.

If \mathbf{M} is invertible, the original signal \mathbf{F} can be recovered exactly by deconvolving the spectrum representation of the mask function by matrix inversion

$$\mathbf{F} = \mathbf{M}^{-1}\mathbf{F}'. \quad (23)$$

To ensure that \mathbf{M} is invertible, the following three requirements must be met.

1. *Frequencies of Measurement Must be Known* – The frequencies ω used in the measurement $f(x, y, \omega)$ must be known so that the contributions of these frequencies in the SAR image $s(x, y, z)$ can be determined. This is in contrast to the more general problem for which the frequencies of the system may be unknown. In short, the SAR imaging system must be well defined so that SAR and R-SAR form an accurate pair.
2. *Support Functions Cannot Overlap* – The main lobes of the function $M(k_z)$ in (19) as referred to by M_{rc} in (22) must not overlap. Given that k_z is determined by (7), the minimum spacing in k_z varies for each pair of (k_x, k_y) , as shown in Fig. 5. When $k_x > 0$, the spacing of k_z increases as ω decreases. The minimum spacing for a given (k_x, k_y) pair, denoted $\Delta k_{z,i}$, increases as k_x or k_y increases.

$\min_i(\Delta k_{z,i})$ occurs at $k_x = k_y = 0$ and we have $\min_i(\Delta k_{z,i}) = \frac{2\Delta\omega}{\nu}$. Given that

$$Z_{\max} - Z_{\min} \approx \Delta z(2N_z + 1), \quad (24)$$

it can be shown that the following condition guarantees that the main lobe of $M(k_z)$ for all pairs of (k_x, k_y) do not overlap

$$Z_{\max} - Z_{\min} \geq \frac{\nu\pi}{\Delta\omega} = 2Z_{\max}. \quad (25)$$

3. *Sampling of SAR Image Along z Must Satisfy the Nyquist Rate* – The uniform discrete image sampling increment Δz must be less than or equal to half that of the range resolution to satisfy the Nyquist rate

$$\Delta z \leq \frac{\delta_z}{2} = \frac{\nu\pi}{2(\omega_{\max} - \omega_{\min})} \quad (26)$$

This requirement prevents the aliasing error in the NUFFT for the R-SAR transform.

It is worth noting that \mathbf{M}^{-1} may be calculated and stored for all combinations of (k_x, k_y, ω) beforehand and used for all subsequent iterations of CS image reconstruction. Since the number of frequencies N_ω is usually much smaller than the number of spatial samples $(2N_z + 1)$ in z , the truncation repair in the R-SAR transform can be performed accurately without significant increase in computational complexity.

Denoting $\mathcal{T}\{\cdot\}$ as the truncation repair in (23), we have

$$F(k_x, k_y, k_z) = \mathcal{T}\{\mathcal{F}_{\text{NU}}\{S(k_x, k_y, z)\}\}. \quad (27)$$

With truncation repair, the accurate NUFFT-based SAR/R-SAR pair can be used in the CS iterations repeatedly with negligible cumulative error and lead to convergence

of the CGD algorithm at very stringent conditions such as $\rho = 10^{-5}$. However, if the truncation error is ignored in the R-SAR transform, the CGD iterative algorithm will fail to converge due to the cumulative error, as demonstrated in Fig. 6, where the cumulative normalized root mean square (NRMS) error between the full-set measured data $f(x, y, \omega)$ and the estimate of measured data $\hat{f}(x, y, \omega)$ calculated from R-SAR transform (without undersampling) after iterations are computed for different values of NUFFT parameters,

$$\text{NRMS} = \frac{\|f(x, y, \omega) - \hat{f}(x, y, \omega)\|_2}{\|f(x, y, \omega)\|_2}. \quad (28)$$

The dB values of NRMS error without truncation repair increase almost linearly with the number of iterations and the CS algorithm fails to converge. When the truncation repair is applied, the oversampling factor σ and overlapping factor p , also play critical roles on keeping the NUFFT accuracy. The approximate slopes of the NRMS error curves after initial transition are compared in Table 1 for these NUFFT parameters,

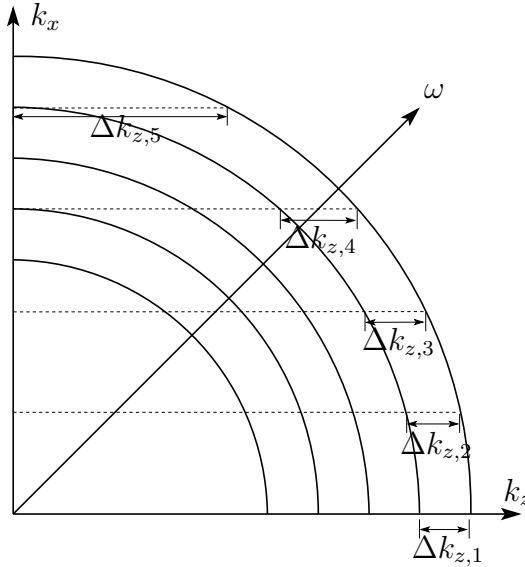


Figure 5: Illustration of nonuniform mapping of k_z with $k_y = 0$ and uniformly spaced k_x and ω .

where smaller NRMS slope indicates higher accuracy. The two cases with $\sigma = 2$, and $p = 6$ or $p = 12$ guarantee the convergence of the CS algorithm, but other cases do not meet the CS convergence requirements. In practice, the oversampling of $\sigma = 1$ is usually avoided due to its poor accuracy. For larger values of oversampling factor ($\sigma > 2$), we increase the accuracy unnecessarily with the cost of high computational complexity.

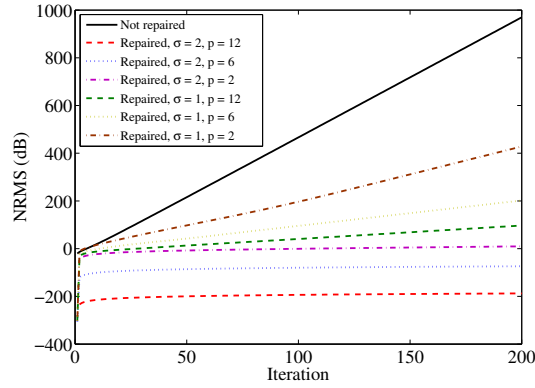


Figure 6: Accumulated errors in $f(x, y, \omega)$ after each SAR and R-SAR transform pair using NUFFT with and without truncation repair.

Table 1: Slope of NRMS error curves vs. iteration

σ	p	Slope (dB/iteration)	Converge for $\rho = 10^{-5}$
2	12	0.081	Yes
	6	0.081	Yes
	2	0.013	No
1	12	0.560	No
	6	1.066	No
	2	2.204	No

4. EXPERIMENTS AND RESULTS

Three sets of experiments were performed to verify the performance of the proposed method. In this section, we explain the experimental configurations and the results of applying CS for SAR imaging. For each experiment, we considered four recovery configurations of the CS method labeled Cases 1 through 4. Each case has its own CS parameters as shown in Table 2 where the notation EYE indicates the identity matrix and DCT is the 3D discrete cosine transform. Cases 1-3 used the proposed CS recovery model with different parameters and Case 4 used the recovery model proposed in [22] that does not utilize SAR in the CS iterations. In contrast to Cases 1-3 that minimize (5), Case 4 applies CS to the undersampled measurement vector \mathbf{y} without TV to recover an estimate of the full measurement space data \mathbf{f} first, then performs only one forward SAR transform to reconstruct the image. Figure 7 shows the iterations between the orthogonal basis and its inverse followed by an NUFFT-based SAR transform. Specifically, this approach solves the linear program

$$\min_{\mathbf{c} \in \mathbb{C}^{N_u}} \|\mathbf{c}\|_1 \quad \text{subject to} \quad \mathbf{y} = \Phi \Psi^H \mathbf{c} \quad (29)$$

where \mathbf{c} is the sparse representation of the measurement \mathbf{f} in the transform domain Ψ such that $\mathbf{c} = \Psi \mathbf{f}$, and N_u is the number of non-zero coefficients of \mathbf{c} . The image is then reconstructed by $\mathbf{s} = \Omega \Psi^H \mathbf{c}$.

4.1. RUBBER PADS IN FOAM - SPECIMEN 1

4.1.1. Experiment.

The first set of experiments was performed on a piece of foam with dimensions 120mm × 180mm × 80mm. The SUT consisted of three layers of construction foam taped together. On each layer of the foam, three round rubber pads of 5 mm diameter and 2 mm height were embedded at different locations as shown in

Fig. 8. The distance between the aperture and the surface of SUT (standoff distance) was 34 mm. The measurements were performed for discrete frequencies between 35.04 GHz and 44.96 GHz (Q-band). Since the distance between the measurement probe and the bottom layer of the SUT (Z_{\max}) was 114 mm, the maximum frequency step size was $\Delta\omega/(2\pi) = c/(4Z_{\max}) = 0.66$ GHz [13]. In our experiment, the measurements were performed with frequency steps of 0.56 GHz. The spatial steps should follow the $\lambda_{\min}/2 = 3.3$ mm rule for targets far from the aperture and $\lambda_{\min}/4 = 1.7$ mm for targets near the aperture where λ_{\min} was the smallest wavelength corresponding to the maximum frequency (ω_{\max}). Consequently, the spatial steps were chosen to be 2 mm along X and Y dimensions prior to undersampling. The complex reflection coefficients were measured and recorded by the vector network analyzer used in [7].

4.1.2. Results. Slices of 3D SAR images of the first specimen are shown in Fig. 9. The left column of the figure shows the SAR images from a full-set of

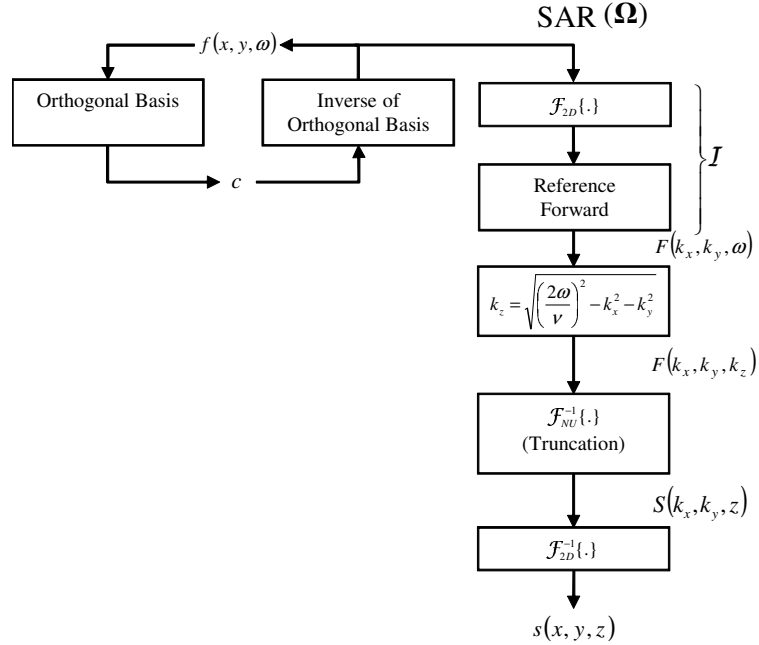


Figure 7: The block diagram of iterations for orthogonal basis as proposed in [22].

measurements for each height of interest ($z = 34, 66, \text{ and } 82$). The recovered images from 20% of measurements are shown for the proposed methods by minimizing (5) in columns 2-4. The details for each case are defined in Table 2. By reducing the measurement points to 20% of the full-set data, the average distance between the spatial points was approximately $2\lambda_{\min}/3 = 4.4 \text{ mm}$ and the acquisition time was

Table 2: CS model parameters for three sets of experiments

Experiment	Case	CS Model	λ_ℓ	λ_t	Ψ
Rubber in foam	1	Eq. (5)	2	0	EYE on s
	2	Eq. (5)	2	0.8	EYE on s
	3	Eq. (5)	2	0.8	DCT on s
	4	Eq. (29)	0.5	0	DCT on f
Rubber in sand	1	Eq. (5)	0.5	0	EYE on s
	2	Eq. (5)	0.5	0.3	EYE on s
	3	Eq. (5)	0.5	0.3	DCT on s
	4	Eq. (29)	0.5	0	DCT on f
Rebar in mortar	1	Eq. (5)	0.5	0	EYE on s
	2	Eq. (5)	0.5	0.5	EYE on s
	3	Eq. (5)	0.5	0.5	DCT on s
	4	Eq. (29)	0.5	0	DCT on f

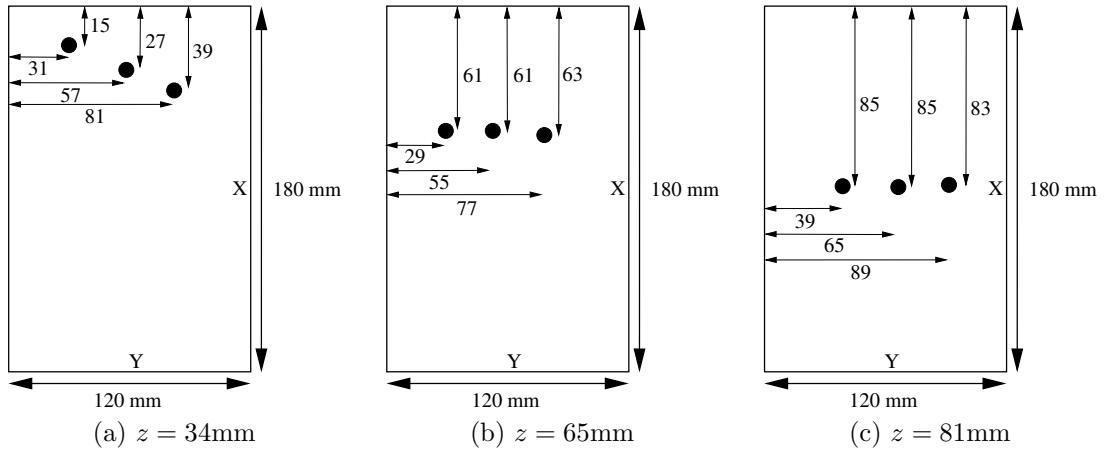


Figure 8: Schematic of the rubber pads in the scanned area of Specimen 1, where unit in figure is mm, and z is the distance from the probe (not to scale).

reduced from 50 minutes to 17 minutes. It can be seen that Cases 1-3 have noticeably reduced the level of background artifacts. Case 4 on the other hand has increased the level of background artifacts. Case 2 has the best performance in terms of artifact removal as it benefits from both 3D SAR sparse representation and TV penalty while Case 3 has best maintained the shape of the targets during the recovery process which might be of interest for certain nondestructive evaluation applications.

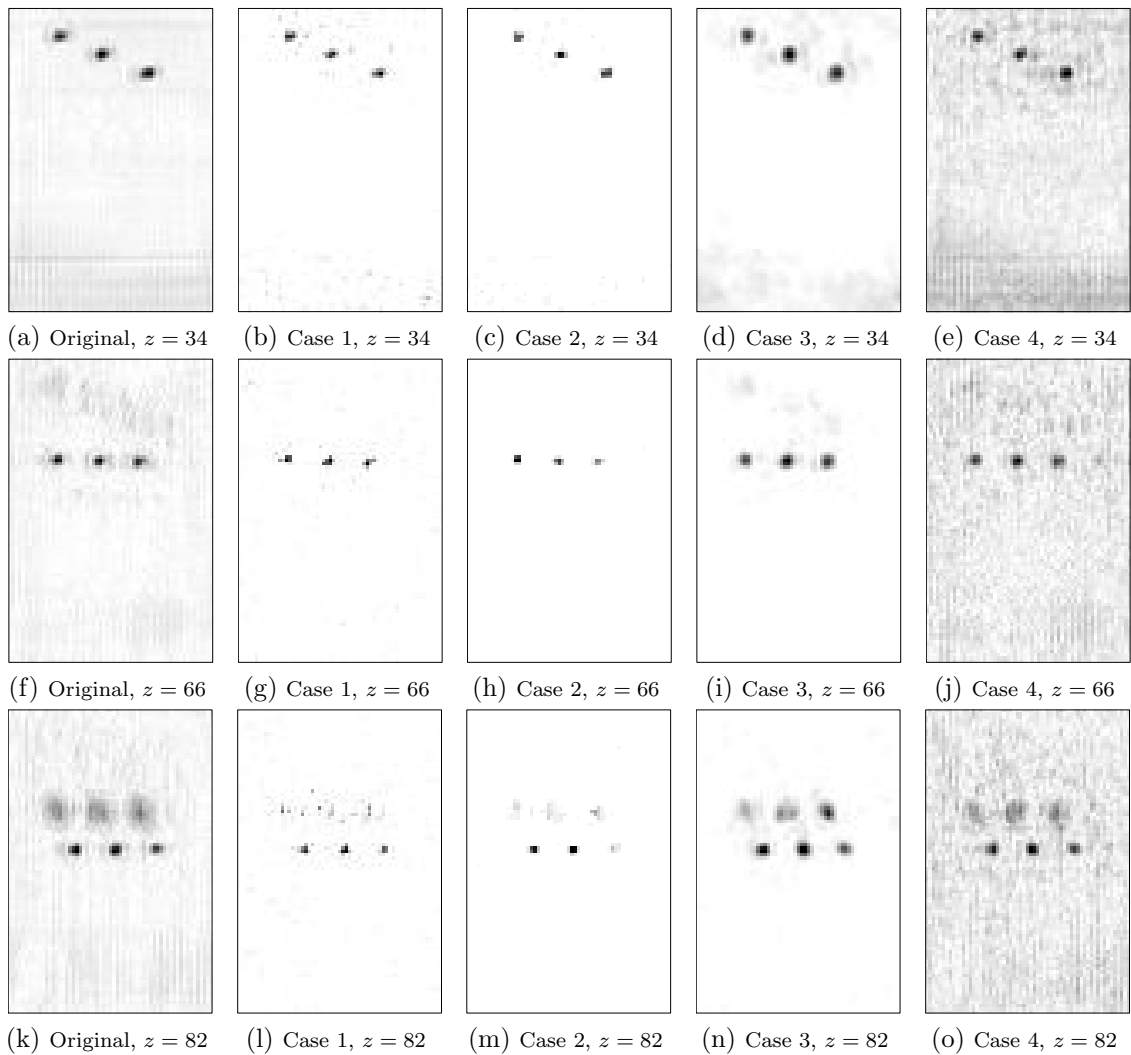


Figure 9: Slices of 3D SAR images of Specimen 1 from complete data and recovered data from 20% randomly selected points.

4.2. RUBBER PADS IN SAND - SPECIMEN 2

4.2.1. Experiment. The second set of experiments was performed on the SUT consisting of eight rubber pads embedded in dry sand at 5 different heights, as shown in Fig. 10. The rubber pads were of size $10 \times 10 \times 3 \text{ mm}^3$. The distance between the aperture and the surface of sand was 5 mm. The frequency range for this set of experiments was from 8.2 GHz to 12.4 GHz (X-band) with steps of 0.21 GHz. An area of $300 \times 300 \text{ mm}^2$ was scanned uniformly with steps of 3 mm along X and Y dimensions prior to undersampling. The reflection coefficients were measured and recorded by an HP8510C vector network analyzer.

4.2.2. Results. Figure 11 shows the results of the second set of experiments consisting of the images from the full-set measurements and the images recovered from 30% of the measurements. Sizing of the rubber pads is relatively the same for all cases. It can be seen that even images from the full-set of measurements have a

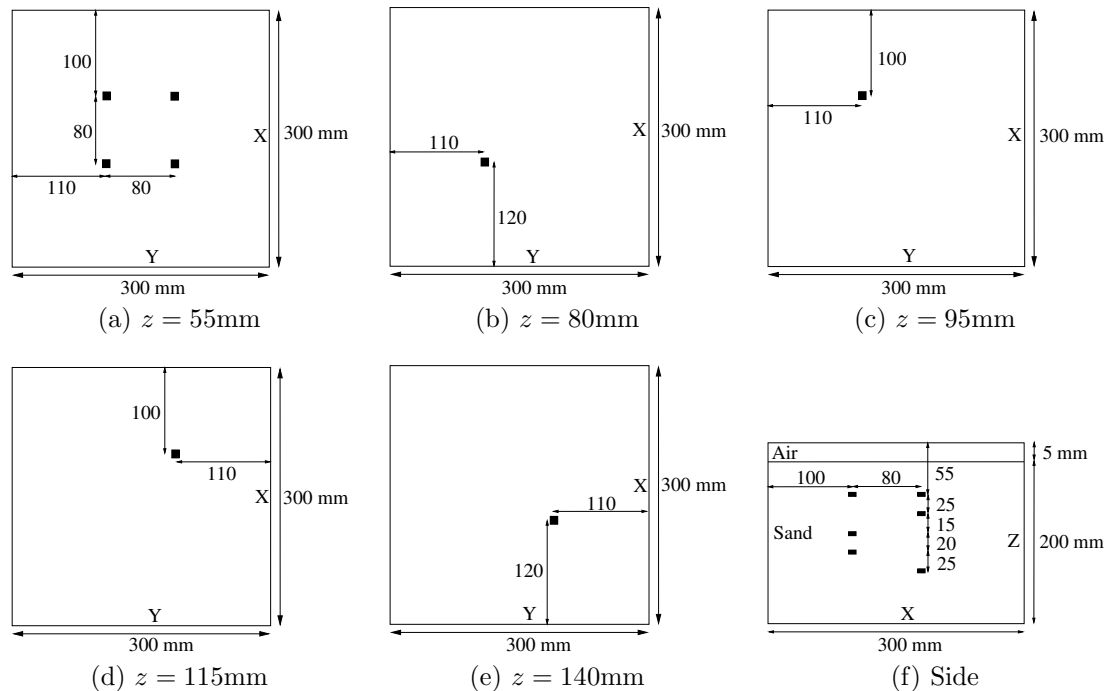


Figure 10: Schematic of the rubber pads in sand in the scanned area of Specimen 2, where unit in figure is mm, and z is the distance from the probe (not to scale).

high level of background artifacts mainly attributed to sand being an inhomogeneous media due to local variations in sand density. However, it can be seen that Cases 2 and 3 have removed the background artifacts since they both benefit from sparsity information of SAR images and TV penalty. Case 4 again has the highest level of background noise since it does not benefit from the SAR transform in the recovery process.

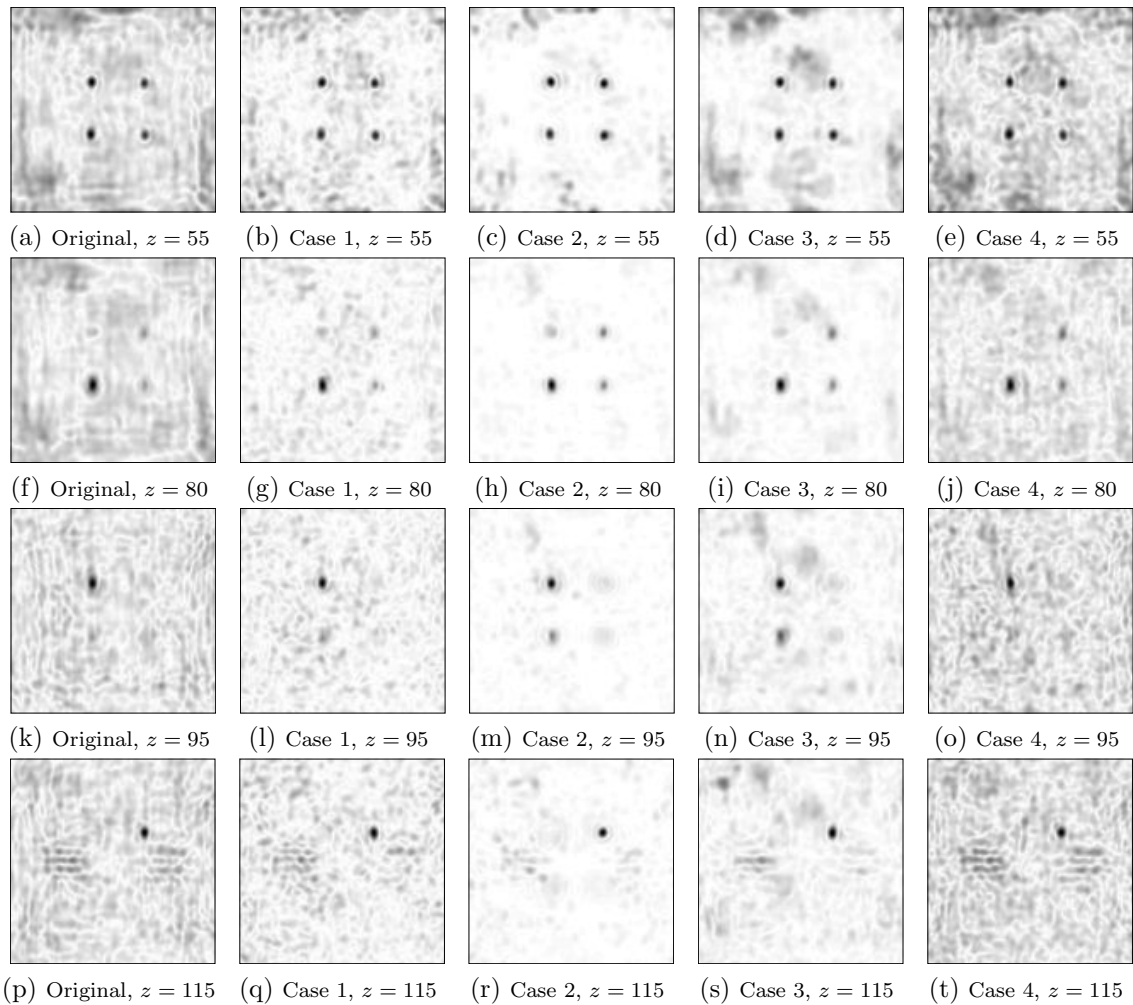


Figure 11: Slices of 3D SAR images of Specimen 2 from complete data and recovered data from 30% randomly selected points.

4.3. REBAR IN CEMENT-BASED MATERIALS - SPECIMEN 3

4.3.1. Experiment. The third and last set of experiments were performed on a mortar block with four rebars embedded in it. The rebars were placed in parallel at a distance 18 mm from surface of the block, as illustrated in Fig. 12. More details of this SUT may be found in [41]. The distance between the aperture and the surface of the block was 8 mm. An area of $260 \times 240 \text{ mm}^2$ was scanned with steps of 2 mm along X and Y dimensions. The reflection coefficients were measured and recorded by an HP8510C vector network analyzer.

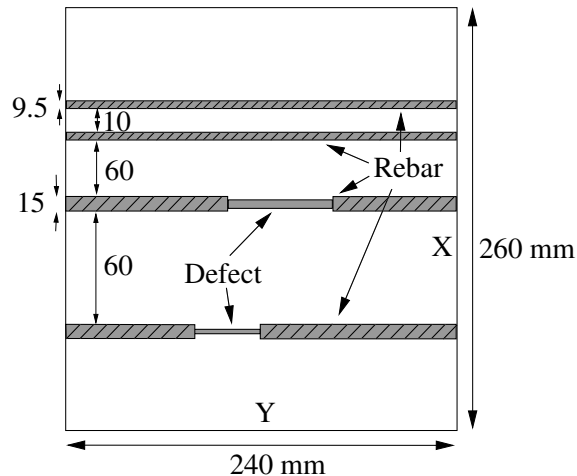


Figure 12: Schematic of the rebars in mortar in the scanned area of Specimen 3, where unit in figure is mm (not to scale).

4.3.2. Results. The results of the third set of experiments are illustrated in Fig. 13 consisting of the images from full-set measurements and the images recovered from 30% of the full-set data. It can be seen that Case 1 recovered the SAR images with low quality due to two main factors in the recovery process: sparsity and coherence [15, 16]. The SAR images are only sparse along two dimensions (X and Z) while they are not sparse along the Y dimension. Besides, the coherence between the

measurement and sparsifying matrices is high. Since the rebars are strong scatterers and were placed very close to the probe, the SAR images appear to be very similar to the measurement data. These two reasons reduce the probability of detecting the rebars using identity as the sparsifying domain and causes the algorithm to recover the targets with low quality. Using TV penalty in Case 2 decreased the background artifact level at the cost of losing the texture of targets. However, Case 3 recovered the rebars with good quality while reducing the background artifacts since Ψ was the DCT. Fewer textures on the rebars were blurred in the images as compared to Case 2. Finally, Case 4 maintained these textures with better quality, thanks to good sparse representation in DCT domain, albeit with a higher background artifact level.

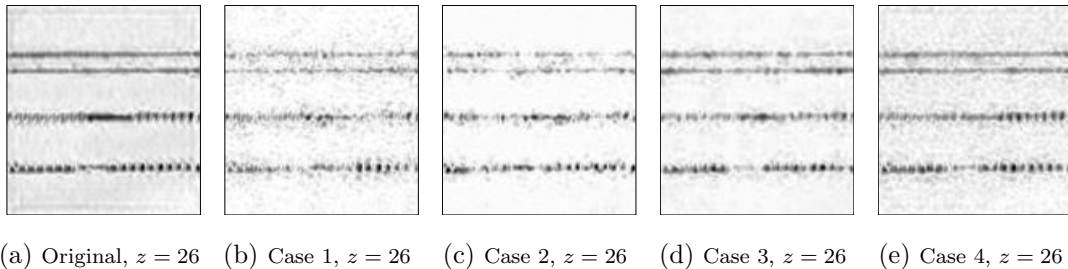


Figure 13: Slices of 3D SAR images of Specimen 3 from complete data and recovered data from 30% randomly selected points.

5. CONCLUSION

In this paper, we propose a new 3D image reconstruction method for compressed sensing microwave imaging using NUFFT-based SAR. High quality SAR images are recovered from incomplete measurements by exploiting an accurate SAR and R-SAR transform pair allowing the forward and reverse SAR to be applied in each iteration of CS and ensuring the convergence of the CS algorithm. A new low-complexity

truncation repair method is also proposed to reduce the truncation error in practical application of the NUFFT algorithm in the reverse SAR transform. The performance of the proposed algorithm is demonstrated using three experiments. It is shown that the proposed model recovers the sparse targets very well and at the same time better removes the background artifacts than using conventional full-set measurement approach.

6. APPENDIX (MATRIX REPRESENTATION OF SAR TRANSFORM)

Although SAR and R-SAR involve nonlinear mapping of k_z points, they are linear operators and can be represented as matrix operation. For 2D SAR we have

$$\mathbf{\Omega}_{2D} = \mathbf{W}_{2D}^H \times (\mathbf{E}_{2D} \circ \mathbf{W}_{2D}) \quad (30)$$

where \times denotes the matrix product, \circ denotes the Hadamard product, \mathbf{W}_{2D} is the 2D discrete Fourier transform matrix, and matrix \mathbf{E}_{2D} is defined as

$$\mathbf{E}_{2D} = \bar{\mathbf{e}} \otimes \begin{bmatrix} 1 & 1 & \cdots & 1 \end{bmatrix}_{1 \times (N_X N_Y)} \quad (31)$$

with \otimes denoting Kronecker product and N_X and N_Y being the number of samples along X and Y dimensions, respectively. Vector $\bar{\mathbf{e}}$ is calculated as

$$\bar{\mathbf{e}} = \begin{bmatrix} \mathbf{e}_1^H & \mathbf{e}_2^H & \cdots & \mathbf{e}_l^H & \cdots & \mathbf{e}_{N_X}^H \end{bmatrix}^H \quad (32)$$

where the $N_Y \times 1$ vector \mathbf{e}_l is the column of matrix \mathbf{e} defined as

$$\mathbf{e}_{xy}(l, j) = \left[e^{-jz_j \sqrt{4k_l^2 - k_x^2 - k_y^2}} \right]_{xy} . \quad (33)$$

In (30), \mathbf{W}_{2D} , the 2D DFT matrix, is defined as

$$\mathbf{W}_{2D} = \mathbf{W}_{1D}^X \otimes \mathbf{W}_{1D}^Y \quad (34)$$

where \mathbf{W}_{1D}^X is the 1D discrete Fourier transform matrix along X dimension and is defined as

$$\mathbf{W}_{1D}^X = \frac{1}{\sqrt{N_X}} \begin{bmatrix} 1 & 1 & 1 & \dots & 1 \\ 1 & w & w^2 & \dots & w^{(N_X-1)} \\ 1 & w^2 & w^4 & \dots & w^{2(N_X-1)} \\ \vdots & \vdots & \vdots & & \vdots \\ 1 & w^{(N_X-1)} & w^{2(N_X-1)} & \dots & w^{(N_X-1)(N_X-1)} \end{bmatrix} \quad (35)$$

with $w = e^{-\frac{2\pi j}{N_X}}$. Matrix \mathbf{W}_{1D}^Y is defined similarly as 1D discrete Fourier transform matrix along Y dimension.

For 3D SAR, the equation (30) could be modified to

$$\mathbf{\Omega} = \mathbf{W}_{3D}^H \times (\mathbf{E}_{3D} \circ \mathbf{W}_{2D}) \quad (36)$$

where the \mathbf{E}_{3D} represents the exponential term in (1). Equation (36) is an approximate matrix representation of the SAR algorithm as explained in Section 3. Since nonuniform samples are utilized in the calculation of \mathbf{W}_{3D}^H , the SAR algorithm is usually calculated using accurate NUFFT's.

7. ACKNOWLEDGMENT

We wish to thank Dr. Sergey Kharkovsky for his valuable assistance in setting up the measurement apparatus. We thank both Dr. Kharkovsky and Dr. Reza Zoughi for their technical advise and expertise in Microwave NDE. This work was partially supported by the American Society for Nondestructive Testing (ASNT) fellowship to Hamed Kajbaf and by the National Science Foundation Graduate Student Fellowship to Joseph T. Case. It has also been partially supported by the University of Missouri Research Board fund.

III. ADAPTIVE BASIS SELECTION COMPRESSED SENSING

Hamed Kajbaf and Yahong Rosa Zheng

ABSTRACT—An adaptive basis selection (ABS) algorithm is proposed for compressed sensing (CS) image reconstruction. In contrast to conventional compressed sensing with a fixed sparsifying basis, the proposed ABS method adapts the basis to the image as the image evolves during the algorithm iterations. In this method, the sparsifying basis is selected from a set of bases based on information from incomplete measurements without any *a priori* knowledge of proper basis. The algorithm benefits from the ability to search through a diverse sets of bases for unknown signals. A decision metric is introduced based on both the sparsity of the image as well as the coherence between the measurement and sparsifying matrices. This decision metric makes the adapting process possible for practical applications. The results from our experiments indicate that the proposed algorithm is capable of recovering 2D synthetic aperture radar (SAR) images very well without compromising the complexity of the recovery process. In addition, the algorithm shows promising results for k -space imaging techniques.

1. INTRODUCTION

Both the sparse representation and compressibility of signals have previously been studied very well under data coding. Transform coding has shown very interesting results in sparsely representing signals and is widely used in data compression. Recently, compressed sensing (CS) theory has combined the approach of first sampling the signal and then compressing it by measuring the signal with the rate of sparsity [14, 15, 17]. In compressed sensing theory, sub-Nyquist sampling of a signal is achievable by utilizing the sparse representation of the signal with an orthogonal basis.

Consider a signal $\mathbf{f} \in \mathbb{C}^N$ and its transform coding \mathbf{c} with an orthonormal basis $\mathbf{\Psi} = [\boldsymbol{\psi}_1 \boldsymbol{\psi}_2 \dots \boldsymbol{\psi}_N]$, such that $\mathbf{f} = \mathbf{\Psi}\mathbf{c}$. If most of the information of the signal \mathbf{f} is contained in only a few elements of the transformed signal \mathbf{c} , signal \mathbf{f} is called *S-sparse* in basis $\mathbf{\Psi}$ if only S of its coefficients are significant and the rest $(N - S)$ coefficients are zero. Therefore, a fixed signal support T of size $|T| = S$ can form an *S-sparse* signal:

$$S = \|\mathbf{c}\|_0 \quad (1)$$

where $\|\cdot\|_0$ is the ℓ_0 pseudo-norm operator and counts the nonzero elements of the vector of coefficients \mathbf{c} .

In compressed sensing, the sparsity of the signal is used to sample the signal \mathbf{f} more efficiently by measuring $M < N$ linear combinations of the signal. Let us define the measurement matrix $\mathbf{\Phi}_\Omega \in \mathbb{R}^{M \times N}$ by selecting the rows of a measurement matrix $\mathbf{\Phi} \in \mathbb{R}^{N \times N}$ on a set $\Omega \subset \{1, 2, \dots, N\}$ with size $|\Omega| = M$ where $\mathbf{\Phi}$ models the linear measurement procedure. This procedure can be modeled in matrix form as

$$\mathbf{y} = \mathbf{\Phi}_\Omega \mathbf{f} \quad (2)$$

where \mathbf{y} is the measured signal. The inverse problem is to recover the original signal from linear measurements. In general, this inverse problem is underdetermined with infinite solutions which satisfy (2). In compressed sensing, the sparsity of the signal is used to find a unique sparse solution for this problem.

Compressed sensing is similar to the decoding procedure in transform coding; both estimate the signal by applying the inverse of encoder orthonormal basis $\mathbf{\Psi}$, on the sparse coefficients \mathbf{c} , supported on set T . CS differs from transform coding in that both the location of support T and the value of the coefficients at these locations \mathbf{c}_T are unknown. The only known variable is a sampled linear combination of the signal.

Proper sparse representation in CS is essential for an accurate recovery of the signal. Conventionally, a fixed basis is used in CS to recover data from an incomplete measurement. In this scenario, it is assumed we know the proper basis in advance. This assumption is not very accurate for many practical applications, especially when we have an incomplete set of data available.

Available literature proposes both dictionary learning and best basis selection compressed sensing. These methods address the issue of selecting the proper basis by evolving the best basis during the recovery procedure [42–47]. These methods systematically develop a dictionary without any assumption of a global sparse representation. In this way, the dictionary adapts itself to the signal as the signal is recovered using CS. The systematic approach for either learning a dictionary or selecting bases is usually used to decrease the complexity of basis searching algorithms. The algorithm, however, loses diversity of search requiring some assumptions on sparse representation of the signal.

In this paper, a new adaptive basis selection (ABS) algorithm is proposed to address the issue of selecting a proper basis without compromising the complexity of the recovery process. In this approach, the proper basis is selected from a set of bases according to both its sparsifying capability and its incoherence with the measurement domain. As the signal is recovered iteratively and a more accurate estimation of the signal is available, the algorithm selects the proper basis more accurately. This proposed method can benefit from a diverse set of bases. In other words, for an unknown signal, a diverse set of bases can be used for a better sparse representation and, consequently, increasing the chance of recovery.

1.1. APPLICATIONS

We need to know the sparsifying basis from only incomplete measurements for a perfect recovery of an unknown signal. A proper basis can be determined in advance for applications in which the sparsity characteristics of the desired signal is not changing in different experiments. One possible method involves calibrating the recovering process using a given test signal for one experiment in a different basis and then comparing the recovered signals. For other experiments, we use a fixed basis (as determined in the calibration procedure) assuming that the sparsity characteristics are not changed. This assumption, however, is not always accurate. Thus, the adaptive basis selection compressed sensing is proposed in this paper to address this issue.

In this paper, two applications of the proposed method are presented and the performance and results are discussed. The first application is synthetic aperture radar (SAR) imaging for nondestructive testing of materials. The second application is k -space imaging for situations in which the frequency components of the image are available for measurement.

Microwave SAR imaging is a high resolution technique that can be exploited to detect discontinuities in critical structures. It does so by raster scanning a specimen under test (SUT) using a single antenna probe (e.g., an open-ended waveguide). This scanning procedure is very time consuming; a relatively large SUT might require hours of data acquisition. Random spatial measurements have been used to significantly reduce this acquisition time. The signal is then recovered using ℓ_1 -norm minimization with different orthogonal bases [21, 22]. The drawback to this technique is that the proper sparsifying basis is determined by first trying different bases and then choosing the one with the best SAR image quality. This approach is not desired in practice as the proper basis could be different for different SUTs. In contrast, the adaptive basis

selection approach chooses the proper basis iteratively as the signal is evolved using ℓ_1 -norm minimization. This application is discussed in detail in Section 2.

The other application of the adaptive basis selection is in k -space imaging using compressed sensing. In this imaging method, frequency components of an image are measured randomly. A basis is then selected from *a priori* knowledge of the proper basis and the image is recovered using the fixed basis. Adaptive basis selection compressed sensing is exploited to recover the images without any knowledge of the proper basis. This application is discussed in Section 5.

2. FIXED BASIS AND BEST BASIS CS FOR IMAGE PROCESSING

2.1. FIXED BASIS

The sparsity of the signal helps solve the system of equations (2) by searching for the sparsest vector of coefficients \mathbf{c} which matches the incomplete measurement signal \mathbf{y} . By defining both $\mathbf{A} = \Phi\Psi$ and $\mathbf{A}_\Omega = \Phi_\Omega\Psi$, this can be formulated as

$$\min_{\mathbf{c} \in \mathbb{C}^N} \|\mathbf{c}\|_1 \quad \text{subject to} \quad \mathbf{y} = \mathbf{A}_\Omega \mathbf{c}. \quad (3)$$

Convex optimization (3) is proved to recover \mathbf{f} with a high probability from linear measurements if some conditions are satisfied [16]. The minimum number of linear measurements guaranteeing a perfect recovery is related to both the sparsity of the signal and the coherence between the measurement and sparsifying bases. The coherence $\mu(\Phi, \Psi)$ between the measurement matrix Φ and the transform matrix Ψ is defined as

$$\mu(\Phi, \Psi) = \sqrt{N} \max_{1 \leq u, v \leq N} |\langle \phi_u, \psi_v \rangle| \quad (4)$$

which is an indication of how correlated the measurement and the sparsifying bases are.

Finite differences are usually used as a sparsifying transform for a 2D signal if variations of the signal are very sharp with small variation in the background. The objective function in (3) is then replaced by total variation (TV). The TV penalized objective function can be combined with other sparsifying bases. This can be interpreted as requiring the image to be sparse by both the specific basis and finite differences at the same time. In this case, (3) can be written as

$$\min_{\mathbf{c} \in \mathbb{C}^N} \lambda_\ell \|\mathbf{c}\|_1 + \lambda_t \text{TV}(\Psi \mathbf{c}) + \|\mathbf{y} - \mathbf{A}_\Omega \mathbf{c}\|^2 \quad (5)$$

where λ_ℓ and λ_t are weighting factor to determine the emphasize on ℓ_1 -norm or TV penalty, respectively [36].

The basis Ψ is fixed and is assumed to be known in advance for recovering a signal from incomplete measurements. Otherwise, one should find \mathbf{c} by guessing the basis Ψ . If the results are not satisfying, another basis should be tried and the signal is recovered in the new basis. This procedure is repeated until a proper basis is found which sparsifies the signal well and, at the same time, is incoherent with the measurement basis. This approach might be very computationally complex and, for some applications, impossible in practice.

2.2. BEST BASIS AND DICTIONARY LEARNING

The problem of selecting a proper basis prior to data recovery using CS is discussed in the literature under both best basis selection and dictionary learning. The method of best basis compressed sensing has been proposed to address the issue of selecting a proper basis in fixed basis compressed sensing [43]. In this approach, the best basis is optimized to obtain the best possible approximation of the signal

for a given sparsity. The problem is solved through the unconstrained optimization problem by minimizing a Lagrangian

$$\kappa^* = \arg \min_{\kappa \in K} \mathcal{E}(\mathbf{c}, \mathcal{B}^\kappa, t)$$

$$\mathcal{E}(\mathbf{c}, \mathcal{B}^\kappa, t) = \min_{\mathbf{c}^\kappa \in \mathbb{C}^N} \frac{1}{2} \|\mathbf{y} - \Phi \Psi \mathbf{c}\|_2^2 + t \|\mathbf{c}\|_1 \quad (6)$$

where \mathcal{B}^κ is an orthonormal basis and t is the Lagrange multiplier. A tree structure is then proposed to produce the set of bases \mathcal{B} . While this approach solves the problem of selecting a proper basis, it suffers from a high computationally complex algorithm due to optimizing two objective functions at the same time.

A dictionary learning compressed sensing method is proposed in [46] for k -space MR imaging. In this method, the dictionary is adapted to a particular image and, at the same time, determines the missing k -space components. A patch-based approach is used for learning the dictionaries. The image is then recovered in a two-step alternating scheme. In the first step, the dictionary is updated while the image is kept fixed. In the second step, the dictionary is fixed while the image is updated. Other methods have been proposed [42] for joint design and optimization for learning the dictionary and measurement matrix. In this approach, a training data set is used for the simultaneous learning of sparse representation and measurement matrix.

3. ADAPTIVE BASIS SELECTION (ABS) COMPRESSED SENSING

In this section, we introduce the proposed adaptive basis selection compressed sensing method. In this method, the proper basis is selected from a set of bases based on the proposed decision metric. The signal is then recovered using ℓ_1 -norm minimization with an iterative approach. A more accurate estimation of the desired signal is available in each iteration of the signal recovery. Consequently, the decision metric can estimate the proper basis more accurately, causing the algorithm to switch to a new basis if the initial guess is not the best one. As the signal evolves during the iterations, the basis keeps updating until the algorithm converges.

We discuss both the proposed ABS compressed sensing method and the proposed strategy for solving the problem of finding the proper basis. To solve the problem, we propose two algorithms. These algorithms are based on the alternating direction method (ADM) and the nonlinear conjugate gradient descent (CGD) with a backtracking line search. We also discuss the computational complexity of the proposed algorithms and compare it with the complexity of the existing fixed basis methods. Finally, we propose a practical decision metric to be used with adaptive basis selection method.

3.1. STRATEGY

Consider a set of N_K bases $\mathbf{B} = \{\Psi^\kappa\}_{\kappa \in K}$, $K = \{1, 2, \dots, N_K\}$, with the κ -th orthogonal basis denoted as Ψ^κ . The signal \mathbf{f} can be represented in each Ψ^κ basis as \mathbf{c}^κ , with the support set T^κ of size $|T^\kappa| = S^\kappa$. The best basis for recovering the signal from incomplete measurements \mathbf{y} is the Ψ^κ with the smallest S^κ . Before solving (3), however, we have no *a priori* knowledge of which Ψ^κ to choose for a given, incomplete measurement.

We define η as

$$\eta(\mathbf{c}^\kappa) = \mu^2(\Phi, \Psi^\kappa) |T^\kappa|. \quad (7)$$

This metric can be considered a measure of how well a sparsifying basis candidate Ψ^κ is able to recover the signal. Also, it can play the role of a decision metric. Therefore, during the recovery process (3), by searching for the smallest η , we will find the best sparse representation κ^* in the set K

$$\kappa^* = \arg \min_{\kappa \in K} \eta(\mathbf{c}^\kappa). \quad (8)$$

Using incomplete measurements to determine the best sparse representation typically produces inaccurate results. This search, however, can result in more accurate results if it is performed iteratively while solving either (3) or (5). We proposed a new iterative algorithm which solves either (3) or (5) and, at the same time, finds the best basis using (8).

We assume that the signal is sampled with a random sequence $\delta_1, \delta_2, \dots, \delta_N$ independent identically distributed Bernoulli distribution with probability

$$p(\delta_k) = \frac{M}{N}. \quad (9)$$

The measurement matrix Φ_Ω is then produced by rows from the identity matrix randomly sampled on the set Ω .

The proposed algorithm benefits from being able to add diversity to the set of bases for a better recovery of an unknown signal. In this way, the sparsifying basis is not limited to any class of basis. Additionally, different classes can be compared with the same metric. For example, both the discrete Fourier transform (DFT) and the discrete cosine transform (DCT) sparsify highly oscillating images very well. On the

contrary, wavelet-based transforms are more suitable for images which are sparsely represented with spatial-frequency transforms. As the set of bases \mathbf{A} is arbitrary and completely user-defined, the proposed algorithm is able to select from a diverse sets of bases. This property is in contrast to other basis selecting compressed sensing algorithms, such as [43], which require searching through one class of dictionary to avoid computational complexity overhead.

3.2. PROPOSED ABS ALGORITHM

In this section, we introduce the proposed algorithm for solving the adaptive basis selection compressed sensing. This algorithm is based on iteratively solving the basis pursuit problem and updating the sparsifying basis in each iteration based on the sparsity information of the signal. As the algorithm goes through the iterations, a better approximation of the original signal increases the chance of selecting the proper sparsifying basis. Reciprocally, selecting the proper sparsifying basis leads to a higher chance of recovery compared to fixed basis CS.

Algorithm 2 illustrates the iterative procedure for solving the proposed method, where I_e is an integer and a user-defined parameter for stopping the basis update procedure. If the sparsifying basis is kept unchanged for I_e iterations, the algorithm stops updating the basis to decrease the overall computational complexity of the recovery process. Typically, I_e is a small number and the basis update procedure stops after the first few iterations.

Two iterative algorithms are developed to investigate the performance of the proposed algorithm. The first algorithm uses the alternating direction method (ADM), as proposed in [28], to solve the ℓ_1 minimization problem. The second algorithm uses the nonlinear conjugate gradient descent (CGD) approach with a backtracking line search, as proposed in [36].

According to the general framework of ADM, the augmented Lagrangian sub-problem of (3) for a given $\kappa \in K$ is

$$\min_{\mathbf{c}^\kappa \in \mathbb{C}^N} \lambda_\ell \|\mathbf{c}^\kappa\|_1 + \lambda_t \text{TV}(\Psi^\kappa \mathbf{c}^\kappa) + \text{Re}(\mathbf{z}^H (\mathbf{A}^\kappa \mathbf{c}^\kappa - \mathbf{y})) + \frac{\beta}{2} \|\mathbf{A}^\kappa \mathbf{c}^\kappa - \mathbf{y}\|^2 \quad (10)$$

where $\mathbf{z} \in \mathbb{C}^M$ is a multiplier and $\beta > 0$ is a penalty parameter. Reformulating (10), we have

$$\min_{\mathbf{c}^\kappa \in \mathbb{C}^N} \lambda_\ell \|\mathbf{c}^\kappa\|_1 + \lambda_t \text{TV}(\Psi^\kappa \mathbf{c}^\kappa) + \frac{\beta}{2} \|\mathbf{A}^\kappa \mathbf{c}^\kappa - \mathbf{y} - \mathbf{z}/\beta\|^2. \quad (11)$$

Algorithm 2 Adaptive Basis Selection (ABS)

- 1: $\kappa_0 := \arg \min_{\kappa \in K} \eta((\mathbf{A}_\Omega^\kappa)^H \mathbf{y})$
 - 2: $\mathbf{c}_0 := (\mathbf{A}_\Omega^{\kappa_0})^H \mathbf{y}$
 - 3: $i := 0$
 - 4: **repeat**
 - 5: Update $\mathbf{c}_{i+1}^{\kappa_i}$ based on $\mathbf{c}_i^{\kappa_i}$
 - 6: **if** κ is changed during the last I_e consecutive iterations **then**
 - 7: $\kappa_{i+1} := \arg \min_{\kappa \in K} \eta(\mathbf{c}_{i+1}^\kappa)$
 - 8: $\mathbf{c}_{i+1}^{\kappa_{i+1}} := (\Psi^{\kappa_{i+1}})^H \Psi^{\kappa_i} \mathbf{c}_{i+1}^{\kappa_i}$
 - 9: **else**
 - 10: $\kappa_{i+1} := \kappa_i$
 - 11: $\mathbf{c}_{i+1}^{\kappa_{i+1}} := \mathbf{c}_{i+1}^{\kappa_i}$
 - 12: **end if**
 - 13: $i := i + 1$
 - 14: **until** stopping criteria is met
-

The proposed method, as in Algorithm 2, with the ADM approach, can be approximated to

$$\kappa_i = \arg \min_{\kappa \in K} \eta(\mathbf{c}_{i-1}^\kappa)$$

$$\min_{\mathbf{c}^{\kappa_i} \in \mathbb{C}^N} \lambda_\ell \|\mathbf{c}^\kappa\|_1 + \lambda_t \text{TV}(\Psi^\kappa \mathbf{c}^\kappa) + \beta \left(\text{Re}(\nabla_i^H(\mathbf{c}^{\kappa_i} - \mathbf{c}_i^{\kappa_i})) + \frac{1}{2\tau} \|\mathbf{c}^{\kappa_i} - \mathbf{c}_i^{\kappa_i}\|^2 \right) \quad (12)$$

where $\tau > 0$ is a proximal parameter and

$$\nabla_i \triangleq (\mathbf{A}_\Omega^\kappa)^H (\mathbf{A}_\Omega^\kappa \mathbf{c}_i^\kappa - \mathbf{y} - \mathbf{z}_i / \beta) \quad (13)$$

is the gradient of the quadratic term in (11) at point $\mathbf{c}_i^{\kappa_i}$, with i indicating the iteration number. To solve the problem without a TV penalty, we can simply set $\lambda_\ell = 1$ and $\lambda_t = 0$. The minimization (12) can be explicitly solved by

$$\mathbf{c}_{i+1}^{\kappa_i} = \text{shrink} \left(\mathbf{c}_i^{\kappa_i} - \tau \nabla_i, \frac{\tau}{\beta} \right) \triangleq \max \left(|\mathbf{c}_i^{\kappa_i} - \tau \nabla_i| - \frac{\tau}{\beta}, 0 \right) \frac{\mathbf{c}_i^{\kappa_i} - \tau \nabla_i}{|\mathbf{c}_i^{\kappa_i} - \tau \nabla_i|} \quad (14)$$

with all of the operations being performed element-wise. Line 5 of Algorithm 2 is then substituted by the following two lines:

$$\mathbf{c}_{i+1}^{\kappa_i} := \text{shrink}(\mathbf{c}_i^{\kappa_i} - \nabla_i, \tau/\beta)$$

$$\mathbf{z}_{i+1} := \mathbf{z}_i - \xi \beta (\mathbf{A}_\Omega^{\kappa_i} \mathbf{c}_{i+1}^{\kappa_i} - \mathbf{y})$$

where $\xi > 0$ is a constant.

The second approach uses nonlinear CGD with a backtracking line search. For simplicity, we set the objective function as

$$\mathcal{C} = \lambda_\ell \|\mathbf{c}^\kappa\|_1 + \lambda_t \text{TV}(\Psi^\kappa \mathbf{c}^\kappa) + \|\mathbf{A}_\Omega^\kappa \mathbf{c} - \mathbf{y}\|^2 \quad (15)$$

The conjugate gradient of the objective function is then calculated by

$$\nabla \mathcal{C} = \lambda_\ell \nabla \|\mathbf{c}^\kappa\|_1 + \lambda_t \nabla \text{TV}(\Psi^\kappa \mathbf{c}^\kappa) + 2(\mathbf{A}_\Omega^\kappa)^H (\mathbf{A}_\Omega^\kappa \mathbf{c} - \mathbf{y}). \quad (16)$$

As the absolute value function in ℓ_1 is not differentiable, the approximation $|c_r| \approx \sqrt{c_r^H c_r + \nu}$ is used where ν is a smoothing parameter. Therefore, $\frac{d}{dc_r} \approx \frac{c_r}{\sqrt{c_r^H c_r + \nu}}$. Consequently, line 5 of Algorithm 2 is substituted by:

```

t := 1
repeat
  t := \zeta t
until  $\mathcal{C}(\mathbf{c}_i^{\kappa_i} + t\Delta\mathbf{c}_i^{\kappa_i}) > \mathcal{C}(\mathbf{c}_i^{\kappa_i}) + \zeta t \text{Re}\{\nabla\mathcal{C}_i^H \Delta\mathbf{c}_i^{\kappa_i}\}$ 
 $\mathbf{c}_{i+1}^{\kappa_i} := \mathbf{c}_i^{\kappa_i} + t\Delta\mathbf{c}_i^{\kappa_i}$ 
 $\Delta\mathbf{c}_{i+1}^{\kappa_i} := -\nabla\mathcal{C}_{i+1} + \frac{\|\nabla\mathcal{C}_{i+1}\|^2}{\|\nabla\mathcal{C}_i\|^2} \Delta\mathbf{c}_i^{\kappa_i}$ 

```

where ς and ζ are the line search parameters.

3.3. COMPUTATIONAL COMPLEXITY

In this section, we discuss the computational complexity of the proposed algorithms and will compare it with that of fixed basis compressed sensing. Both for fixed basis compressed sensing and proposed method, it is a common practice to calculate the matrix multiplication $\mathbf{f} = \Psi^\kappa \mathbf{c}$ with an implicit function. Let us assume that the computing time of this implicit function is $X^\kappa(N)$ with biggest order of computation $\mathcal{O}(X^\kappa(N))$ or simply \mathcal{O}^κ .

The order of computations per iteration for fixed basis compressed sensing using the ADM approach is $2\mathcal{O}^\kappa$, where $\kappa \in K$ is a candidate basis. By repeating the recovery process using all bases and finding the best recovered signal, the order of computations will be $2 \sum_{\kappa=1}^{|K|} \mathcal{O}^\kappa$. This is while the order of computations for the proposed adaptive basis selection method using ADM approach is $\mathcal{O}^{\kappa_{i+1}} + 2\mathcal{O}^{\kappa_i} +$

$\sum_{\kappa=1}^{|K|} \mathcal{O}^\kappa$ for $i \leq I_e$ and is $2\mathcal{O}^{\kappa^*}$ for $i > I_e$. To compare the complexity of fixed basis CS with ABS, assume that we sort the bases, $\kappa \in \{1, 2, \dots, |K|\}$, with respect to their order of complexity with ascending order. The worst case for ABS occurs when the best basis in the set has the highest order of complexity, $\mathcal{O}^{|K|}$. In practice, for $|K| > 3$, the order of complexity per iteration for ABS is less than that of fixed basis applied on all bases. In other words, if the number of candidate bases is larger than three, ABS needs fewer computations than fixed bases repeated for all bases. Note that this is the worst case study and if the best basis is not the most complex one, the order of computations of ABS might be much less than fixed basis. Also, the basis updating procedure stops after I_e iterations.

Assume that fixed basis CS using $\kappa \in K$ candidate basis converges in I^κ iterations. The overall computational time for all bases is then $2 \sum_{\kappa=1}^{|K|} \mathcal{O}^\kappa I^\kappa$. On the other hand, ABS converges in $I^{\kappa^*} + I_e$ with κ^* being the best candidate basis and I_e being the number of iterations needed to find the best basis. Therefore, the overall computational time for worst case study of ABS algorithm is $\left(3\mathcal{O}^{|K|} + \sum_{\kappa=1}^{|K|} \mathcal{O}^\kappa\right) I_e + 2\mathcal{O}^{\kappa^*} I^{\kappa^*}$. In practice, $I_e \ll I^\kappa, \forall \kappa \in K$ and the overall complexity of the proposed algorithm is much less than the fixed basis algorithm repeated over different bases.

With the same discussion, we can study the computational complexity of CGD approach. The order of complexity of fixed basis CS with CGD algorithm repeated for all bases is $4 \sum_{\kappa=1}^{|K|} \mathcal{O}^\kappa$. On the other hand, the order of complexity of ABS is $5\mathcal{O}^{\kappa_i} + \sum_{\kappa=1}^{|K|} \mathcal{O}^\kappa$. Again, for practical applications and for $|K| > 2$, the order of complexity of ABS is less than that of fixed basis applied on all bases.

3.4. SPARSITY METRIC

As discussed earlier, the sparsity of a signal plays a critical role in performance of data recovery techniques. In practice, most signals have S significant coefficients and the rest of the coefficients are close to zero, but not exactly zero. The ℓ_1 -norm

optimization is capable of recovering these kinds of signals with good approximation despite the fact that they are not strictly sparse as defined in (1). Therefore, the definition of sparsity as in (1) is not a proper sparsity metric in practice.

Several measures of sparsity are proposed in the literature to measure the sparsity of a signal for practical purposes [48–50]. These measures include ℓ_p -norm, kurtosis, impulsiveness, pq-mean, and the Gini index. After evaluating these measures of sparsity, we selected impulsiveness based on its reliability and computational complexity. As the sparsity increases, impulsiveness of the signal increases. The Gini index is also a reliable sparsity metric [48–51], but it has higher computational complexity. As ABS selects the best basis in each iteration based on the sparsity metric, we need a low complexity measure and the Gini index is not suitable for this application.

Impulsiveness is typically used in characterization of impulsive noise and is defined as [52]

$$\gamma_{im}(\mathbf{c}^\kappa) = \frac{E\{|c_r^\kappa|^2\}^{\frac{1}{2}}}{E\{|c_r^\kappa|\}}. \quad (17)$$

When the exact statistics of c_r 's are not available, the estimate of impulsiveness reduces to the special case of pq-mean with $p = 2$ and $q = 1$ defined as

$$\gamma_{pq}(\mathbf{c}^\kappa) = \frac{(\frac{1}{N} \sum_{r=1}^N |c_r^\kappa|^p)^{\frac{1}{p}}}{(\frac{1}{N} \sum_{r=1}^N |c_r^\kappa|^q)^{\frac{1}{q}}} \quad p < q \quad (18)$$

where the negative sign is removed from the definition to make the sparsity measure positive.

It should be noted that all c_r 's must be available to calculate these measures of sparsity. However in compressed sensing applications, only incomplete measurements are available. Therefore, we need to estimate the sparsity metric from an incomplete set of data.

In this paper two measurement methods are used for two different sets of data. The first measurement method is the spatial sampling for which the measurement matrix is a matrix of spikes. The second measurement method is the frequency domain sampling and the measurement matrix is the incomplete Fourier matrix. We have noticed that for spatial sampling bilinear interpolation of the signal results in the best estimate of measures of sparsity. On the other hand, for frequency domain sampling, zero padding the missing Fourier coefficients results in the best estimate of measures of sparsity.

3.5. COHERENCE

Besides sparsity, coherence between the measurement matrix and transform matrix is one of the factors which determine the sufficient number of samples to recover a signal [15, 16]. In this paper, we proposed a decision metric based on both sparsity and coherence (4), to select between different bases. The metric is defined as

$$\tilde{\eta}(\mathbf{c}^\kappa)^\kappa = \frac{\mu^2(\Phi, \Psi^\kappa)}{\gamma(\mathbf{c}^\kappa)} \quad (19)$$

4. APPLICATION TO WIDEBAND 2D SAR IMAGING

In this section, two applications of the proposed method are discussed and the results are presented. The first application is synthetic aperture radar (SAR) imaging for nondestructive testing of materials. The second application is k -space imaging for the situations where the frequency components of the image are available for measurement.

For the SAR imaging application, the hardware system performs the measurement in the spatial domain and the measurement matrix is a matrix of spikes. On the

other hand, the k -space imaging application performs the measurement in frequency domain and the measurement matrix is the incomplete Fourier matrix. Five transform bases are selected for each measurement method to show the performance of the proposed algorithm. For spatial sampling which is used for the SAR imaging application, the selected bases are: 2D SAR, 2D discrete Fourier transform, 2D discrete cosine transform, 2D Daubechies 1 wavelet with one level decomposition (DB1(1)), and 2D DB1 with two level decomposition (DB1(2)). For frequency domain sampling which is used for k -space imaging application, the identity matrix (EYE) is used instead of 2D SAR. The rest of the bases are the same as spatial sampling. Table 1 lists the set of bases which are used in this paper.

Table 1: Sets of bases

Basis	1	2	3	4	5
Application	SAR	DFT	DCT	DB1 (1)	DB1 (2)
k -space Imaging	EYE	DFT	DCT	DB1 (1)	DB1 (2)

4.1. SYNTHETIC APERTURE RADAR IMAGING

Microwave synthetic aperture radar (SAR) imaging is a nondestructive method for inspecting materials and detecting defects and discontinuities in critical structures. Conventionally, a specimen under test (SUT) is raster scanned with an antenna probe to form high resolution images of the SUT. The cost of high resolution images is the time spent for scanning and acquiring the data with very small spatial steps.

In SAR imaging, a microwave probe illuminates an area of the SUT and the hardware device measures the backscattered complex-valued reflection coefficients, $\mathbf{f}(x', y', \omega_s)$, which are the superposition of reflections from all points in the illuminated

area with x' and y' being the probe location and ω_s being the swept temporal angular frequency. The reflection coefficients

$$\mathbf{f}(x', y', \omega_s) = \iint \mathbf{s}(x, y, \omega_s, z_t) e^{-j2k_s \sqrt{(x-x')^2 + (y-y')^2 + z_t^2}} dx dy \quad (20)$$

are superposition of reflections from all points in the illuminated area where $k_s = \frac{\omega_s}{c}$ is the wavenumber and $\mathbf{s}(x, y, \omega_s, z_t)$ is the reflectivity function of the target at location x and y and distance z_t from the probe.

After decomposing the spherical wave propagation into a superposition of plane wave components and dropping the distinction between primed and unprimed coordinates, the estimate of the range migration formula becomes

$$\mathbf{s}(x, y, \omega_s, z_t) = \mathcal{F}_{2D}^{-1} \left\{ \mathcal{F}_{2D} \{ \mathbf{f}(x, y, \omega_s) \} e^{-jz_t \sqrt{4k_s^2 - k_x^2 - k_y^2}} \right\} \quad (21)$$

where $\mathcal{F}_{2D} \{ \cdot \}$ and $\mathcal{F}_{2D}^{-1} \{ \cdot \}$ are the 2D Fourier and inverse Fourier transform operators, respectively, k_x and k_y are the Fourier transform variables corresponding to x and y , respectively, and c is the speed of light [5, 12, 13, 20]. To improve the quality of images, the reflection coefficients, $\mathbf{f}(x, y, \omega_s)$, are measured for a range of frequencies. Then, all focused images are averaged for a given distance of the probe to the target z_t ,

$$\mathbf{s}(x, y, z_t) = \frac{1}{N_\omega} \sum_{s=1}^{N_\omega} \mathbf{s}(x, y, \omega_s, z_t) \quad (22)$$

where N_ω is the number of frequency points.

The scan time can be reduced by randomly selecting spatial acquisition points from a uniform grid and optimizing the scan path to minimize the total traveling distance. In the compressed sensing SAR imaging technique, the reflection coefficients are sampled randomly from a uniform grid along the X and Y dimensions. Then, CS

is exploited to recover the uniform grid data and (21) and (22) are used to form 2D images of the target at different heights [21, 22].

The 2D SAR transform is calculated using (21) and can be expressed in matrix format

$$\Psi_{SAR} = \Psi_{2DFT}^H \times (\mathbf{E} \circ \Psi_{2DFT}) \quad (23)$$

where \times denotes the matrix product, \circ denotes the Hadamard product, Ψ_{SAR} is the 2D SAR matrix, and Ψ_{2DFT} is the 2D Fourier transform matrix and is formed by

$$\Psi_{2DFT} = \Psi_{FT} \otimes \Psi_{FT} \quad (24)$$

where \otimes denotes Kronecker product and Ψ_{FT} is the 1D Fourier transform matrix. The exponential factor in (21) is denoted by matrix \mathbf{E} and is calculated as

$$\mathbf{E}(s, t) = \bar{\mathbf{e}} \otimes \begin{bmatrix} 1 & 1 & \cdots & 1 \end{bmatrix}_{1 \times N} \quad (25)$$

where

$$\bar{\mathbf{e}} = \begin{bmatrix} \mathbf{e}_1^T & \mathbf{e}_2^T & \cdots & \mathbf{e}_l^T \end{bmatrix}^T \quad (26)$$

with \mathbf{e}_l being the columns of matrix \mathbf{e} defined as

$$\mathbf{e}_{mn}(s, t) = \left[e^{-jzt\sqrt{4k_s^2 - k_{xm}^2 - k_{yn}^2}} \right]_{mn} . \quad (27)$$

The 2D transform matrices for other bases are the Kronecker product of 1D bases

$$\Psi_{2D} = \Psi_{1D} \otimes \Psi_{1D} \quad (28)$$

where Ψ_{1D} is the 1D basis matrix corresponding to each 2D basis matrix, Ψ_{2D} .

4.2. RESULTS

The goal in adaptive basis selection compressed sensing SAR imaging is to find a proper sparse representation of $\mathbf{f}(x, y, \omega_s)$ from incomplete measured reflection coefficients, $\mathbf{y}(x, y, \omega_s)$. The hardware system is designed to randomly measure the reflection coefficients and the *a priori* knowledge of proper representation is not available from incomplete data. On the other hand, the proper sparse representation might be different for different SUTs. Using the proposed algorithm, the proper representation is selected adaptively as the signal is evolved during the recovery process. Spatial sampling is selected for SAR imaging because of hardware specifications. Therefore, the decision metric is based on bilinear interpolation of $\mathbf{y}(x, y, \omega_s)$'s.

To show the efficacy of the proposed method, experimental tests were conducted on an SUT which was eight rubber (Rbr) patches and one copper (Cu) patch fixed on a substrate at different heights using pieces of construction foams as physical support. The imaging probe is operating at 18 GHz to 26.5 GHz with frequency steps of 0.6 GHz. An area of 120mm \times 180mm is scanned and the reflections are received by the same antenna probe. The complex-valued reflection coefficients are measured and recorded by an HP 8510C vector network analyzer.

The ADM approach is used to recover the SAR images. To see the effect of the sparsifying basis on signal recovery, we have recovered SAR images using different bases. The results of the recovered images for $z = -28$ are shown in Fig. 1. It can be seen that different bases have recovered the images with different qualities. The closest one in terms of normalized root mean square (NRMS) error to the original image with complete measurement points is the one recovered using 2D DFT basis. The worse basis in terms of error is 2D DB1(1).

The same SAR images are recovered using the proposed algorithm with the ADM approach. The algorithm has detected the sparsest basis for all pairs of (ω_s, z_t) correctly and has evolved the signal in the correct basis. The resulting 2D compressed

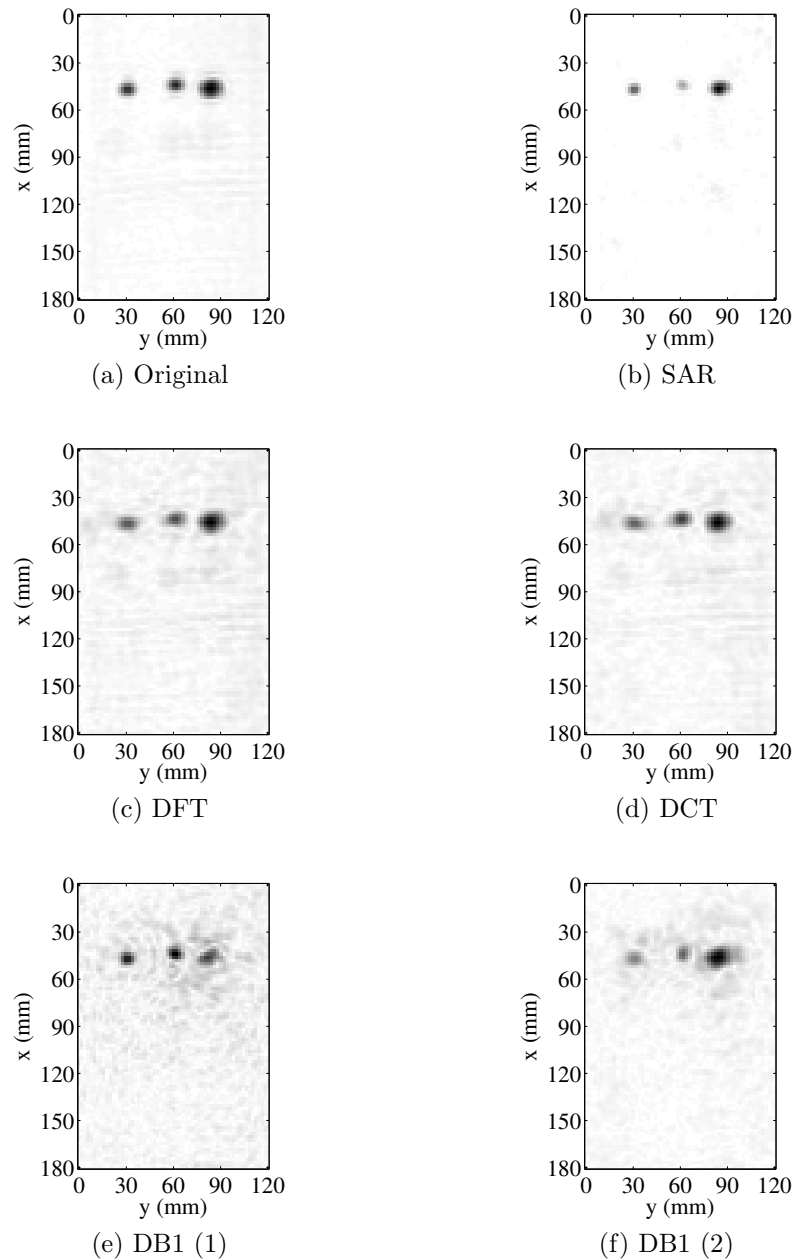


Figure 1: 2D SAR images of the SUT from complete data and recovered using fixed bases from 20% randomly selected points at $z = -28$.

sensing SAR images of the SUT using the proposed method is shown in Fig. 2 with 20% of the points used in the complete data. These figures show the SAR images focused on three different levels of the targets and images from substrate level.

The convergence of the proposed algorithm is studied for this set of images. Figure 3 illustrates the error and the decision metric behavior of the algorithm on the same plot. It can be seen that as the algorithm converges, it selects the best basis (DFT) and converges to the desired signal with this basis. The algorithm also selects DB1(1) as the worst basis and sorts all other bases in between these two bases. The initial guess for the sparsifying basis is based on initialization in Algorithm 2.

The robustness of the algorithm to initial basis is studied by forcing the algorithm to select a wrong initial basis. Figure 4 shows how the algorithm selects the best basis with different initialization. The numbers on the vertical axis indicate the bases according to Table 1. The maximum number of iterations for basis convergence, I_e , is 20. From the figure, it can be seen that the algorithm selects the best basis after the first iteration for all basis except SAR. When the sparsifying transform is selected as SAR for initialization, the algorithm selects SAR after 7 iterations as the best basis which is the second best basis in the set of bases.

5. APPLICATION TO K -SPACE IMAGING

5.1. K -SPACE IMAGING

The Shepp-Logan phantom is sampled in the frequency domain and is recovered using different sparsifying bases. The samples are randomly selected from frequency coefficients of the image with more concentration on lower frequencies. The images are recovered using fixed basis compressed sensing with TV penalty as in (5). The results of the image recovery using 30% of the frequency coefficients are shown in Fig.

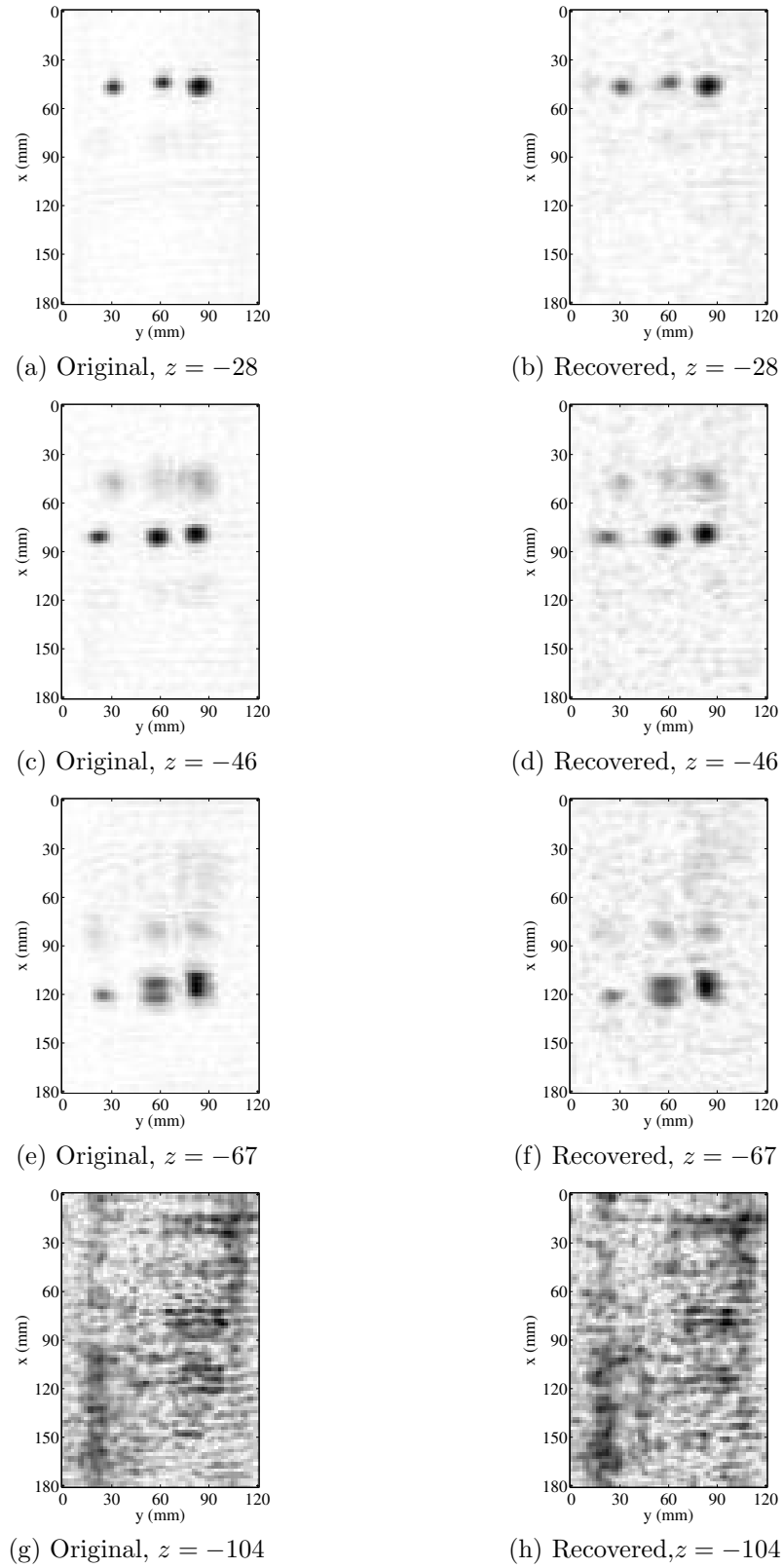


Figure 2: 2D SAR images of the SUT from complete data and recovered data from 20% randomly selected points using ABS.

5. From the figure, it can be seen that the best recovery is by using the identity matrix. The worst basis is 2D DFT as it is the same as the measurement basis and has the highest coherence.

5.2. RESULTS

To evaluate the performance of the proposed algorithm on k -space imaging the same image is recovered using the proposed algorithm with the CGD approach with

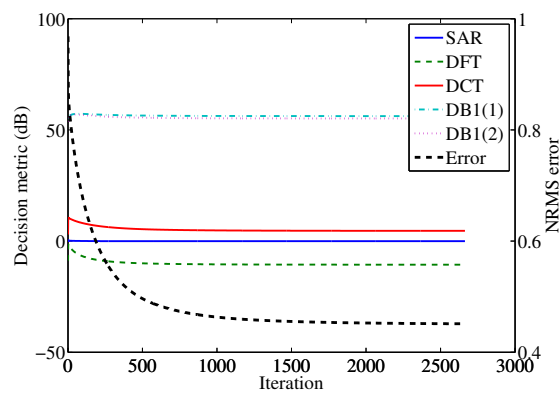


Figure 3: Decision metric and error vs. number of iterations for SAR data.

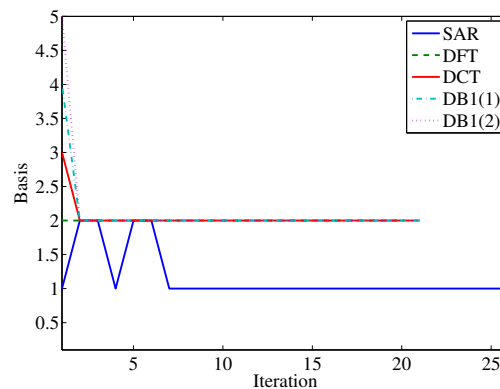


Figure 4: Basis convergence vs. number of iterations for SAR data for different basis initialization.

TV penalty. The algorithm selected the best basis as the identity matrix and the resulting image is shown in Fig. 6. The convergence of the algorithm is studied with respect to the changes in decision metric in Fig. 7. It can be seen that the algorithm has selected the best basis for recovery and has sorted all other bases correctly. Figure

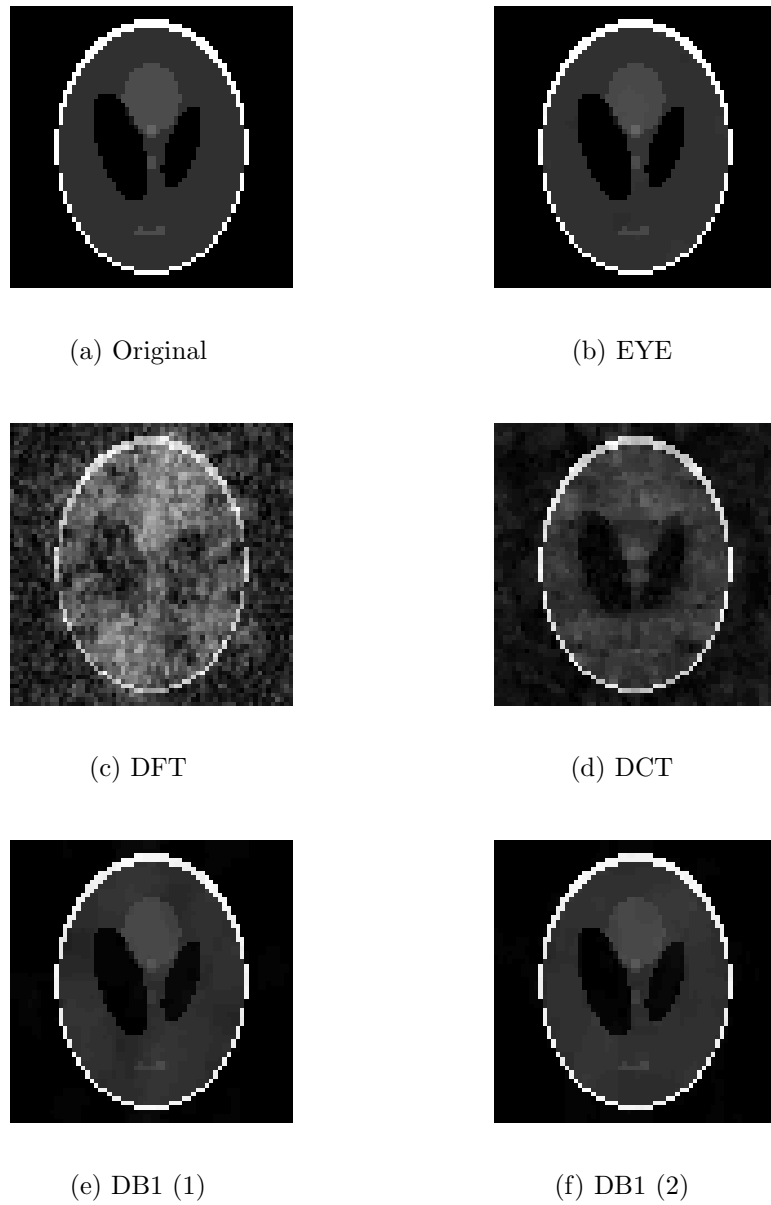


Figure 5: Shepp-Logan phantom images from complete data and recovered using fixed bases from 30% randomly selected frequency points.

8 shows the results of the study on robustness to initialization. It can be seen that initializations with all bases have converged to the identity matrix after the first iteration.



Figure 6: Shepp-Logan phantom images from complete data and recovered data from 30% randomly selected frequency points.

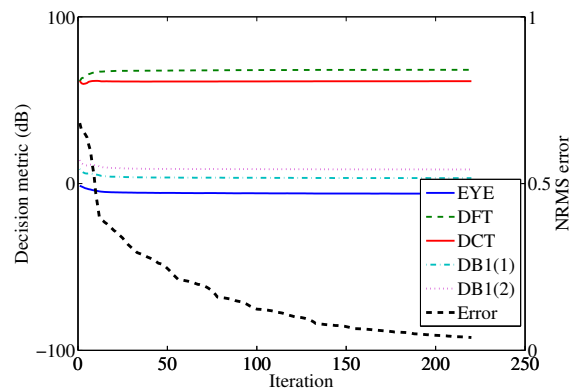


Figure 7: Decision metric and error vs. number of iterations for Shepp-Logan phantom data.

6. CONCLUSION

Recently developed compressed sensing theory has proposed a more efficient acquisition of signals by sampling below the conventional Nyquist rate. However, there is a need for selecting a proper basis for the recovering of signals using sparse representation. This is while no *a priori* knowledge of the proper basis is available before the signal is recovered. On the other hand, the proper basis should be selected based on incomplete measurements.

In this paper we proposed a low-computationally-complex algorithm called adaptive basis selection compressed sensing to recover images from incomplete measurement without any knowledge of the proper sparse representation. To detect the best basis from a set of bases, a decision metric is introduced to select between the bases as the signal is evolved during the iterations of the algorithm. The 2D synthetic aperture radar images and Shepp-Logan phantom data were used in this paper to show the performance of the proposed method. The results of our experiments showed that the proposed algorithm successfully selected the best basis adaptively and was capable of recovering the images with high accuracy.

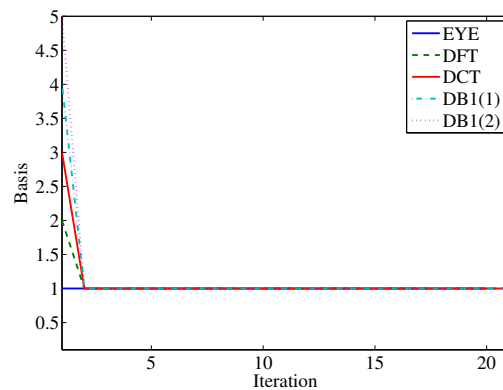


Figure 8: Basis convergence vs. number of iterations for Shepp-Logan phantom data for different basis initialization.

7. ACKNOWLEDGMENT

We wish to thank Dr. Sergey Kharkovsky and Dr. Reza Zoughi for their valuable assistance on the experiments. This work was partially supported by the ASNT fellowship award and by the University of Missouri Research Board fund.

IV. QUANTITATIVE AND QUALITATIVE COMPARISON OF SAR IMAGES FROM INCOMPLETE MEASUREMENTS USING COMPRESSED SENSING AND NONUNIFORM FFT

Hamed Kajbaf, Joseph T. Case, Yahong Rosa Zheng, Sergey Kharkovsky, and Reza
Zoughi

ABSTRACT—In this paper the performance of two wideband synthetic aperture radar (SAR) imaging methods from incomplete data sets are compared quantitatively and qualitatively. The first approach uses nonuniform fast Fourier transform (NUFFT) SAR to form images from nonuniform spatial and frequency data points. The second approach benefits from the emerging compressed sensing (CS) methodology to recover raw data from undersampled measurements. The results of our experimental tests show that CS has a better performance in terms of error and image contrast while NUFFT SAR has lower computational complexity.

1. INTRODUCTION

Microwave synthetic aperture radar (SAR) imaging is a high resolution nondestructive testing and evaluation (NDT&E) technique which can be exploited to detect discontinuities in critical structures by raster scanning using a single antenna probe (e.g. an open-ended waveguide) [1, 4, 5]. Wideband SAR is capable of determining depth of discontinuities and providing 3D images of specimens under test (SUT) such as spacecraft tiles, airplane coating, bonding of adhesive or composite materials. However, the drawback of microwave SAR imaging for NDT&E applications is the time needed for scanning the region of interest, which for a relatively large SUT might be hours of data acquisition. Reducing the number of spatial samples significantly helps in decreasing the acquisition time.

The emerging compressed sensing (CS) theory has introduced a method of reducing the number of samples by sampling below the conventional Nyquist rate [14, 17]. Nonuniform fast Fourier transform (NUFFT) SAR is another method for forming SAR images from incomplete data with low computational requirements. In this paper the performance of sample reduction in SAR imaging using CS and NUFFT SAR are compared in terms of metrics indicating the quality of the SAR images.

2. NUFFT SAR

Suppose that an antenna probe located at (x', y', z_0) illuminates a target and a general point on the target, (x, y, z) , reflects back the pulse. The same probe receives the backscattered coherent signal, $f(x', y', \omega)$, which is the superposition of reflection from all points in the illuminated area

$$f(x', y', \omega) = \iiint s(x, y, z) e^{-jkR} dx dy dz \quad (1)$$

where R is the range between the probe and the target point

$$R = \sqrt{(x - x')^2 + (y - y')^2 + (z - z_0)^2}$$

, $k = \frac{\omega}{c}$ is the wavenumber, c is the propagation speed, and $s(x, y, z)$ is the reflectivity function of the target, which is the ratio of the reflected field to the incident field. Decomposing the spherical wave propagation into a superposition of plane wave components, we can rewrite (1) in 3D Fourier transform form [13]

$$\begin{aligned}
f(x', y', \omega) &= \\
&\iint \left[\iiint s(x, y, z) e^{-j(k_{x'}x + k_{y'}y + k_z z)} dx dy dz \right] \\
&\quad \times e^{j(k_{x'}x' + k_{y'}y' + k_z z_0)} dk_{x'} dk_{y'}
\end{aligned} \tag{2}$$

where $k_{x'}$ and $k_{y'}$ are Fourier transform variables corresponding to x' and y' , respectively, and the one corresponding to z is $k_z = \sqrt{4k^2 - k_x^2 - k_y^2}$. The triple integral in (2) is the 3D Fourier transform of $s(x, y, z)$. Solving this equation and dropping the distinction between primed and unprimed coordinates, the 3D image is formed by [13]

$$s(x, y, z) = \mathcal{F}_{3D}^{-1} \left\{ \mathcal{F}_{2D} \{f(x, y, \omega)\} e^{-j\sqrt{4k^2 - k_x^2 - k_y^2} z_0} \right\} \tag{3}$$

where $\mathcal{F}\{.\}$ and $\mathcal{F}^{-1}\{.\}$ are the Fourier and inverse Fourier transform operators, respectively. Since in (3) the frequencies are uniformly sampled in the frequency band and the probe scans at uniform step size along X-Y dimensions, k_z 's are nonuniformly distributed and Stolt interpolation is normally used to interpolate the uniform points in k_z [20]. It has been shown that NUFFT can be exploited to improve the accuracy of SAR imaging [8] since it is a good approximation of the nonuniform discrete Fourier transform (NDFT) [23, 38]. Using NUFFT, (3) becomes

$$\begin{aligned}
s(x, y, z) &= \\
&\mathcal{F}_{2D}^{-1} \left\{ \mathcal{F}_{NU}^{-1} \left\{ \mathcal{F}_{2D} \{f(x, y, \omega)\} e^{-j\sqrt{4k^2 - k_x^2 - k_y^2} z_0} \right\} \right\}
\end{aligned} \tag{4}$$

where $\mathcal{F}_{NU}^{-1}\{.\}$ is one dimensional inverse NUFFT operator in the k_z domain.

Now, consider the case where spatial and frequency samples are nonequispaced and randomly distributed. The two dimensional Fourier transform in (4) is no longer applied to uniform X-Y grids. Assuming that we know the sample locations, we can

use the two dimensional NUFFT as an accurate approximation to the two dimensional NDFT. This is also known as an unbiased spectrum estimator with uniform weights [53]. Therefore, (4) becomes

$$s(x, y, z) = \mathcal{F}_{2D}^{-1} \left\{ \mathcal{F}_{NU}^{-1} \left\{ \mathcal{F}_{2DNU} \{f(x, y, \omega)\} e^{-j\sqrt{4k^2 - k_x^2 - k_y^2} z_0} \right\} \right\} \quad (5)$$

where $\mathcal{F}_{2DNU} \{.\}$ is the two dimensional NUFFT operator applied along X-Y dimensions.

3. DATA RECOVERY USING CS

Let us consider a complex valued column vector $\mathbf{f} \in \mathbb{C}^N$ containing all reflection coefficients $f(x, y, \omega)$ where N is the number of measured reflection coefficients. This vector expands in an orthonormal basis of $N \times 1$ vectors, $\{\boldsymbol{\psi}_i\}_{i=1}^N$, that forms $N \times N$ dictionary matrix, $\boldsymbol{\Psi} = [\boldsymbol{\psi}_1 \boldsymbol{\psi}_2 \dots \boldsymbol{\psi}_N]$. The signal can then be expressed as $\mathbf{f} = \boldsymbol{\Psi} \mathbf{c}$, where \mathbf{c} is the vector of atoms, $c_i = \langle \mathbf{f}, \boldsymbol{\psi}_i \rangle = \boldsymbol{\psi}_i^H \mathbf{f}$, with $(.)^H$ denoting conjugate transpose. The signal \mathbf{f} is called *S-sparse* if it can be represented with only S significant c_i coefficients. Our experiments show that three dimensional discrete cosine transform (DCT) applied on 3D matrix of reflection coefficients sparsifies the signal very well and is a very good candidate to be used in CS.

Random samples of \mathbf{f} are chosen using the measurement matrix, $\boldsymbol{\Phi}$, of size $M \times N$ with $M < N$. The undersampled vector, \mathbf{y} , can be expressed in matrix format $\mathbf{y} = \boldsymbol{\Phi} \mathbf{f} = \boldsymbol{\Phi} \boldsymbol{\Psi} \mathbf{c}$. This equation for solving \mathbf{f} is ill-conditioned in general and does not have a unique solution. However, if the matrix $A = \boldsymbol{\Phi} \boldsymbol{\Psi}$ obeys *restricted isometry property* (RIP), we can recover the signal, \mathbf{f} , with high probability using $M \geq KS \log(N/S)$ measurements for some constant K [17]. To make hardware

implementation feasible and satisfy the RIP for matrix A , we choose Φ a matrix of spikes by randomly placing a one in each row of the matrix such that the matrix selects samples at the corresponding (x, y) locations. For each selected location, the matrix samples frequency point from a full set of swept frequencies. To reconstruct high resolution images from the incomplete samples, \mathbf{y} , we use the standard Basis Pursuit (BP) method [19]

$$\min_{\tilde{\mathbf{c}} \in \mathbb{C}^N} \|\tilde{\mathbf{c}}\|_1 \quad \text{subject to} \quad \mathbf{y} = \Phi \Psi \tilde{\mathbf{c}} \quad (6)$$

where $\|\cdot\|_1$ is the ℓ_1 norm operator and $\tilde{\mathbf{c}}$ is the estimate of \mathbf{c} . After recovering the full set of reflection coefficients, we use (4) to reconstruct the 3D image.

4. EXPERIMENTAL TESTS AND RESULTS

Wideband SAR experiments were conducted at the Applied Microwave Non-destructive Testing Laboratory (*amntl*) at the Electrical and Computer Engineering Department of the Missouri University of Science and Technology (Missouri S&T). A sample was prepared with eight rubber (Rbr) patches of different sizes and one copper (Cu) patch. As shown in Fig. 1, the targets were fixed on a substrate at different heights using pieces of construction foam as physical support. The microwave imaging antenna probe was an open-ended waveguide located at 30 mm above the highest target along Z direction. Since the substrate was located at 106 mm below the probe (maximum range), frequency step size of at most $\Delta f = c/(4R_{max}) = 0.7$ GHz was needed to image the whole range [13]. In our experiments, the swept frequency imaging system operated at K-band (18–26.5 GHz) with frequency step size of 0.6 GHz. An area of 120 mm \times 140 mm of the SUT was raster scanned using spatial step sizes of 2 mm in both X and Y directions and the reflections were received by

the same antenna probe. The baseband complex-valued raw data were measured and recorded by an HP 8510C vector network analyzer. Having a complete set of raw data, several incomplete sample sets were chosen using uniform random sampling. Then NUFFT SAR and CS were applied separately to produce the SAR images of the SUT.

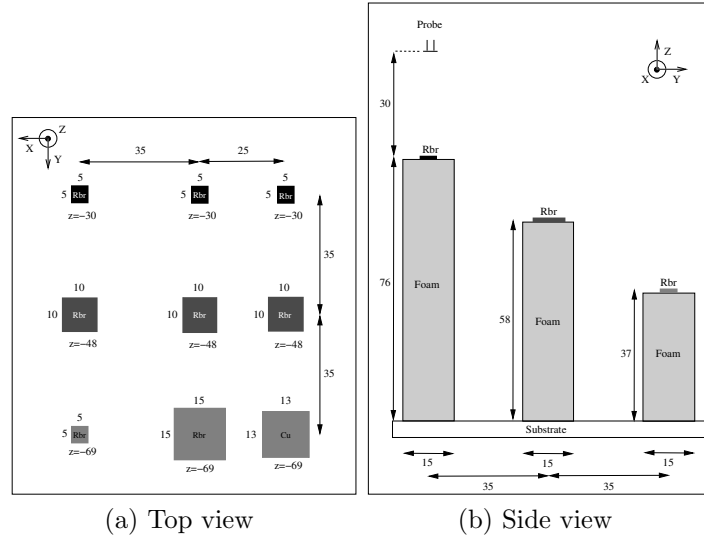


Figure 1: Schematic of scanned area of SUT, where unit in figure is mm.

To evaluate the performance of each method, four different quantitative metrics are used on the reconstructed SAR image. The first metric is the normalized root mean square (RMS) error that is the normalized Euclidean distance between the full data set image and the estimated one

$$\varepsilon = \frac{\|\mathbf{s} - \tilde{\mathbf{s}}\|}{\|\mathbf{s}\|} \quad (7)$$

where $\|\cdot\|$ is the ℓ_2 norm operator, \mathbf{s} is the vectorized image of full data set, and $\tilde{\mathbf{s}}$ is the vectorized estimated image of incomplete data set. The second, third, and fourth

metrics each quantify the SAR image from incomplete data in comparison to itself in terms of two types of contrast and signal-to-noise ratio (SNR). The contrast definitions used are Weber contrast and root mean square (RMS) contrast. Weber contrast is usually used in cases where small targets are presented on a wide uniform background

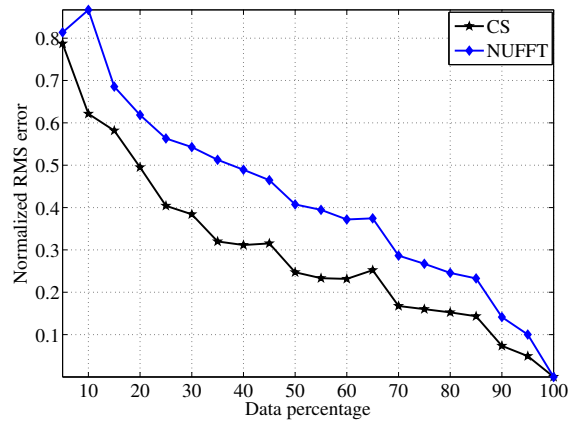


Figure 2: Normalized RMS error for 3D images reconstructed from experimental data using CS and NUFFT.

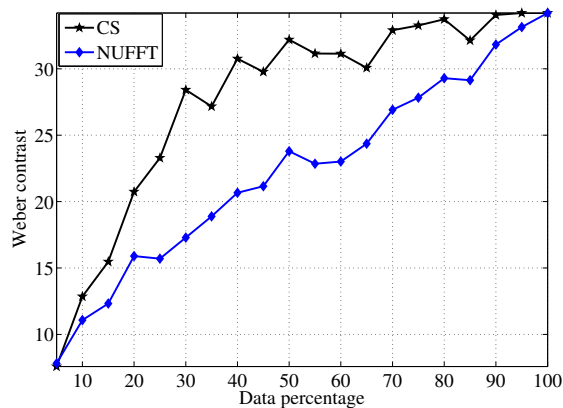


Figure 3: Weber contrast of 3D images reconstructed from experimental data using CS and NUFFT.

and is defined as the normalized difference between target and background intensity

$$C_w = \frac{|s_t - s_b|}{s_b} \quad (8)$$

where s_t is the target intensity and s_b is the plain background intensity [29]. On the other hand, RMS contrast does not use the spatial distribution of contrast since it is

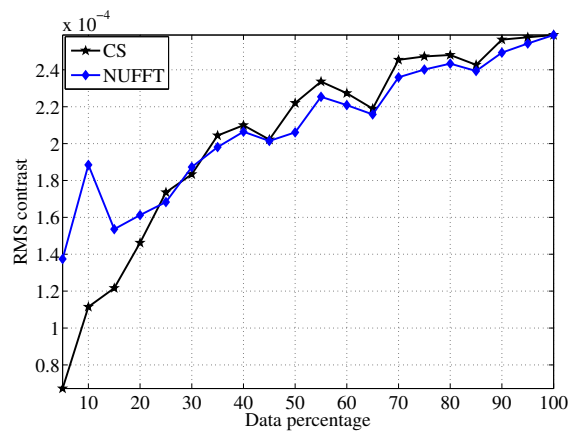


Figure 4: RMS contrast of 3D images reconstructed from experimental data using CS and NUFFT.

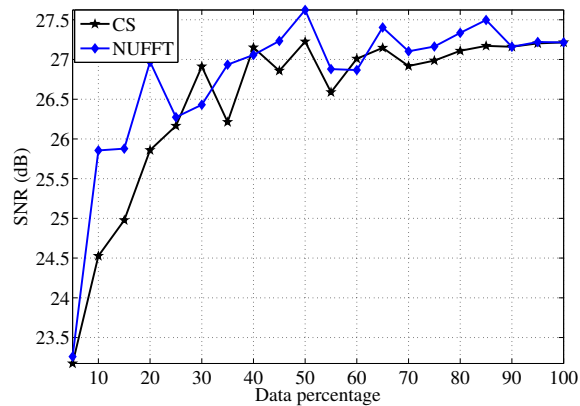


Figure 5: SNR of 3D images reconstructed from experimental data using CS and NUFFT.

defined as the standard deviation of voxels intensity

$$C_{rms} = \left[\frac{1}{n-1} \sum_{i=1}^n (s_i - \bar{s}) \right]^{1/2} \quad (9)$$

where s_i is the intensity of each voxel, \bar{s} is the mean of voxels intensity, and n is the number of voxels. SNR is the last metric utilized. It is defined as the ratio of target intensity to background noise intensity in dB

$$SNR = 20 \log_{10} \left(\frac{s_{max} - s_{min}}{\sigma_s} \right) \quad (10)$$

where σ_s is the standard deviation of the image.

Figure 2 illustrates the RMS error for different percentages of data selected from the full data set. It can be seen that CS have performed better than NUFFT SAR in terms of error. The Weber contrast of the generated images for different percentages of raw data is shown in Fig. 3. It can be seen that Weber contrast is a good figure of merit to quantify the sparsity in images. CS resulted in higher contrast images and targets are more distinguishable as compared to NUFFT SAR. Figure 4 shows RMS contrast for the same data set. Since RMS contrast is defined globally, CS and NUFFT SAR have almost the same performance especially in higher percentages. The SNR of images from NUFFT SAR and CS for different percentages of incomplete data is shown in Fig. 5. The two algorithms have almost the same performance in terms of SNR.

The two approaches are also compared in terms of computational complexity and time required to estimate the image. To solve the optimization problem in (5), we used Alternating Direction Method (ADM) recently proposed in [28] and provided by the YALL1 Matlab package. Because of its iterative nature, CS is more computationally intensive and it took about 100 seconds to converge while NUFFT SAR uses the fast

Fourier transform and can be computed in fraction of a second using a Dell Optiplex 760 with an Intel Core 2 Duo 3.33 GHz CPU.

To compare the two methods qualitatively, volumetric images of the SUT are plotted and compared to the image of the full data set. Figure 6 shows the 3D images of the targets from the original and incomplete data sets using CS and NUFFT SAR with different percentages of spatial and frequency points. It can be seen for images from 30% (40% X-Y and 75% frequency points) and 24.5% (35% X-Y and 70% frequency points) of data that all targets are distinguishable in images recovered using CS while the small rubber target at $z = -69$ mm can not be easily seen in NUFFT SAR images because of background artifacts added to the image. Both methods fail to detect this small rubber pads for 10% (18% X-Y and 56% frequency points) of data.

To see the details of each figure, slices of the 3D image are also shown. Figure 7 illustrates slices of SAR image from full data set. It shows slices from three different levels of targets and one slice from substrate level which has very low signal power. Figures 8 and 9 show slices of images produced from different percentages of raw data using CS and NUFFT SAR respectively. From the slices it can be seen that NUFFT have added more artifacts to the image especially at $z = -30$ mm.

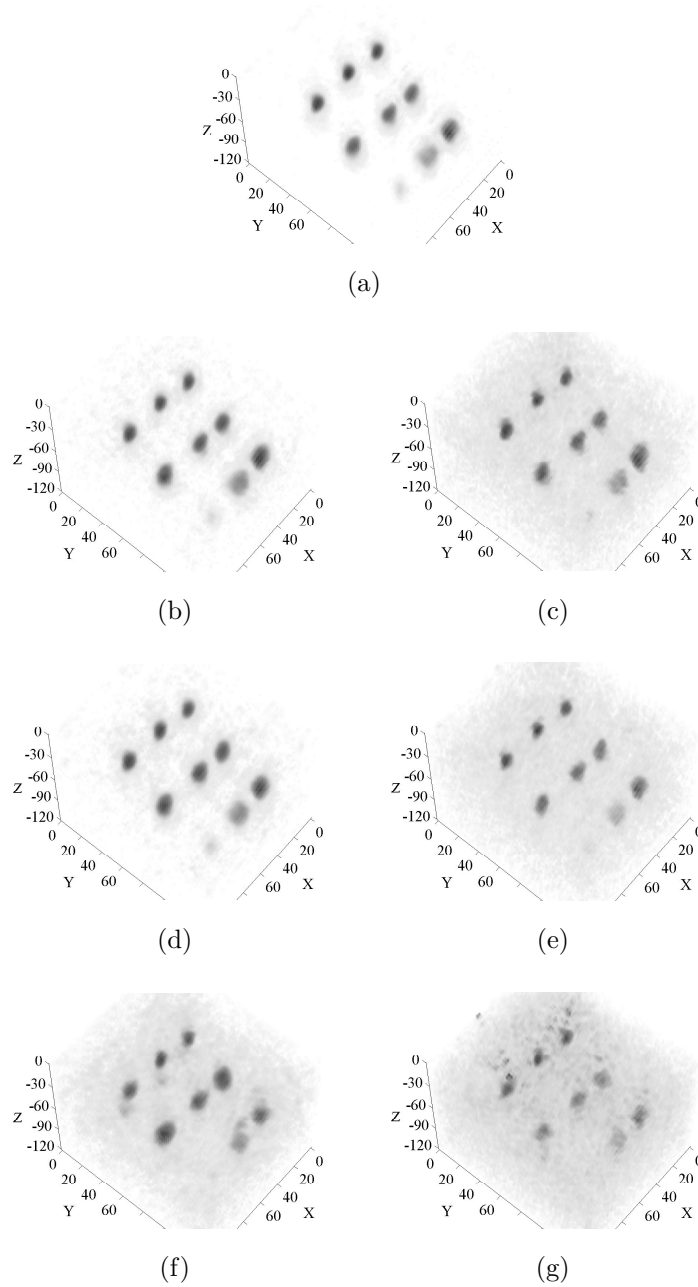


Figure 6: Wideband SAR images of (a) full data set, (b) 30% of data using CS, (c) 30% of data using NUFFT (d) 24.5% of data using CS, (e) 24.5% of data using NUFFT, (f) 10% of data using CS, and 10% of data using NUFFT (unit in figure is mm).

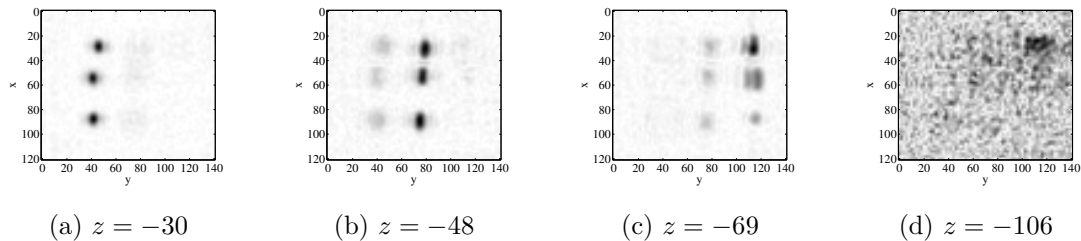


Figure 7: Slices of wideband SAR images of full data set (unit in the figure is mm).

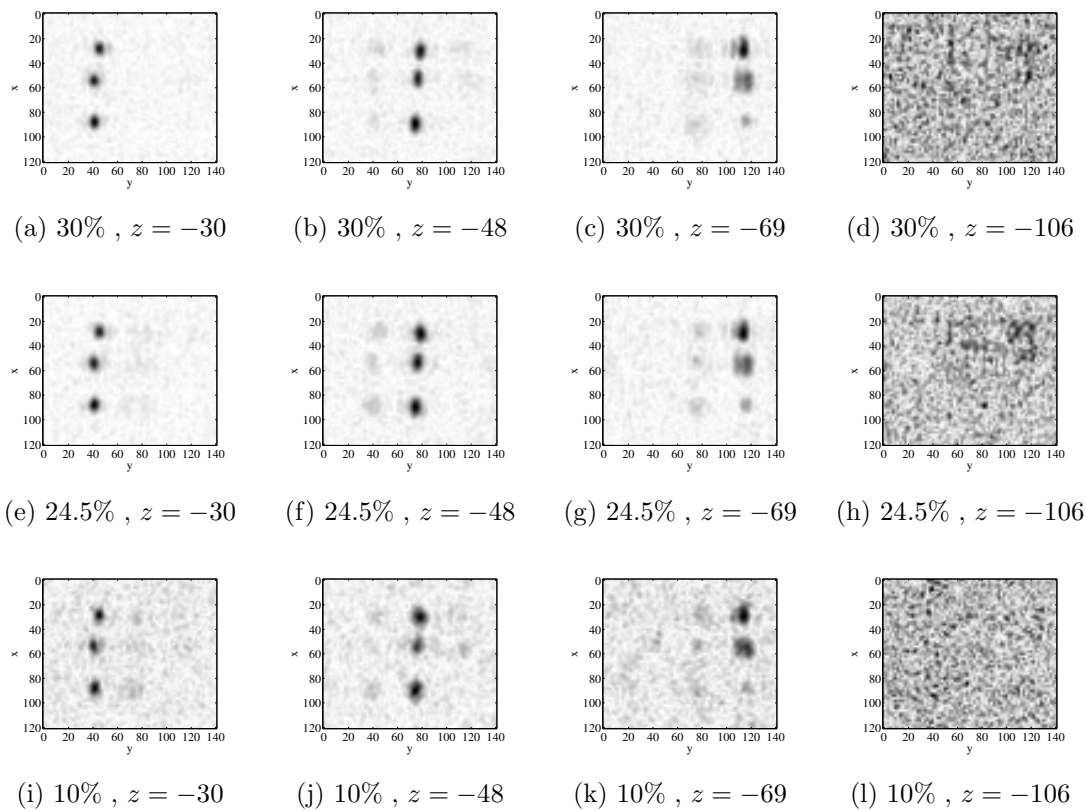


Figure 8: Slices of wideband SAR images from incomplete data using CS (unit in the figure is mm).

5. CONCLUSION

CS and NUFFT SAR are both capable of forming SAR images from an incomplete set of data. Quantitative and qualitative metrics show that CS performs better than NUFFT SAR for the same set of data and causes fewer artifacts during data recovery.

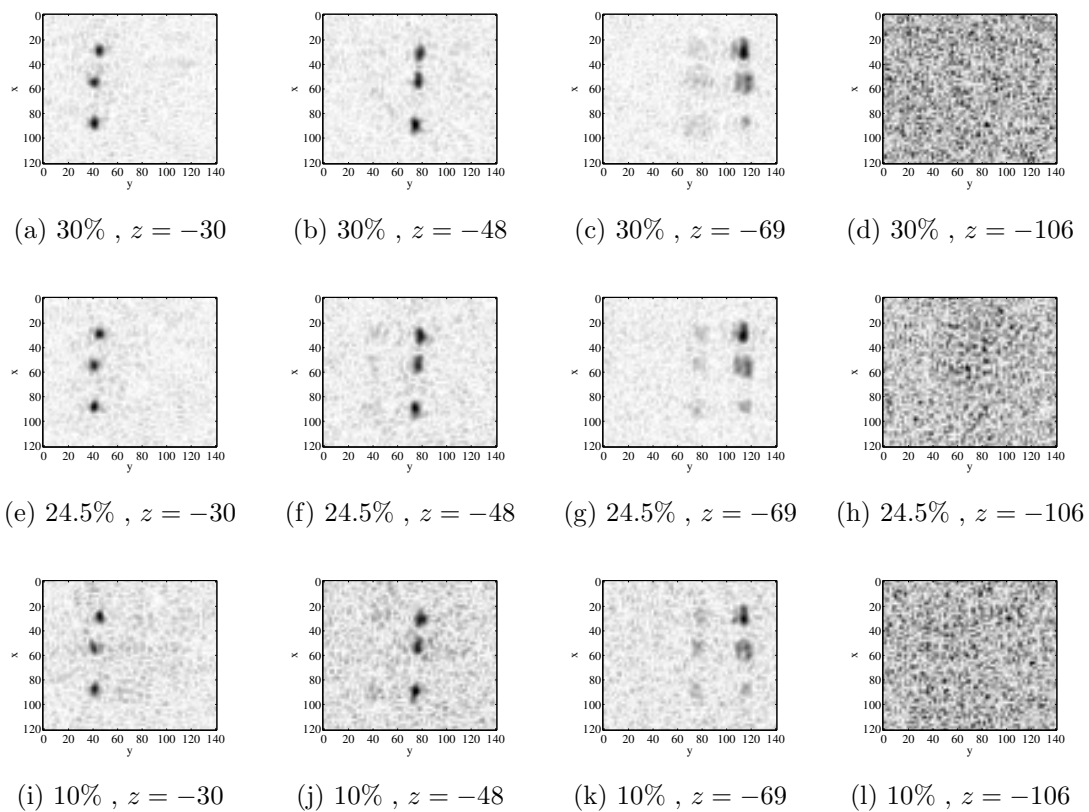


Figure 9: Slices of wideband SAR images from incomplete data using NUFFT SAR (unit in the figure is mm).

In terms of computational complexity, NUFFT SAR have much better performance than CS and is more suitable for real-time applications.

V. 3D IMAGE RECONSTRUCTION FROM SPARSE MEASUREMENT OF WIDEBAND MILLIMETER WAVE SAR EXPERIMENTS

Hamed Kajbaf, Joseph T. Case, and Yahong Rosa Zheng

ABSTRACT—Nonuniform random sampling is applied to a wideband 3D synthetic aperture radar (SAR) imaging system to reduce the number of measurement points in both frequency and space domains. Experimental tests were performed on a construction foam specimen using uniformly sampled Q-band frequencies in 35.04 GHz to 44.96 GHz and at a grid of two millimeter step sizes. Using discrete Fourier transform (DFT) or discrete cosine transform (DCT) sparse representations, the 3D images can be reconstructed from 7% random samples of the experimental data achieving comparable quality as the one from original full-set data. This can translate to significant time reduction of measurement from more than one hour to less than 20 minutes.

1. INTRODUCTION

Microwave and millimeter wave imaging are effective nondestructive testing and evaluation (NDT&E) methods that have found important applications in testing critical structures such as spacecraft tiles, airplane coating, bonding of adhesive or composite materials, etc [1]. Using synthetic aperture radar (SAR) technology, the wideband 3D SAR imaging system developed at the Missouri University of Science and Technology (Missouri S&T) is capable of detecting tiny defects of millimeter sizes embedded within the specimen under test (SUT) without compromising the usefulness and utility of the SUT [7]. However, using the conventional sampling method in both space and frequency domains, the imaging system currently suffers from slow sensing

speed due to slow sweeping oscillators available in current microwave technology as well as small step sizes needed for spatial resolution.

The emerging compressed sensing (CS) methodology [14, 17] provides a great potential for solving this problem. In this paper, we successfully develop the CS method for reconstruction of wideband 3D images from as low as 7% of the measurement samples required by Nyquist sampling rate. Experimental results have been obtained using nonuniform random sampling [17, 36] with discrete Fourier transform (DFT) and discrete cosine transform (DCT) as the sparsifying domain. The reconstructed 3D images achieve similar quality as that of conventional method using the full-set data. This work distinguishes itself from existing CS research on radar applications in that we deal with wideband 3D SAR rather than narrowband synthetic 3D imaging such as the ones in [18, 27, 54, 55]. This allows us to reduce the number of measured frequency points in addition to reducing the number of spatial points.

2. WIDEBAND MONOSTATIC SAR IMAGING

A typical configuration of a wideband 3D SAR imaging system is shown in Fig. 1. The antenna probe located at (x', y', z_0) transmits a short pulse, $Re\{p(t)e^{j\omega t}\}$, onto the SUT with a wide aperture antenna, where t is the time and ω is the temporal angular frequency. A point on the target at (x, y, z) reflects back the pulse and the probe receives an echo with round trip phase delay. The demodulated baseband echo is then $p(t - \frac{2R}{c})e^{j\omega\frac{2R}{c}}$, where c is the propagation speed and R is the range between the probe and the target point $R = \sqrt{(x - x')^2 + (y - y')^2 + (z - z_0)^2}$.

The complex signal received at the probe, $f(x', y', \omega)$, is the superposition of back-scattered pulses from all points of the target within the aperture [13]

$$f(x', y', \omega) = \iiint s(x, y, z)e^{-jkR} dx dy dz \quad (1)$$

where $k = \frac{\omega}{c}$ is the wavenumber and $s(x, y, z)$ is the reflectivity function of the target, which is the ratio of the reflected field to the incident field. Decomposing the spherical wave propagation into a superposition of plane wave components, we can rewrite (1) in 3D Fourier transform form [13]

$$f(x', y', \omega) = \iint \left[\iiint s(x, y, z) e^{-j(k_{x'}x + k_{y'}y + k_z z)} dx dy dz \right] \times e^{j(k_{x'}x' + k_{y'}y' + k_z z_0)} dk_{x'} dk_{y'} \quad (2)$$

where $k_{x'}$ and $k_{y'}$ are Fourier transform variables corresponding to x' and y' , respectively, and the one corresponding to z is $k_z = \sqrt{4k^2 - k_x^2 - k_y^2}$. The triple integral in (2) is the 3D Fourier transform of $s(x, y, z)$. Solving this equation and dropping the distinction between primed and unprimed coordinates and benefiting from wideband measurement, the 3D image is formed by [13]

$$s(x, y, z) = \mathcal{F}_{3D}^{-1} \left\{ \mathcal{F}_{2D} \{ f(x, y, \omega) \} e^{-j\sqrt{4k^2 - k_x^2 - k_y^2} z_0} \right\} \quad (3)$$

where $\mathcal{F}\{\cdot\}$ and $\mathcal{F}^{-1}\{\cdot\}$ are the Fourier and inverse Fourier transform operators, respectively.

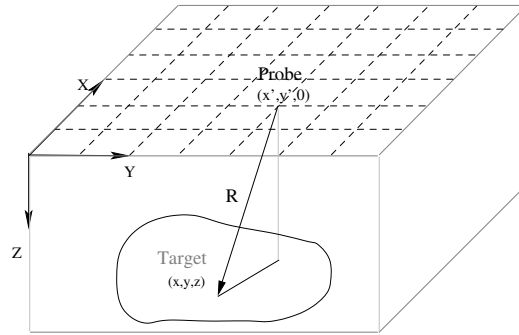


Figure 1: Schematic of imaging system setup configuration.

In (3), the frequencies are uniformly sampled in the frequency band and the probe scans at uniform step size along X-Y dimensions, hence, uniform k , k_x , and k_y . Consequently, the k_z 's are nonuniformly distributed and Stolt interpolation is usually used to interpolate the uniform points in k_z . Alternatively, it has been shown that the nonuniform fast Fourier transform (NUFFT) improves the performance and accuracy of SAR imaging since it is a good approximation of the nonuniform discrete Fourier transform (NDFT) [24]. Using NUFFT, (3) becomes

$$s(x, y, z) = \mathcal{F}_{2D}^{-1} \left\{ \mathcal{F}_{NU}^{-1} \left\{ \mathcal{F}_{2D} \{f(x, y, \omega)\} e^{-j\sqrt{4k^2 - k_x^2 - k_y^2} z_0} \right\} \right\} \quad (4)$$

where $\mathcal{F}_{NU}^{-1} \{.\}$ is one dimensional inverse NUFFT operator in the k_z domain.

3. APPLICATION OF CS TO WIDEBAND SAR

To develop CS method for the wideband SAR imaging system, we first formulate the uniformly sampled reflection coefficients $f(x, y, \omega)$ into a $N \times 1$ column vector \mathbf{f} . Assuming this vector expands in an orthonormal basis of $N \times 1$ vectors $\{\boldsymbol{\psi}_i\}_{i=1}^N$, we form an $N \times N$ dictionary matrix $\boldsymbol{\Psi} = [\boldsymbol{\psi}_1 \boldsymbol{\psi}_2 \dots \boldsymbol{\psi}_N]$ and express the signal as $\mathbf{f} = \boldsymbol{\Psi} \mathbf{c}$, where \mathbf{c} is the vector of atoms $c_i = \langle \mathbf{f}, \boldsymbol{\psi}_i \rangle = \boldsymbol{\psi}_i^H \mathbf{f}$ with $(.)^H$ denoting conjugate transpose (Hermitian). The signal \mathbf{f} is called *S-sparse* if only S of its c_i coefficients are significant and the rest of $(N - S)$ coefficients are zero or close to zero. In practice, we can use DFT, DCT, wavelet, and other dictionaries as matrix $\boldsymbol{\Psi}$ to represent the data.

Then we choose a random measurement matrix, $\boldsymbol{\Phi}$, of size $M \times N$ with $M < N$ to undersample the signal \mathbf{f} and obtain the compressed measurement $\mathbf{y} = \boldsymbol{\Phi} \mathbf{f} = \boldsymbol{\Phi} \boldsymbol{\Psi} \mathbf{c}$. To ease the hardware implementation, we choose uniformly distributed random (x, y)

locations and set the corresponding coefficient of Φ to one. Other coefficients of Φ are set to zero. For each selected (x, y) location, a set of frequency points are also selected randomly from the full-set of swept frequencies.

To reconstruct high resolution images from the incomplete samples, \mathbf{y} , we use the standard Basis Pursuit (BP) method [19]

$$\min_{\tilde{\mathbf{c}} \in \mathbb{C}^N} \|\tilde{\mathbf{c}}\|_1 \quad \text{subject to} \quad \mathbf{y} = \Phi \Psi \tilde{\mathbf{c}} \quad (5)$$

where $\tilde{\mathbf{c}}$ is the estimate of \mathbf{c} . Consequently, the high resolution signal \mathbf{f} can be recovered, and the 3D image is reconstructed using (4).

4. EXPERIMENTAL TESTS AND RESULTS

The wideband SAR experiments were conducted by the Applied Microwave Non-destructive Testing Laboratory (amntl) at the Electrical and Computer Engineering Department of the Missouri University of Science and Technology. The SUT was a cubic blue foam of size $120 \times 180 \times 80 \text{ mm}^3$ supported on a wooden frame with two thin metal strips. The SUT was made from three layers of construction foam. The layers of foam were taped together and each layer had three round rubber pads (defects) of 5 mm diameter and 2 mm height embedded at different locations, as shown in Fig. 2. The millimeter wave imaging probe was located 34 mm above the SUT (standoff distance). The imaging system operated with 125 uniformly swept frequencies in the Q-band (35.04 – 44.96 GHz) and with a spatial step size of 2 mm in the X and Y dimensions. The reflected backscatters were received by the same antenna probe and a matched filter receiver. The baseband complex-valued raw data were recorded by a vector network analyzer. Other details of the experiment are found in [7].

To apply CS method for image reconstruction, an undersampled data set was chosen from the acquired raw data with 35% of points randomly selected in the X-Y plane. For each spatial location, 20% frequency points from the full data set were randomly selected. This resulted in 7% of the data used in image reconstruction which could reduce the measurement time from more than an hour to less than 20 minutes.

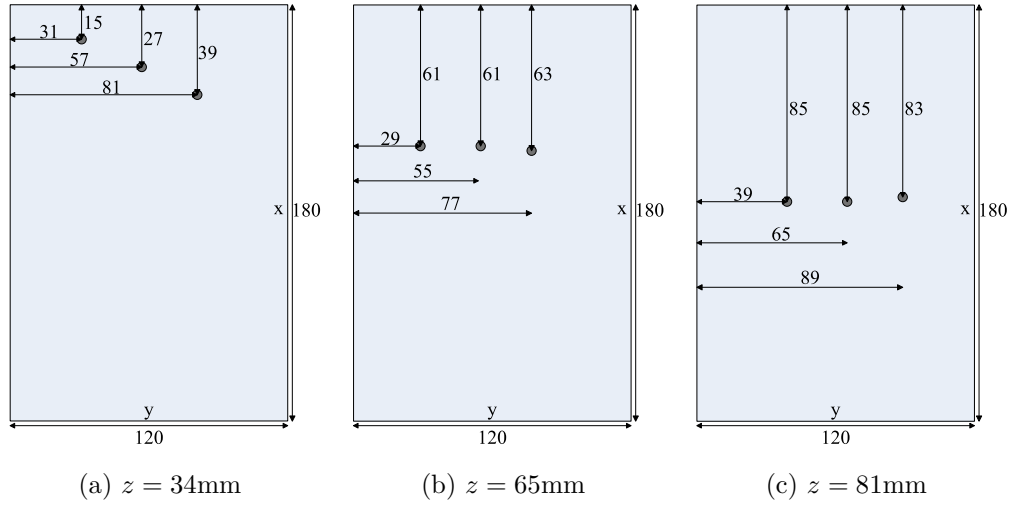


Figure 2: Locations of the rubber pads in the scanned area of SUT, where unit in figure is mm, and z is the distance from the SAR probe.

The optimization problem in (5) was solved using the Alternating Direction Method (ADM) recently proposed in [28] and provided by the YALL1 Matlab package, thanks to its capability of handling complex coefficients. We tried several transform domains (matrix Ψ), such as the DFT, DCT, wavelet, SAR transform (the image domain), etc. We found that the DCT domain provided the best performance and convergence with the experimental data.

The CS reconstructed 3D image achieved similar quality as the one from the original full-set raw data. The reconstructed volumetric images from the DFT CS and

DCT CS methods were compared to the one from the original full data set, as shown in Fig. 3. The nine defects in three different layers were clearly shown in all images, while the DFT CS method produced two strips on the boundary of the aperture at depth $z = 0$ mm. Alternatively, Fig. 4 illustrates slices of the reconstructed 3D SAR images at different heights from the probe. The defects on all three layers were clearly identified by both DFT and DCT domain methods, even though some artifacts in the lower layer ($z = 81$ mm) were presented in all three images from the original, DFT CS, and DCT CS methods. The images at $z = 120$ mm height shows the bottom supporting material.

The performance of DCT was better in terms of root mean square (RMS) error of the estimates, as shown in Fig. 5. When different percentages of data were used, the DCT CS achieved less reconstruction error than the DFT CS method, especially at low percentages. Also, the algorithm converged faster in DCT domain as shown in Fig. 6 since the reflection coefficients were sparser in this domain.

Despite the good performance of CS reconstruction using 2D SAR as sparse representation, reconstruction failed to converge for wideband 3D SAR representation (sparse domain). The reason was due to truncation errors occurring in each iteration

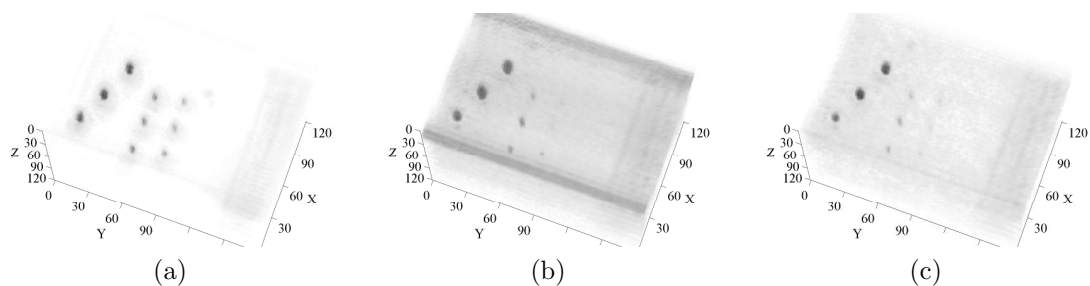


Figure 3: Wideband SAR images of (a) full data set, (b) 7% of data using DFT sparse representation, and (c) 7% of data using DCT sparse representation. Unit in the figure is mm.

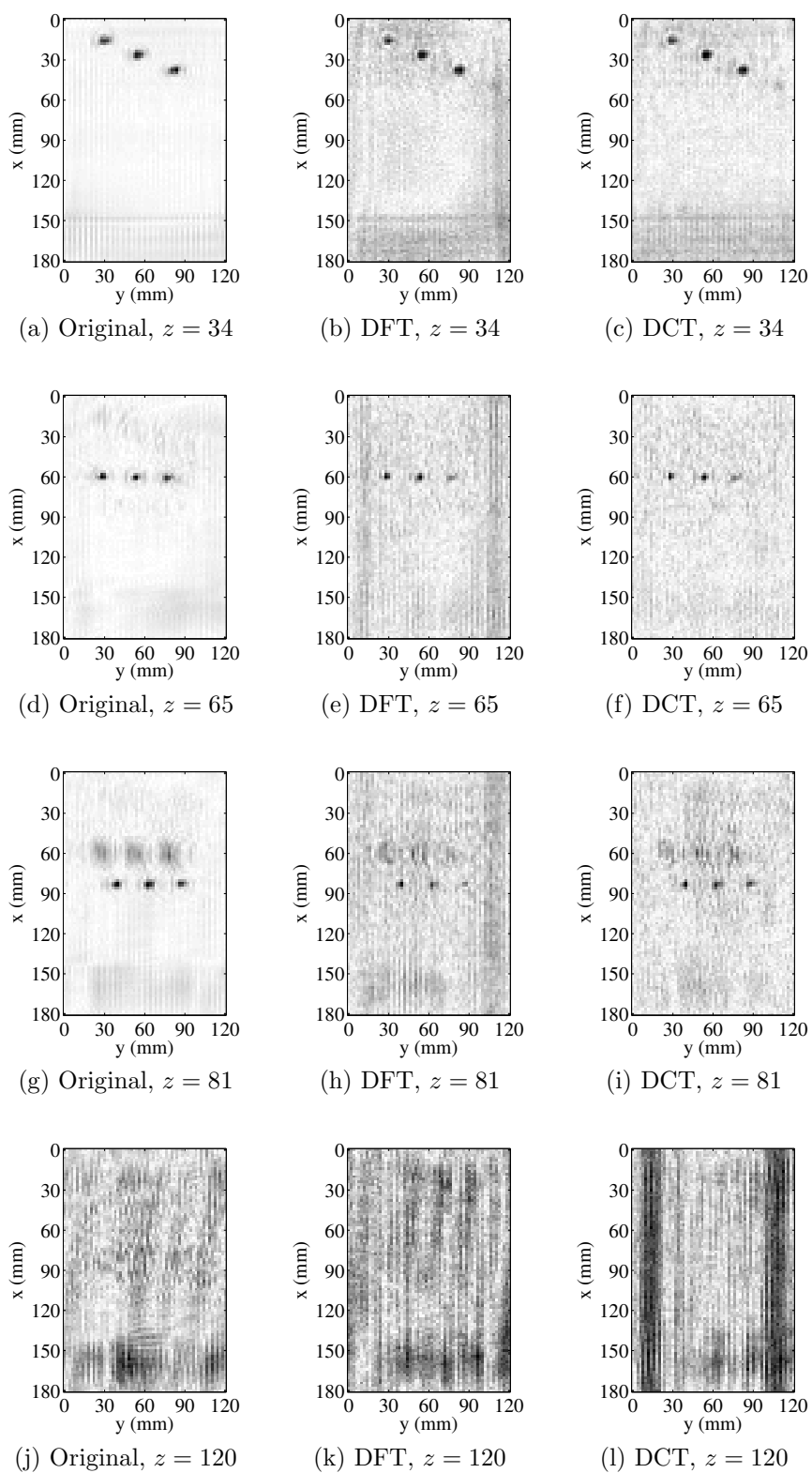


Figure 4: Slices of reconstructed wideband SAR images using measured data as in Fig. 3. Unit in the figure is mm.

of solving (5). In the future, we are going to correct this truncation error and use 3D SAR sparse representation to decrease the acquisition time.

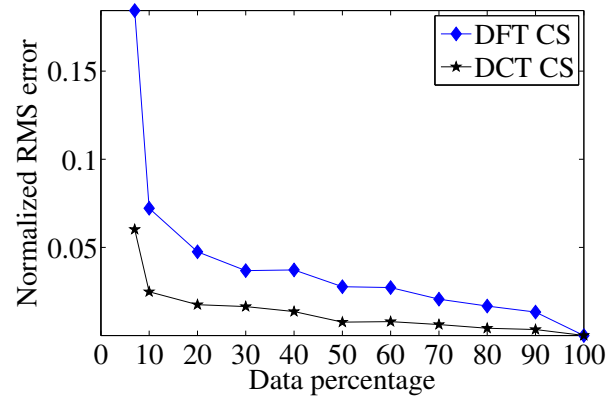


Figure 5: Normalized RMS error for 3D images reconstructed by the DFT and DCT CS methods.

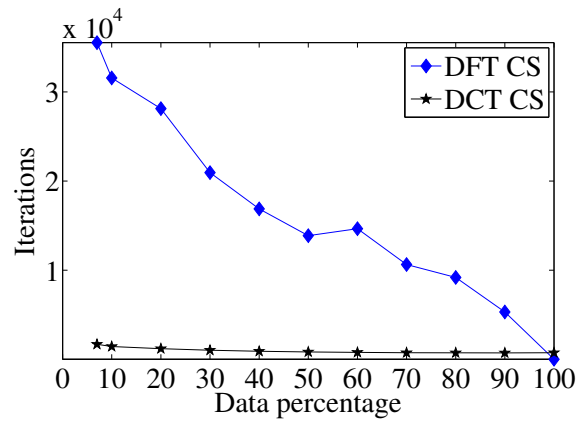


Figure 6: Number of iterations for 3D images reconstructed by the DFT and DCT CS methods.

5. CONCLUSION

The random sampling method has been successfully applied to a wideband 3D SAR imaging system to reduce the number of measurement samples to 7% of the full-set, thus in turn reducing the measurement time significantly. The Basis Pursuit method has been used with DFT and DCT as the sparsifying domain to reconstruct volumetric images from the undersampled measurements. Experimental results demonstrated that both discrete Fourier transform and discrete cosine transform achieve low estimation error and fast convergence, while 3D SAR sparse representation failed to converge for 3D images.

6. ACKNOWLEDGMENT

We wish to thank Drs. Sergey Kharkovsky and Reza Zoughi for providing the blue foam experiment data.

SECTION

2. CONCLUSIONS

In this dissertation, the compressed sensing (CS) methodology is applied to a 3D SAR imaging system. Several sets of experiments are performed on different specimens to evaluate the performance of the proposed CS algorithms.

The results of experimental tests indicate that compressed sensing can be successfully applied to 2D and 3D microwave SAR imaging for nondestructive testing applications. Using the proposed methods, the acquisition time is significantly reduced and the computational complexity of the post-processing is kept low while the images are produced with comparable quality. The results of our experiments indicate that one can reduce the acquisition time by up to 66% of that of conventional methods while maintaining the quality of the SAR images by randomly selecting 20% of spatial points.

CS and NUFFT SAR are both capable of forming SAR images from an incomplete set of data. Both quantitative and qualitative metrics show that CS performs better than NUFFT SAR for the same set of data and causes fewer artifacts during data recovery. In terms of computational complexity, NUFFT SAR demonstrated a much better performance than did CS and is more suitable for real-time applications.

We propose a new 3D image reconstruction method for compressed sensing microwave imaging using NUFFT-based SAR. High quality SAR images are recovered from incomplete measurements by exploiting an accurate SAR and R-SAR transform pair allowing the forward and reverse SAR to be applied in each iteration of CS and ensuring the convergence of the CS algorithm. A new, low-complexity truncation repair method is also proposed to reduce the truncation error in the practical application of the NUFFT algorithm in the reverse SAR transform. It is shown that the

proposed model recovers the sparse targets very well and, at the same time, removes the background artifacts better than the conventional full-set measurement approach.

Finally, we propose a low-computationally-complex algorithm called adaptive basis selection (ABS) compressed sensing to recover images from incomplete measurement without any knowledge of the proper sparse representation. To detect the best basis from a set of bases, a decision metric is introduced to select between the bases as the signal is evolved during the iterations of the algorithm. The 2D synthetic aperture radar images and the Shepp-Logan phantom data were used to show the performance of the proposed method. The results of our experiments indicate that the proposed algorithm successfully selected the best basis adaptively and was capable of recovering the images with high accuracy.

3. PUBLICATIONS

- [1] H. Kajbaf, J.T. Case, Y.R. Zheng, S. Kharkovsky, and R. Zoughi, “Quantitative and qualitative comparison of SAR images from incomplete measurements using compressed sensing and nonuniform FFT,” in *Proc. 2011 IEEE Radar Conf. (RADAR)*, Kansas City, MO, May 2011, pp. 592–596.
- [2] H. Kajbaf, J.T. Case, and Y.R. Zheng, “3D image reconstruction from sparse measurement of wideband millimeter wave SAR experiments,” in *Proc. of the 18th IEEE Int. Conf. on Image Process. (IEEE ICIP 2011)*, Brussels, Belgium, Sep. 2011, pp. 2701–2704.
- [3] H. Kajbaf, Y.R. Zheng, and R. Zoughi, “Improving efficiency of microwave imaging systems using compressive sensing technology,” *Materials Evaluation*, accepted for publication.
- [4] H. Kajbaf, J.T. Case, Z. Yang, and Y.R. Zheng, “Compressed sensing for SAR-based wideband 3D microwave imaging system using nonuniform FFT,” *IET Radar, Sonar, and Navigation*, to be published.
- [5] H. Kajbaf and Y.R. Zheng, “Adaptive basis selection compressed sensing,” *IEEE Trans. Instrum. Meas.*, to be submitted.

BIBLIOGRAPHY

- [1] S. Kharkovsky and R. Zoughi, "Microwave and millimeter wave nondestructive testing and evaluation – overview and recent advances," *IEEE Instrum. Meas. Mag.*, vol. 10, no. 2, pp. 26–38, Apr. 2007.
- [2] R. Zoughi, *Microwave Non-Destructive Testing and Evaluation*. the Netherlands: Kluwer Academic Publishers, 2000.
- [3] L. P. Song, C. Yu, and Q. H. Liu, "Through-wall imaging (TWI) by radar: 2-D tomographic results and analyses," *IEEE Trans. Geosci. Remote Sens.*, vol. 43, no. 12, pp. 2793–2798, Dec. 2005.
- [4] J. T. Case, S. Kharkovsky, R. Zoughi, and F. Hepburn, "High resolution millimeter wave inspecting of the orbiter acreage heat tiles of the space shuttle," in *Proc. IEEE Instrumentation and Measurement Technology Conf. (IMTC 2007)*, Warsaw, Poland, May 2007, pp. 1–4.
- [5] J. T. Case, S. Kharkovsky, R. Zoughi, G. Steffes, and F. L. Hepburn, "Millimeter wave holographical inspection of honeycomb composites," in *Review of Progress in Quantitative Nondestructive Evaluation Vol. 27B, AIP Conference Proceedings*, D. O. Thompson and D. E. Chimenti, Eds., vol. 975. Melville, NY: American Institute of Physics, Feb. 2008, pp. 970–975.
- [6] S. Hantscher, A. Reizenzahn, and C. Diskus, "Through-wall imaging with a 3-D UWB SAR algorithm," *IEEE Signal Process. Lett.*, vol. 15, pp. 269–272, 2008.
- [7] M. T. Ghasr, D. Pommerenke, J. T. Case, A. McClanahan, A. Aflaki-Beni, M. Abou-Khousa, S. Kharkovsky, K. Guinn, F. D. Paulis, and R. Zoughi, "Rapid rotary scanner and portable coherent wideband Q-band transceiver for high-resolution millimeter-wave imaging applications," *IEEE Trans. Instrum. Meas.*, vol. 60, no. 1, pp. 186–197, Jan. 2011.
- [8] J. Song, Q. H. Liu, K. Kim, and W. R. Scott, "High-resolution 3-D radar imaging through nonuniform fast Fourier transform (NUFFT)," *Commun. Comput. Phys.*, vol. 1, no. 1, pp. 176–191, Feb. 2006.
- [9] B. Subiza, E. Gimeno-Nieves, J. M. Lopez-Sanchez, and J. Fortuny-Guasch, "An approach to SAR imaging by means of non-uniform FFTs," in *Proc. IEEE Int. Geosci. and Remote Sensing Symp.*, vol. 6, Spain, Jul. 2003, pp. 4089–4091.
- [10] J. T. Case, M. T. Ghasr, and R. Zoughi, "Optimum two-dimensional uniform spatial sampling for microwave SAR-based NDE imaging systems," *IEEE Trans. Instrum. Meas.*, vol. 60, no. 12, pp. 3806–3815, Dec. 2011.

- [11] I. G. Cumming and F. H. Wong, *Digital Processing of Synthetic Aperture Radar Data: Algorithms and Implementation*. Artech House, 2005.
- [12] J. M. Lopez-Sanchez and J. Fortuny-Guasch, “3-D radar imaging using range migration techniques,” *IEEE Trans. Antennas Propag.*, vol. 48, no. 5, pp. 728–737, May 2000.
- [13] D. M. Sheen, D. L. McMakin, and T. E. Hall, “Three-dimensional millimeter-wave imaging for concealed weapon detection,” *IEEE Trans. Microw. Theory Tech.*, vol. 49, no. 9, pp. 1581–1592, Sep. 2001.
- [14] D. L. Donoho, “Compressed sensing,” *IEEE Trans. Inf. Theory*, vol. 52, no. 4, pp. 1289–1306, Apr. 2006.
- [15] E. J. Candès, J. Romberg, and T. Tao, “Robust uncertainty principles: Exact signal reconstruction from highly incomplete frequency information,” *IEEE Trans. Inf. Theory*, vol. 52, no. 2, pp. 489–509, Feb. 2006.
- [16] E. J. Candès and J. Romberg, “Sparsity and incoherence in compressive sampling,” *Inverse Prob.*, vol. 23, no. 3, pp. 969–985, Apr. 2007.
- [17] E. J. Candès and M. B. Wakin, “An introduction to compressive sampling,” *IEEE Signal Process. Mag.*, vol. 25, no. 2, pp. 21–30, Mar. 2008.
- [18] L. C. Potter, E. Ertin, J. T. Parker, and M. Cetin, “Sparsity and compressed sensing in radar imaging,” *Proc. of the IEEE*, vol. 98, no. 6, pp. 1006–1020, Jun. 2010.
- [19] S. Chen and D. Donoho, “Basis pursuit,” in *Conf. Rec. of the 28th Asilomar Conf. on Signals, Systems and Comput.*, vol. 1, Pacific Grove, CA, Oct. 1994, pp. 41–44.
- [20] M. Soumekh, “Bistatic synthetic aperture radar inversion with application in dynamic object imaging,” *IEEE Trans. Signal Process.*, vol. 39, no. 9, pp. 2044–2055, Sep. 1991.
- [21] H. Kajbaf, J. T. Case, and Y. R. Zheng, “3D image reconstruction from sparse measurement of wideband millimeter wave SAR experiments,” in *Proc. of the 18th IEEE Int. Conf. on Image Process. (IEEE ICIP 2011)*, Brussels, Belgium, Sep. 2011, pp. 2701–2704.
- [22] H. Kajbaf, J. T. Case, Y. R. Zheng, S. Kharkovsky, and R. Zoughi, “Quantitative and qualitative comparison of SAR images from incomplete measurements using compressed sensing and nonuniform FFT,” in *Proc. 2011 IEEE Radar Conf. (RADAR)*, Kansas City, MO, May 2011, pp. 592–596.
- [23] J. Keiner, S. Kunis, and D. Potts, “Using NFFT 3—a software library for various nonequispaced fast Fourier transforms,” *ACM Trans. Math. Softw.*, vol. 36, no. 4, pp. 19:1–19:30, Aug. 2009.

- [24] Q. H. Liu and N. Nguyen, "An accurate algorithm for nonuniform fast Fourier transforms (NUFFT's)," *IEEE Microw. Guided Wave Lett.*, vol. 8, no. 1, pp. 18–20, Jan. 1998.
- [25] D. L. Donoho, Y. Tsaig, I. Drori, and J. C. Starck, "Sparse solution of underdetermined linear equations by stagewise orthogonal matching pursuit," *IEEE Trans. Inf. Theory*, pp. 1–39, Mar. 2006.
- [26] R. G. Baraniuk, "Compressive sensing [lecture notes]," *IEEE Signal Process. Mag.*, vol. 24, no. 4, pp. 118–121, Jul. 2007.
- [27] K. R. Varshney, M. Cetin, J. W. Fisher, and A. S. Willsky, "Sparse representation in structured dictionaries with application to synthetic aperture radar," *IEEE Trans. Signal Process.*, vol. 56, no. 8, pp. 3548–3561, Aug. 2008.
- [28] J. Yang and Y. Zhang, "Alternating algorithms for ℓ_1 -problems in compressive sensing," Rice University CAAM, Tech. Rep. TR09-37, Jun. 2010. [Online]. Available: <http://www.caam.rice.edu/zhang/reports/tr0937.pdf>
- [29] E. Peli, "Contrast in complex images," *J. Opt. Soc. Am. A*, vol. 7, no. 10, pp. 2032–2040, Oct. 1990.
- [30] N. Qaddoumi, A. Shroyer, and R. Zoughi, "Microwave detection of rust under paint and composite laminates," *Research in Nondestructive Evaluation*, vol. 9, no. 4, pp. 201–212, 1997.
- [31] C. D. Austin, E. Ertin, and R. L. Moses, "Sparse signal methods for 3-D radar imaging," *IEEE J. Sel. Topics Signal Process.*, vol. 5, no. 3, pp. 408–423, Jun. 2011.
- [32] Z. Yang and Y. R. Zheng, "Near-field 3-D synthetic aperture radar imaging via compressed sensing," in *Proc. IEEE Int. Conf. Acoustics, Speech, Signal Processing (ICASSP)*, Kyoto, Japan, Mar. 2012.
- [33] J. C. Yoo and Y. S. Kim, "A reverse-SAR (R-SAR) algorithm for the detection of targets buried in ground clutter," *Microwave and Optical Technology Lett.*, vol. 28, no. 2, pp. 121–126, Jan. 2001.
- [34] M. Figueiredo, J. Bioucas-Dias, and R. Nowak, "Majorizationminimization algorithms for wavelet-based image restoration," *IEEE Trans. Image Process.*, vol. 16, no. 12, pp. 2980–2991, Dec. 2007.
- [35] J. Yang, Y. Zhang, and W. Yin, "A fast alternating direction method for TVL1-L2 signal reconstruction from partial Fourier data," *IEEE J. Sel. Top. Signal Process.*, vol. 4, no. 2, pp. 288–297, Apr. 2010.
- [36] M. Lustig, D. L. Donoho, and J. M. Pauly, "Sparse MRI: The application of compressed sensing for rapid MR imaging," *Magn. Reson. Med.*, vol. 58, no. 6, pp. 1182–1195, 2007.

- [37] L. Rudin, S. Osher, and E. Fatemi, “Nonlinear total variation based noise removal algorithms,” *Phys. D*, vol. 60, no. 1-4, pp. 259–268, Nov. 1992.
- [38] A. Dutt and V. Rokhlin, “Fast Fourier transforms for nonequispaced data,” *SIAM J. Sci. Comput.*, vol. 14, no. 6, pp. 1368–1393, Nov. 1993.
- [39] A. V. Oppenheim and R. W. Schaffer, *Discrete-Time Signal Processing*. New Jersey, USA: Prentice Hall, 2010.
- [40] K. Grochenig and T. Strohmer, “Numerical and theoretical aspects of nonuniform sampling of band-limited images,” in *Nonuniform Sampling: Theory and Practice*, F. Marvasti, Ed. New York: Kluwer Academic/Plenum Publishers, 2001, pp. 283–324.
- [41] S. Kharkovsky, J. T. Case, M. T. Ghasr, R. Zoughi, S. W. Bae, and A. Belarbi, “Application of microwave 3D SAR imaging technique for evaluation of corrosion in steel rebars embedded in cement-based structure,” in *Review of Progress in Quantitative Nondestructive Evaluation, Burlington, VT, Chicago, IL, Jul. 17-22, 2011, AIP Conference Proceedings*, D. O. Thompson and D. E. Chimenti, Eds. Melville, NY: American Institute of Physics, 2012, to be published.
- [42] J. M. Duarte-Carvajalino and G. Sapiro, “Learning to sense sparse signals: Simultaneous sensing matrix and sparsifying dictionary optimization,” *IEEE Trans. Image Process.*, vol. 18, no. 7, pp. 1395–1408, Jul. 2009.
- [43] G. Peyré, “Best basis compressed sensing,” *IEEE Trans. Signal Process.*, vol. 58, no. 5, pp. 2613–2622, May 2010.
- [44] H. W. Chen, L. W. Kang, and C. S. Lu, “Dictionary learning-based distributed compressive video sensing,” in *Picture Coding Symp. (PCS)*, Dec. 2010, pp. 210–213.
- [45] A. Soni and J. Haupt, “Efficient adaptive compressive sensing using sparse hierarchical learned dictionaries,” *ArXiv e-prints*, pp. 1–5, Nov. 2011.
- [46] S. Ravishankar and Y. Bresler, “MR image reconstruction from highly under-sampled k-space data by dictionary learning,” *IEEE Trans. Med. Imag.*, vol. 30, no. 5, pp. 1028–1041, May 2011.
- [47] J. J. Thiagarajan, K. N. Ramamurthy, and A. Spanias, “Multilevel dictionary learning for sparse representation of images,” in *Digital Signal Processing Workshop and IEEE Signal Processing Education Workshop (DSP/SPE)*, Jan. 2011, pp. 271–276.
- [48] S. Rickard, “Sparse sources are separated sources,” in *Proc. 16th Annu. European Signal Process. Conf.*, Florence, Italy, 2006.

- [49] C. M. Akujuobi, O. O. Odejide, A. Annamalai, and G. L. Fudge, “Sparseness measures of signals for compressive sampling,” in *IEEE Int. Symp. on Signal Process. and Inform. Technology*, Dec. 2007, pp. 1042–1047.
- [50] N. Hurley and S. Rickard, “Comparing measures of sparsity,” *IEEE Trans. Inf. Theory*, vol. 55, no. 10, pp. 4723–4741, Oct. 2009.
- [51] D. Zonoobi, A. A. Kassim, and Y. V. Venkatesh, “Gini index as sparsity measure for signal reconstruction from compressive samples,” *IEEE J. Sel. Topics Signal Process.*, vol. 5, no. 5, pp. 927–932, Sep. 2011.
- [52] T. A. Schonhoff and A. A. Giordano, *Detection and Estimation Theory and Its Applications*. Prentice Hall, 2006.
- [53] A. Tarczynski and N. Allay, “Spectral analysis of randomly sampled signals: Suppression of aliasing and sampler jitter,” *IEEE Trans. Signal Process.*, vol. 52, no. 12, pp. 3324–3334, Dec. 2004.
- [54] R. Baraniuk and P. Steeghs, “Compressive radar imaging,” in *Proc. 2007 IEEE Radar Conf.*, Boston, MA, Apr. 2007, pp. 128–133.
- [55] A. Budillon, A. Evangelista, and G. Schirinzi, “Three-dimensional SAR focusing from multipass signals using compressive sampling,” *IEEE Trans. Geosci. Remote Sens.*, vol. 49, no. 1, pp. 488–499, Jan. 2011.

VITA

Hamed Kajbaf received a BS degree in Electrical Engineering from Shiraz University, Shiraz, Iran, in 2006. He received an MS degree in Biomedical Engineering-Bioelectric from Tarbiat Modares University, Tehran, Iran, in 2009. He began his PhD study in August 2009 in the Electrical and Computer Engineering department at Missouri University of Science and Technology, Rolla, MO, USA.

His research interests include digital signal and image processing, sensing and imaging systems optimization, microwave and acoustic imaging, and array signal processing. His current area of research is on compressed sensing and its applications to microwave imaging systems.